



**THE UNIVERSITY OF
WESTERN AUSTRALIA**

Achieving International Excellence

School of Electrical, Electronic and Computer Engineering

**DEVELOPMENT OF IN-WHEEL MOTOR SYSTEMS
FOR FORMULA SAE ELECTRIC VEHICLES**

Ian Hooper

Student number: 20669056

Supervisor: Prof. Thomas Bräunl

School of Electrical, Electronic and Computer Engineering

This thesis submitted for the degree of

Master of Engineering Science

The University of Western Australia

Submitted: 4th November 2011



THE UNIVERSITY OF
WESTERN AUSTRALIA

DECLARATION FOR THESES CONTAINING PUBLISHED WORK AND/OR WORK PREPARED FOR PUBLICATION

The examination of the thesis is an examination of the work of the student. The work must have been substantially conducted by the student during enrolment in the degree.

Where the thesis includes work to which others have contributed, the thesis must include a statement that makes the student's contribution clear to the examiners. This may be in the form of a description of the precise contribution of the student to the work presented for examination and/or a statement of the percentage of the work that was done by the student.

In addition, in the case of co-authored publications included in the thesis, each author must give their signed permission for the work to be included. If signatures from all the authors cannot be obtained, the statement detailing the student's contribution to the work must be signed by the coordinating supervisor.

Please sign one of the statements below.

<p>1. This thesis does not contain work that I have published, nor work under review for publication.</p> <p>Student Signature <i>[Handwritten Signature]</i></p>
<p>2. This thesis contains only sole-authored work, some of which has been published and/or prepared for publication under sole authorship. The bibliographical details of the work and where it appears in the thesis are outlined below.</p> <p>Student Signature</p>
<p>3. This thesis contains published work and/or work prepared for publication, some of which has been co-authored. The bibliographical details of the work and where it appears in the thesis are outlined below. The student must attach to this declaration a statement for each publication that clarifies the contribution of the student to the work. This may be in the form of a description of the precise contributions of the student to the published work and/or a statement of percent contribution by the student. This statement must be signed by all authors. If signatures from all the authors cannot be obtained, the statement detailing the student's contribution to the published work must be signed by the coordinating supervisor.</p> <p>Student Signature</p> <p>Coordinating Supervisor Signature</p>

ABSTRACT

With the threat of anthropogenic climate change and humanity's dependence on non-renewable petroleum, the need for a transition to zero-emission transport is widely acknowledged. Battery electric vehicles represent the most promising solution for urban transport, being the most efficient technology which can be powered from renewable energy sources.

As of 2011, most major automobile manufacturers have either released or announced development of electric vehicles, and it is clear that they are going to play a big role in our future transport needs. To date, all such vehicles employ a conventional drivetrain with a single motor, driving the wheels through a transmission and differential.

In contrast, many small electric vehicles such as bicycles and scooters have employed in-wheel motor systems (also known as hub motors) – where the electric motor is contained within the wheel hub itself. In-wheel motor systems offer many advantages over conventional drivetrains including fewer moving parts, lower transmission losses, and space savings. However the performance requirements of road-going automobiles has so far precluded the use of in-wheel motor systems.

This thesis reviews electric motor technology and recent academic research on in-wheel motor systems to determine the most promising candidates. A design for a direct-drive wheel motor is proposed and optimised through magnetostatic Finite Element Analysis (FEA) experiments. Finally the development of an in-wheel motor system for a Formula SAE Electric vehicle is presented, based on a high-speed motor with reduction drive, and its performance is compared with the direct-drive solution.

Formula SAE is an international competition which challenges university students to construct and race Formula-style vehicles. The competition was started in 1978 for petroleum-powered vehicles. In response to growing interest in sustainable transport and electric vehicles, in 2007 many universities began developing electric FSAE vehicles. The competition represents a valuable arena for electric vehicle research and evaluation.

TABLE OF CONTENTS

	<i>page</i>
1 Introduction	1
1.1 The Future is Electric	1
1.2 Research Goals	2
1.3 Thesis Overview	3
2 Electric Vehicle Review	4
2.1 Introduction	4
2.2 Road-Going Electric Vehicles	4
2.2.1 Tesla Roadster	4
2.2.2 Mitsubishi i-MiEV	5
2.2.3 Nissan LEAF	6
2.3 Formula SAE Electric Vehicles	7
2.3.1 University of Stuttgart's Green Team	7
2.3.2 RMIT's R10E Formula SAE Electric vehicle	8
2.4 FSE at The University of Western Australia	8
2.4.1 2009/10 Prototype Vehicle	8
2.4.2 2011/12 FSE Competition Vehicle	11
3 Requirements Analysis	13
3.1 Introduction	13
3.2 Power and Torque Requirements	13
3.3 Qualitative Requirements	15
3.3.1 Requirements Summary For Formula SAE Electric Vehicle	16
4 Motor Theory Review	17
4.1 Electromagnetic Fundamentals	17
4.1.1 Fundamental Equations	17
4.1.2 Magnetic Permeability	19
4.1.3 Remanence, Coercivity and Hysteresis Losses	21
4.1.4 Eddy Currents	22
4.1.5 Saliency and Cogging Torque	23
4.1.6 Efficiency	24
4.1.7 Pole Count	25
4.2 Taxonomy of Electric Motors	25
4.2.1 Permanent Magnet Direct Current (PMDC) Motors	26

4.2.2	Dual-wound DC Motors	27
4.2.3	AC Induction Motors	28
4.2.4	Variable Reluctance Motors	29
4.2.5	Permanent Magnet Synchronous Motors (PMSMs)	30
4.3	Halbach Arrays	32
4.4	Vernier Drive Motors	32
4.5	Motor Control Review	35
4.5.1	Introduction	35
4.5.2	Pulse Width Modulation	35
4.5.3	DC Motor Control	36
4.5.4	Three-phase Motor Control	36
4.5.5	Field Oriented Control	38
4.5.6	Sensored vs Sensorless Control	39
5	In-Wheel Motor Systems Review	40
5.1	Introduction	40
5.2	Axial Flux Motors	41
5.2.1	Outer-rotor Radial Flux Motors	50
5.3	More exotic motor topologies	54
5.3.1	Transverse Flux Permanent Magnet (TFPM) machines	54
5.3.2	Variable Reluctance Motors (VRM)	55
5.3.3	Spherical Wheel Motors	56
5.3.4	Reducing Permanent Magnet Volume	57
5.3.5	Polyphase Motors and Controllers	58
5.4	Previous Hub Motor Designs for FSAE Vehicles	59
5.5	Commercial Products and Prototypes	61
5.5.1	Introduction	61
5.5.2	Protean Electric (formerly PML Flightlink)	61
5.5.3	Michelin Active Wheel	62
5.5.4	Siemens VDO eCorner	63
5.5.5	E-traction	64
5.6	High Performance Motors	65
5.7	Unsprung Weight Considerations	68
5.8	Discussion	72
6	Magnetostatic FEA Experiments	75
6.1	Introduction	75

6.2	Backplate material	75
6.2.1	Introduction	75
6.2.2	Simulation Results	75
6.2.3	Summary	76
6.3	Effect of airgap width	77
6.3.1	Introduction	77
6.3.2	Simulation Results	77
6.3.3	Summary	78
6.4	Backplate Thickness	79
6.4.1	Introduction	79
6.4.2	Simulation results	79
6.4.3	Summary	80
6.5	Effect of Magnet Thickness	81
6.5.1	Introduction	81
6.5.2	Simulation Results	81
6.5.3	Summary	82
6.6	Inter-pole Leakage vs Pole Pitch	83
6.6.1	Introduction	83
6.6.2	Simulation Results	83
6.6.3	Summary	84
6.7	Effectiveness of Halbach Array	85
6.7.1	Introduction	85
6.7.2	Simulation Results	85
6.7.3	Summary	86
6.8	Summary of Results	87
7	Direct Drive Design & Analysis	88
7.1	Introduction	88
7.2	Design Decisions	88
7.3	Proposed Design	89
7.4	Theoretical Performance Analysis	92
7.4.1	Copper Fill Factor	92
7.4.2	FEA Simulation	92
7.4.3	Estimating Torque/Speed Characteristics	93
7.4.4	Estimating Torque Ratings	94
7.5	Conclusion of Findings	95

8	Commercial Motor Testing	96
8.1	Introduction	96
8.2	Design Analysis	97
8.2.1	Introduction	97
8.2.2	Physical Measurements	98
8.2.3	Design Analysis and Discussion	98
8.3	Magnetic Leakage Testing	100
8.3.1	Introduction	100
8.3.2	Method and Materials	100
8.3.3	Results	101
8.3.4	Discussion	102
8.4	Back-EMF Testing	103
8.4.1	Introduction and Method	103
8.4.2	Results	103
8.4.3	Discussion	105
8.5	Adding Hall sensors	105
8.6	No-Load Test	106
8.6.1	Introduction	106
8.6.2	Materials and Method	107
8.6.3	Results: Hall sensors	107
8.6.4	Results: Phase Windings	108
8.6.5	Discussion	109
8.7	Fixed Load Test	110
8.7.1	Introduction	110
8.7.2	Materials and Method	110
8.7.3	Results	111
8.7.4	Discussion	112
8.8	Effects of Hall sensor Timing	113
8.8.1	Introduction	113
8.8.2	Materials and Method	113
8.8.3	Results	113
8.8.4	Discussion	114
8.9	Conclusion	115
9	Mechanical Design Of Wheel Hub	116
9.1	Introduction	116
9.2	Suspension Attachments	116

9.3	Drivetrain Comparison	118
9.3.1	Introduction	118
9.3.2	Belt Drive	118
9.3.3	Planetary Gearbox	120
9.3.4	Pinion and Spur Gears	122
9.4	Preliminary CAD Model	126
9.5	Design Verification and Optimisation	126
9.5.1	Introduction	126
9.5.2	Verification of Wheel Bearing Load Rating	127
9.5.3	Brake Caliper Mount Strength Verification	127
9.5.4	Upright Body Lightening and Verification	129
9.5.5	Optimisation of Spur Gear	131
9.5.6	Final Design	132
9.6	Summary	133
10	Conclusion	134
11	References	136

LIST OF FIGURES

Figure 2.1: Tesla Roadster (Source: Wikipedia 2011)	4
Figure 2.2: Mitsubishi i-MiEV	5
Figure 2.3: The Nissan LEAF	6
Figure 2.4: Uni Stuttgart Green Team's 2010 FSE vehicle	7
Figure 2.5: RMIT's R10E FSE Vehicle	8
Figure 2.6: CAD render of prototype Formula SAE Electric vehicle	9
Figure 2.7: Top view of prototype FSE vehicle showing component locations	9
Figure 2.8: Prototype vehicle in testing at the race track, early 2010	10
Figure 2.9: CAD render of the 2011/12 Formula SAE Electric vehicle	11
Figure 2.10: Top view of 2011/12 FSE vehicle showing component layout	12
Figure 3.1: Speed-power graph for road-going car	14
Figure 3.2: Speed-power graph for Formula SAE	14
Figure 4.1: Electric current produces a magnetic field	18
Figure 4.2: Conductors in a magnetic field distort flux and induce forces	19
Figure 4.3: B-H curves for vacuum, diamagnetic or paramagnetic materials (Reproduced from Clarke 2008)	20
Figure 4.4: B-H curves of three common ferromagnetic materials (reproduced from Wildi 2002)	20
Figure 4.5: Hysteresis loop for magnetisation cycles in ferromagnetic material (Reproduced from Clarke 2008b)	21
Figure 4.6: Use of laminated steel reduces electrical conduction paths and hence eddy currents	22
Figure 4.7: Litz wire, (a) regular copper bundle (b) Litz wire (c) finer wires for high frequencies	23
Figure 4.8: Illustration showing typical example of 2, 4 and 6 pole permanent magnet motors	25
Figure 4.9: Taxonomy of five common types of electric motor	26
Figure 4.10: Typical brushed/commutated DC permanent magnet motor (2-pole, inner-rotor, radial flux)	26
Figure 4.11: Typical wound-stator DC motor (2-pole, inner-rotor, radial flux)	27
Figure 4.12: Typical AC induction motor with "Squirrel Cage" rotor	28
Figure 4.13: Example of a Variable Reluctance motor design	29
Figure 4.14: Example topology of a PMSM (2-pole, inner-rotor, axial flux)	30
Figure 4.15: Three common topologies for PMSM motors: Inner rotor, outer rotor and axial flux	31
Figure 4.16: Asymmetric magnetic field around 3-magnet Halbach array (Copied from Volk 2008)	32
Figure 4.17: Common example of a 10-pole 12-slot outer-rotor LRK, a PMSM vernier drive motor	33
Figure 4.18: Effect of Pulse Width Modulated voltage on motor current flow	35
Figure 4.19: Half-bridge and full-bridge control of (mechanically-commutated) DC motors	36
Figure 4.20: Graph of trapezoidal control waveforms	37
Figure 4.21: 3-phase windings	37
Figure 4.22: Graph of sinusoidal 3-phase voltage waveforms	37
Figure 4.23: 3-phase windings	37
Figure 4.24: Typical circuit for three-phase bridge and motor	37
Figure 4.25: Generic 3-phase drive system (Reproduced from Murray, Kettle & Moynihan 1997)	38
Figure 5.1: Cross section of two-stage axial-flux permanent magnet machine with ironless water-cooled stator winding (Copied from Caricchi et al 1996)	42
Figure 5.2: Cross-sectional drawing of CSIRO wheel motor (Copied from Lovatt, Ramsden & Mecrow 1997)	43

Figure 5.3: Halbach magnet array and air-gap winding(Copied from Lovatt, Ramsden & Mecrow 1997)	43
Figure 5.4: Cross-section of motor topology(Copied from Pullen & Mansir 1999)	44
Figure 5.5: Cutaway view of motor(Copied from Pullen & Mansir 1999)	44
Figure 5.6: Cross section of the UltraCommuter Rear Wheel Mounted Direct Drive Motor(Copied from Greaves et al 2003)	45
Figure 5.7: Cross-section of motor design(Copied from Xiaoyuan et al 2005)	45
Figure 5.8: 3D view of three-disc magnet layout(Copied from Xiaoyuan et al 2005)	45
Figure 5.9: Exploded diagram of axial-flux wheel motor (Copied from Yang, Luh & Cheung 2004)	46
Figure 5.10: Dual axial-flux motor topology and its 2D configuration (Copied from Yang, Luh & Cheung 2004)	46
Figure 5.11: 3D render of AFPM wheel motor design (Copied from Rahman et al 2006)	47
Figure 5.12: Picture of test unit installed on mule vehicle (Copied from Rahman et al 2006)	47
Figure 5.13: (a) Flux in the rotor back iron showing the area of low flux concentration. (b) Area of low flux concentration removed from the back iron to reduce mass. (Copied from Rahman et al 2006)	47
Figure 5.14: Winding cooling arrangement. (a) Stator and cooling ring separate. (b) Stator and cooling ring engaged. (Copied from Rahman et al 2006)	47
Figure 5.15: Comparison of axial flux motor topologies:Surface-PM (left) or interior PM(Copied from Profumo, Zhang & Tecomi 1997)	48
Figure 5.16: Comparison of axial flux motor topologies: inner-rotor (left), torus inner-stator (middle),and segmented armature torus (right) (Copied from Woolmer & McCulloch 2007)	49
Figure 5.17: Image of YASA-750 motor(From YASA Motors 2011)	50
Figure 5.18: Dimensions of YASA-750 motor(From YASA Motors 2011)	50
Figure 5.19: Typical example of direct drive bicycle hub motor (Copied from Brand, Ertugrul & Soong 2003)	51
Figure 5.20: Cross section of in-wheel motor (Copied from Terashima et al 1997)	52
Figure 5.21: Configuration of the in-wheel motor system (Copied from Chung 2008)	52
Figure 5.22: Assembled stator and rotor of the in-wheel motor (C Copied from hung 2008)	52
Figure 5.23: 3D Cross-section of PM ironless machine (Modified copy from Greaves, Walker & Walsh 2001)	53
Figure 5.24: Transverse flux PM topology, where w_m is the direction of movement(Copied from Svehkarenko et al 2008)	54
Figure 5.25: Geometry of the TVHR motor (Copied from Espanet, Kauffmann & Bernard 2006)	55
Figure 5.26: Cross section of the four-phase 8/6 VRM (Copied from Wang et al 2005)	56
Figure 5.27: Rotor and stator of the prototype VRM(Copied from Wang et al 2005)	56
Figure 5.28: Photo of PM spherical wheel motor (Copied from Kang et al 2009)	57
Figure 5.29: Structure and operation of PM spherical wheel motor (Copied from Kang et al 2009)	57
Figure 5.30: IPM Wheel Motor magnetic components geometry (Copied from Laskaris & Kladas 2008)(a) Stator - 0.5mm laminated silicon steel(b) Rotor - Solid iron magnetic core blocks(c) Rotor - NdFeB permanent magnet blocks	58
Figure 5.31: Magnetic flux density distribution in the motor under full load(Copied from Laskaris & Kladas 2008)	58
Figure 5.32: Radial cross-section of proposed wheel motor(Copied from Tseng & Chen 2005)	59
Figure 5.33: Axial cross-section of proposed wheel motor(Copied from Tseng & Chen 2005)	59
Figure 5.34: Two views of the in-wheel two-stage pulley system (Copied from Ivanescu 2009)	60
Figure 5.35: Exploded view of in-wheel drive system (Copied from Harris 2010)	60
Figure 5.36: Cutaway view of Protean Electric's electric wheel motor (Copied from Brooke 2010)	61

Figure 5.37: Performance graph of Protean Electric PD18 In-Wheel Motor System (Protean Electric 2011)	62
Figure 5.38: Components of Michelin Active Wheel (Copied from Michelin 2008)	62
Figure 5.39: Cutaway view of Siemens eCorner wheel motor solution (Copied from Autospectator 2006)	63
Figure 5.40: 3D render of TheWheel system (Copied from e-Traction 2011)	64
Figure 5.41: Exploded view of TheWheel system(Copied from e-Tracton 2011)	64
Figure 5.42: Motenergy ME0201 PMSM motor	65
Figure 5.43: Quarter vehicle suspension model (as per Schalkwyk & Kamper 2006)	68
Figure 5.44: Bode plot of suspension frequency response (Copied from Schalkwyk & Camper 2006)	69
Figure 5.45: Sprung and unsprung mass step response (Copied from Schalkwyk & Kamper 2006)	69
Figure 5.46: Dynamic model for separately-suspended wheel motor (Copied from Li-qiang, Chuan-xue & Qing-nian 2010)	70
Figure 5.47: Frequency response for separately-suspended wheel motor vs conventional wheel motor and inboard drivetrain (Copied from Li-qiang, Chuan-xue & Qing-nian 2010)	70
Figure 5.48: Illustration of rotor perturbation by the road surface (Copied from Hredzak, Gair & Eastham 1996)	70
Figure 5.49: Three basic layouts for in-wheel motor drive: (a) Axial flux motor, direct drive(b) Outer-rotor (ring) motor, direct drive (c) High speed motor with reduction drive	73
Figure 6.1: Comparison of magnetic fields for steel vs aluminium rotor backplates	76
Figure 6.2: Magnetic simulation showing effect of varying air gap	77
Figure 6.3: Graph of field strength for varying air gap	78
Figure 6.4: Magnetic simulation showing effect of steel backplate thickness	79
Figure 6.5: Graph of air gap flux vs leakage flux for various backplate thicknesses	80
Figure 6.6: Magnetic simulation showing effect of varying magnet thickness	81
Figure 6.7: Graph of air gap and leakage flux for various magnet thicknesses	82
Figure 6.8: Magnetic simulation showing flux for various pole pitch to airgap ratios	83
Figure 6.9: Graph of inter-pole leakage vs pole pitch:airgap ratio	84
Figure 6.10: Magnetic simulation comparing Halbach Arrays with typical magnet arrangements	85
Figure 6.11: Graphical comparison of air gap and leakage flux for Halbach vs typical configurations	86
Figure 7.1: Orthographic projection of proposed axial flux PMSM motor	89
Figure 7.2: Winding diagram (conductors shown at reduced diameter for clarity)	90
Figure 7.3: Actual active conductor fill factor	90
Figure 7.4: Proposed hub layout with direct drive motor (top view)	91
Figure 7.5: Maxwell simulation of proposed motor	92
Figure 7.6: Plot of airgap field strength	93
Figure 7.7: Graph of resistive power loss vs motor current	95
Figure 8.1: From left to right: Plettenberg Predator 37, Turnigy CA120-70, Turnigy CA80100-130	96
Figure 8.2: Diagram of setup for magnetic leakage test	101
Figure 8.3: Hall sensor and position markings on motor can	101
Figure 8.4: Individual graphs of motor magnetic field leakage	101
Figure 8.5: Combined and phase-corrected graph of motor leakage	102
Figure 8.6: Back-EMF waveform for Turnigy CA120-70	103
Figure 8.7: Back-EMF waveform for Plettenberg Predator 37	104
Figure 8.8: External Hall sensors added to Turnigy motor	106
Figure 8.9: Test setup for no-load motor experiments	107
Figure 8.10: Oscilloscope capture of Hall sensors A (blue) and B (red)	107
Figure 8.11: Oscilloscope capture of Hall sensors A (blue) and C (red)	108

Figure 8.12: Plettenberg phase capture, 1ms/div	108
Figure 8.13: Turnigy phase capture, 500ms/div	108
Figure 8.14: Plettenberg phase capture, 250us/div	108
Figure 8.15: Turnigy phase capture, 100us/div	108
Figure 8.16: Plettenberg phase capture, 10us/div	109
Figure 8.17: Turnigy phase capture, 10us/div	109
Figure 8.18: Overview of full power motor test rig	111
Figure 8.19: Power consumption vs speed for motors tested	112
Figure 8.20: Effect of timing on current at various speeds	114
Figure 9.1: CAD rendering of front left suspension design, as designed by Marcin Kiszko (2011)	117
Figure 9.2: Suspension reference (Kiszko 2011)	117
Figure 9.3: Space constraints make single-stage belt drive impractical due to inadequate wrap angle	119
Figure 9.4: Diagram of a typical planetary gearbox	120
Figure 9.5: Possible suspension pull rod interference with planetary hub design (Kiszko 2011)	121
Figure 9.6: Top view (left) and front view (right) for hub layout based on planetary gearbox	121
Figure 9.7: Picture of pinion/spur (TEA2080NH, TEA2012) and planetary gear set (Matex120-5MNH)	122
Figure 9.8: Four possible layouts (top-view) based on pinion/spur reduction gears	124
Figure 9.9: Preliminary hub design in SolidWorks	126
Figure 9.10: Close-up of design without wheel	126
Figure 9.11: Diagram of forces on wheel bearings	127
Figure 9.12: Drawing of caliper mounting bracket	128
Figure 9.13: Von Mises analysis of brake caliper mounting bracket	128
Figure 9.14: Lightening of the upright body	129
Figure 9.15: Forces experienced by upright body	130
Figure 9.16: Von Mises stresses on upright	130
Figure 9.17: Highlighted areas where safety factor < 1 (material failure)	130
Figure 9.18: SolidWorks model of unmodified gear	131
Figure 9.19: Von Mises analysis of unmodified gear	131
Figure 9.20: Design of lightened gear	132
Figure 9.21: Von Mises analysis of lightened gear	132
Figure 9.22: Exploded view of wheel hub assembly	132
Figure 11.1: FSAE vehicle Centre of Gravity location (front view)	144
Figure 11.2: FSAE vehicle Centre of Gravity location (side view)	145
Figure 11.3: Keizer 4L Wheel Specifications Sheet (Keizer Wheels 2011)	149
Figure 11.4: 3D Model (Keizer Wheels 2011)	149
Figure 11.5: Photo of actual wheels (Keizer Wheels 2011)	149

LIST OF SYMBOLS

Symbol	Description	Units	
Φ	Magnetic Flux	Wb	Webers
B	Magnetic Flux Density	T	Tesla
A	Area	m ²	Square metres
ε	Induced electromotive force (EMF)	V	Volts
t	Time	s	Seconds
μ	Magnetic permeability	Hm ⁻¹	Henrys per metre
μ_0	Magnetic permeability of vacuum	Hm ⁻¹	Henrys per metre
μ_r	Relative permeability		
MMF	Magnetomotive Force	A	Amp-turns
H	Magnetic field strength	Am ⁻¹	Amp-turns per metre
H _c	Coercivity	Am ⁻¹	Amperes per metre
R	Reluctance	A/Wb or H ⁻¹	
q	Electric charge	C	Coulombs
F	Force	N	Newtons
E	Electric field	Vm ⁻¹	Volts per metre
v	Velocity	ms ⁻¹	Metres per second
I	Current	A	Amperes
L	Length	m	Metres
ρ	Resistivity (Electrical)	Ω m	Ohm-metre
Kv	Motor speed constant	RPM/V or rad/s/V (SI units)	
Kt	Motor torque constant	Nm / A	Newton-metre / amp

ACKNOWLEDGEMENTS

My thanks go to Professor Thomas Bräunl for acting as supervisor for this research. Thomas is also the coordinator of the REV Project at UWA, a research group dedicated to the development of electric vehicles, which was the catalyst for my postgraduate studies.

I also owe thanks to many of my fellow students under the REV Project, particularly Marius Ivanescu and Daniel Harris who were both also involved with in-wheel motor research for the Formula SAE vehicles.

And finally my parents, whose financial and moral support over the past two and a half years has been greatly appreciated.

1 INTRODUCTION

1.1 THE FUTURE IS ELECTRIC

The problems associated with vehicle emissions have long been a cause for concern, partly due to airborne pollutants, and more recently relating to climate change due to greenhouse gas emissions. According to the US Environmental Protection Agency (EPA), in addition to up to 40% of greenhouse gas emissions, conventional Internal Combustion Engine (ICE) vehicles contribute 40-50% of ozone, 80-90% of carbon monoxide and 50-60% of air toxins found in urban areas (Ehsani, Rahman & Toliyat 1997). And with vehicle numbers forecast to increase from 700 million to 2.5 billion in the next half century (Chan & Wong 2004), the need for sustainable transport solutions is clear.

So recent years have seen a surge of interest in zero emission transport solutions. The leading contender to replace petrol-powered vehicles at present is Battery-powered Electric Vehicles (BEVs), since they are the most efficient solution which can be powered (recharged) entirely from renewable energy sources.

Until recently, the low energy density of batteries restricted the driving range of BEVs to such an extent that they were not a viable option for many applications. However the development of batteries based on Lithium chemistries have been an enabling factor for electric vehicles, offering sufficiently high energy density to provide vehicles with usable range for urban use, exceeding the day-to-day requirements of the vast majority of road users – even if still well short of petrol-powered vehicles.

Of the many mass produced electric vehicles so far released or currently in development, all have featured a conventional drivetrain consisting of a motor, gearbox, differential, and Constant Velocity (CV) joints to the wheels. This style of drivetrain evolved to suit the limitations of an Internal Combustion Engine (ICE), where the most economical solution features a single centralised engine.

However, electric drives can be used with very different drivetrain topologies. One alternative to conventional drivetrains is to incorporate the motor into the wheel, known as an in-wheel drive system, or hub motor. In-wheel drive systems are not a new idea, with patents dating back to the late 19th century (Adams 1884, Theryc 1896, Parcelle 1890). They were even used in a production car from Porsche between 1900-1905.

In-wheel motors hold the promise of several attractive advantages, such as elimination of drivetrain

losses for higher efficiency, space savings in the vehicle body allowing for better utilisation of space, and the possibility of new advanced traction control systems (Ando & Fujimoto 2010, Laine & Fredriksson 2007, Kim & Kim 2007).

1.2 RESEARCH GOALS

The main hypothesis being explored in this thesis is whether in-wheel motor systems are a viable option for passenger vehicles.

The largest potential application of in-wheel motor systems is road-going passenger automobiles, of which there are currently over 700 million worldwide, so no study would be complete without considering this application. However for this project, the available test vehicle and first application of the research was a Formula SAE Electric vehicle.

Formula SAE is an international competition for university students to design and race Formula-style vehicles. Historically these were powered by small internal combustion engines. Around 2008, a new category was introduced for electric vehicles. It is envisaged that Formula SAE Electric will be a valuable forum for electric vehicle research. Hence, a second research goal here is to quantify the differences in requirements between Formula SAE vehicles and road-going automobiles.

Electric motors come in a wide range of electromagnetic designs and topologies, which had been developed over many decades. The fact that there exists more than one type of electric motor is proof that some types are more suitable for certain applications than others. By evaluating the performance characteristics of the various types of electric motors, with respect to the requirements of in-wheel motor drive, it should be possible to determine the most suitable motor technology.

Similarly in-wheel motors can be implemented in a variety of ways. By reviewing in-wheel motor research and evaluating existing designs, the most suitable topologies should become apparent.

With this knowledge, in-wheel motor designs based on the most promising technologies can be considered and evaluated to determine if the original hypothesis has been met: are they viable for use in passenger vehicles.

1.3 THESIS OVERVIEW

This thesis begins with some background information about road-going electric vehicles and Formula SAE electric (Chapter 2). Then the requirements of the two application are identified, such as speeds and accelerations expected for a Formula SAE vehicle, and how they translate back to motor requirements (Chapter 3)

After a review of fundamental electromagnetic theory, motor design and motor controller design (Chapter 4), academic literature and commercial prototypes for in-wheel drive systems are reviewed to determine the most suitable technologies available, and areas for further research (Chapter 5). As a result two possible options are identified, one being a direct drive solution (motor turns the wheel directly, 1:1 ratio) based on a high torque (low speed) motor, and the other a reduction drive solution using high-speed motor.

The direct drive option is evaluated first, starting with a range of Finite Element Analysis experiments to help optimise machine dimensions (Chapter 6). A design for a direct drive motor is presented, and its performance predicted through a combination of Finite Element Analysis (FEA) simulation and theoretical analysis (Chapter 7).

Next the reduction drive option is explored, starting with testing some commercial high-speed motor candidates (Chapter 8). Once a suitable motor is identified, a reduction drive system is designed and evaluated (Chapter 9).

Finally some conclusions are drawn as a result of the research, and some directions for further study identified (Chapter 10).

2 ELECTRIC VEHICLE REVIEW

2.1 INTRODUCTION

Growing concern over pollution and climate change has created a surge of interest in electric vehicles in recent years. Two distinct applications for in-wheel motors are discussed in this thesis. The first is one of the biggest potential applications for in-wheel motor systems: road-going vehicles, of which there are hundreds of millions around the world. As of 2011, most major automobile manufacturers have either released or are developing battery-powered electric cars.

However as with many other automotive technologies, the research and development which occurs in the racing world often becomes applicable to road-going vehicles, which is why the Formula SAE Electric competition makes a viable application for this research.

In this chapter we review some of the first road-going electric vehicles released in recent years, as well as some of the first Formula SAE Electric vehicles developed at other universities. Other than the latest Formula SAE vehicle being developed at the University of Western Australia (UWA), all of the vehicles reviewed employ a conventional drivetrain with inboard motor(s) and CV joints to the wheels.

2.2 ROAD-GOING ELECTRIC VEHICLES

2.2.1 Tesla Roadster

The first highway-capable all-electric mass-produced vehicle available in the United States was the Tesla Roadster, introduced for sale in 2008 (Wikipedia: Tesla Roadster 2011).



Figure 2.1: Tesla Roadster (Source: Wikipedia 2011)

Tesla had an unusual strategy in introducing a vehicle at the top end of the market, being priced around US\$100,000. However the high price allowed for the use of high performance components.

The vehicle is mid-engined, rear wheel drive. It was originally based on a Lotus Elise but the final production version only shares 6% of its parts in common. It uses an Alternating Current Induction Motor (ACIM) with peak power of 185kW, with up to 270Nm torque and 14000rpm top speed. Drive to the wheels is via a single reduction ratio and differential.

It has a relatively large 53kWh lithium ion battery pack which represents approximately one third of the total vehicle weight. To leverage mass production, it is constructed from almost 7000 individual lithium cells similar to those used in laptop computers. Replacement cost for the pack is cited as US\$36000, with a service life of 7 years or 100,000km.

The large size of the pack enables the vehicle to achieve an EPA certified range of 392 km, which is comparable to similar petrol powered vehicles. As well as its impressive range, the Roadster achieves acceleration of 0-100km/h in about 4 seconds, which is also very competitive against petrol powered vehicles in its price bracket.

Approximately 2000 Tesla Roadsters have been sold since its introduction.

2.2.2 Mitsubishi i-MiEV

In 2009 Mitsubishi released its first all-electric vehicle, the i-MiEV. In contrast with the Tesla Roadster, it was a more conventional small car and targeting the commuter market.



Figure 2.2: Mitsubishi i-MiEV

It is powered by a 47kW permanent magnet motor with 180Nm maximum torque, through a single reduction ratio and differential to the wheels (Wikipedia: i-MiEV). Its battery is 16kWh lithium ion – less than one third the capacity of the Tesla Roadster’s batter – and achieves an EPA-certified range of approximately 100km.

In most areas it has been priced around US\$45000 or equivalent. This price is substantially higher than equivalent petrol vehicles, which has no doubt hindered widespread adoption.

2.2.3 Nissan LEAF

Released in 2010, the Nissan LEAF may be considered the first freeway-capable electric car to be sold in quantity. It carries a similar price tag to the Mitsubishi i-MiEV, however is a larger vehicle and offers more range and performance.



Figure 2.3: The Nissan LEAF

It is powered by an 80kW synchronous motor with 280Nm peak torque, and drives the front wheels through a single reduction gearbox and differential. Its battery is 24kWh lithium ion, and achieves a range around 120-160km (depending on the standard used).

Since its release it has received many accolades, including the 2010 Green Car Vision Award, the 2011 European Car of the Year, and the 2011 World Car of the Year. It is currently the most efficient EPA-certified vehicle in the United States, with an equivalent fuel consumption of 2.4L/100km. (Although electric vehicles do not use fossil fuels directly, they are recharged from electricity partially generated from fossil fuels, so an equivalent consumption is calculated.)

In many countries around the world, electric vehicles are awarded government subsidies to aid in their adoption. The United States offer US\$7500 subsidy on any new electric vehicles, and in the United Kingdom it is £5000. In Japan the subsidy covers half of the difference between electric

vehicles and an equivalent petrol vehicle – which in the case of the i-MiEV works out around ¥1.2M.

Another attractive feature of electric vehicles is the potential for their battery to be used as a backup power supply if the electrical grid is compromised. Mitsubishi have announced that they will be including 1.5kW inverters in their i-MiEV vehicles, which would allow the vehicle to power home electrical appliances in the event of a grid failure. Nissan has demonstrated a prototype Vehicle-to-Grid (V2G) system working in cooperation with a LEAF, which can export power to the grid. V2G systems have the potential to improve renewable energy penetration by complementing their intermittency.

2.3 FORMULA SAE ELECTRIC VEHICLES

Formula SAE is an international competition which challenges teams of university students to construct and race Formula-style vehicles. The competition has been running since 1978, with vehicles powered by internal combustion engines. In recent years to address environmental concerns, universities have begun to develop electric-powered Formula SAE vehicles as well.

2.3.1 University of Stuttgart's Green Team

One of the most successful Formula SAE Electric (FSE) vehicles was constructed in 2010 at the University of Stuttgart. It went on to win the Formula Student Electric competition in Germany in August 2010, as well as the Italian competition in October. (Green Team: Rennwagen 2011)



Figure 2.4: Uni Stuttgart Green Team's 2010 FSE vehicle

It is powered by dual in-board 47kW synchronous motors, with single reduction drive of 5.5:1 to independently drive each of the rear wheels.

It carries an 8.5kWh lithium ion battery pack weighing approximately 52kg. Total vehicle weight including driver is 268kg, with 48:52 weight balance front to rear. Acceleration from 0 to 100km/h is an impressive 3.3 seconds. The Green Team's vehicle was the fastest accelerating vehicle (including petrol powered vehicles) at the 2010 FSE competition in Germany, proving that electric vehicles can compete directly against petrol vehicles in performance.

2.3.2 RMIT's R10E Formula SAE Electric vehicle

The Royal Melbourne Institute of Technology in Melbourne, Australia was one of the first universities to construct Formula SAE Electric vehicles. Their most recent competition vehicle was the R10E, which competed at FSAE Australasia in December 2010.



Figure 2.5: RMIT's R10E FSE Vehicle

It is powered by dual 30kW brushless DC motors. Its battery pack is lithium polymer from Dow Kokam, with a total capacity of 12.4kWh (155V 80Ah) weighing around 82kg. Total vehicle weight is approximately 320kg, so its power to weight is considerably lower than the Green Team's vehicle, but still sufficient to be competitive.

2.4 FSE AT THE UNIVERSITY OF WESTERN AUSTRALIA

2.4.1 2009/10 Prototype Vehicle

As of 2011, the University of Western Australia has undertaken the development of two Formula SAE Electric vehicles. The first was built in 2009/10, based on a 2001 chassis donated to the Renewable Energy Vehicle (REV) group by UWA Motorsport, and was effectively an electric conversion of an existing vehicle. Since the old chassis was no longer compatible with FSAE

regulations (due to several updated rules), the vehicle could never be used in competition, but it represented a good opportunity to attempt an electric drive system without having to construct an entirely new vehicle.

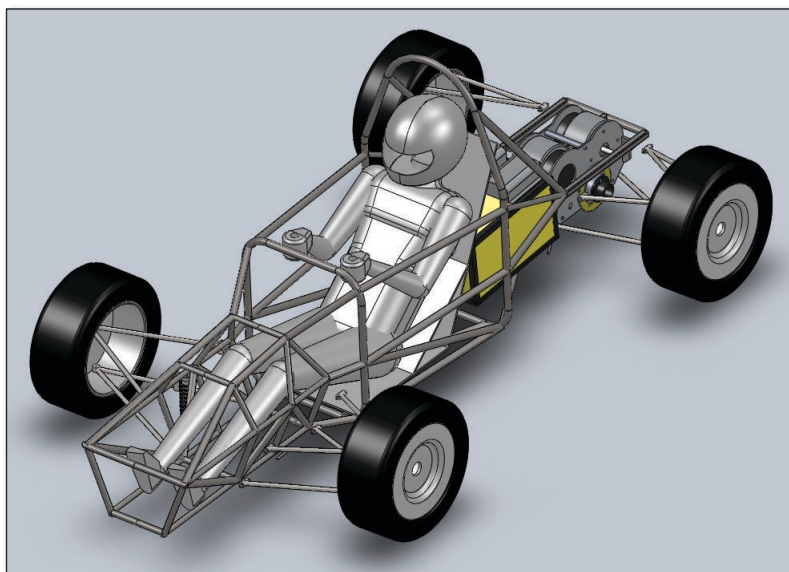


Figure 2.6: CAD render of prototype Formula SAE Electric vehicle

To avoid extensive re-engineering, an in-board drive system was chosen for this vehicle, and existing rear wheel hubs and constant velocity (CV) joints were retained. The following diagram shows the physical layout of electrical components in the vehicle.

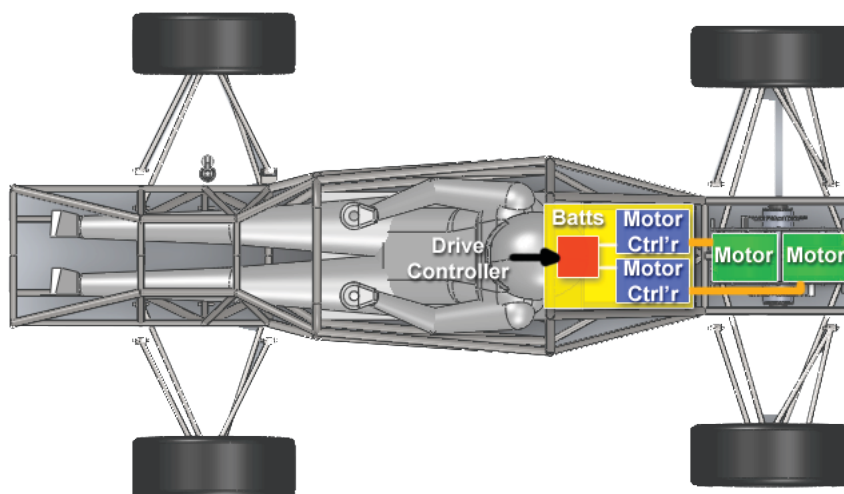


Figure 2.7: Top view of prototype FSE vehicle showing component locations

The following table summarises the electric drive components used in the prototype vehicle:

Table 2.1: Components summary for prototype FSE vehicle

Component	Description
Motors	2x Mars ME0201, 5-15kW PMSM
Motor Controllers	2x Kelly KBL72301, 72V 300A BLDC
Batteries	15x ThunderSky 3.2V 90Ah LiFePO4 (48V 90Ah, 4.3kWh, ~20kW peak)
Battery management	EV Power TS-90 system
Contactors	Gigavac GX14
E-stop	Nanfeng 250A
Throttle	Dual Hall sensor
Brake sensor (for regen)	Dual Hall sensor



Figure 2.8: Prototype vehicle in testing at the race track, early 2010

2.4.2 2011/12 FSE Competition Vehicle

Since the original inherited vehicle could never be used at competition, it was necessary to build a whole new vehicle in accordance with all current FSAE regulations. This was also an opportunity to create a vehicle layout which was better suited to electric drive system. Design commenced in 2010 and construction in 2011. It is intended that this vehicle will be used at FSAE competition(s) in 2012.

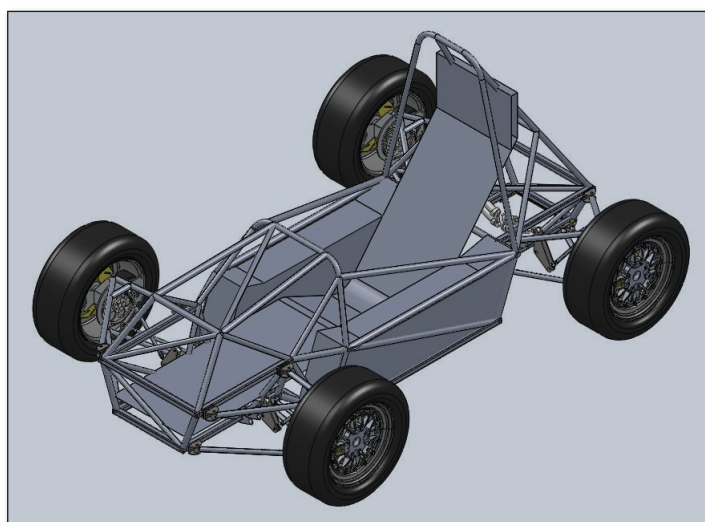


Figure 2.9: CAD render of the 2011/12 Formula SAE Electric vehicle

A major design change was allowing space for a larger battery pack, which would offer more range and power. The batteries are situated either side of the driver for optimal weight balance and minimum polar moment of inertia. With complete design freedom it was decided that the option of in-wheel drive should be explored, as an application for in-wheel motor research. Having no motors or batteries behind the driver freed up a significant amount of space and allowing for a smaller vehicle overall (wheelbase approximately 150mm shorter than the prototype vehicle) which is expected to improve its agility on the race track. The following diagram shows the physical layout of electrical components in the vehicle. The improvements in vehicle space utilisation compared with the prototype vehicle are clear.

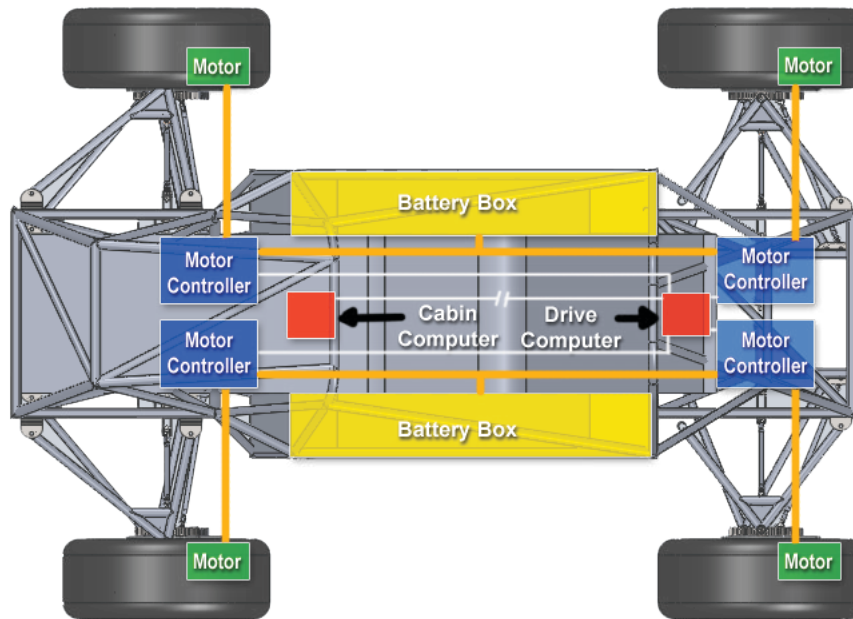


Figure 2.10: Top view of 2011/12 FSE vehicle showing component layout

One significant addition is having a cabin computer and a drive computer. Under FSAE regulations, all cabin electronics must be galvanically isolated from the traction circuit, so one microcontroller is required for reading pedal positions, with optically-isolated communications to a drive computer handling outputs to the motor controllers. The drive computer in this vehicle is also being designed to support traction control and torque vectoring algorithms for optimum performance.

Table 2.2: Component summary for 2011/12 FSE vehicle

Component	Description
Motors	4x Turnigy CA120-70, 5-15kW PMSM
Motor Controllers	4x Sevcon Gen4, 48V 300A SVM
Batteries	640x K2 26650EV, 3.2V 3.2Ah LiFePO4 (51V 128Ah, 6.5kWh, ~60kW peak)
Battery management	Custom designed
Contactors	2x Kilovac EV200
E-stop	2x LV e-stop buttons
Throttle	Dual Hall sensor
Brake sensor (for regen)	Dual Hall sensor
Cabin computer	AVR-based, data logging plug RF telemetry transmission
Drive computer	AVR-based, traction control algorithms for four motor controllers

3 REQUIREMENTS ANALYSIS

3.1 INTRODUCTION

The requirements for electric motors used in vehicle propulsion systems differ greatly from industrial drives, primarily due to the large ratio between continuous requirements vs peak requirements, both in torque and speed. Fortunately electric motors are well suited to this sort of duty. Continuous power ratings in an electric motor are dictated by rate of heat buildup (due to operating inefficiency) vs rate of heat dissipation (via cooling systems etc). However short term power capabilities are only limited by thermal gradients of components in the motor. In most cases, motors can be run at several times their continuous rating intermittently, for example when accelerating a vehicle.

In this section we consider the operating requirements for two potential applications of in-wheel motors, both continuous and intermittent duties.

3.2 POWER AND TORQUE REQUIREMENTS

The power and torque requirements of two vehicles are considered under various common scenarios of operation. The first vehicle is a typical small (1 tonne) road-going car, which represents one of the largest potential applications of in-wheel drive systems.

The second case is a Formula SAE Electric vehicle, which is the practical application of this project. Formula SAE vehicles are much smaller and lighter than regular road-going vehicles, however being open-wheel and open cockpit their drag coefficient is appreciably worse. They do not have a high top speed or hill-climbing requirement, but do need good acceleration to be competitive on a compact race track. Table 2.1 summarises vehicle parameters.

Table 3.1: Reference data for vehicle requirements calculations

Parameter	Typical Small Car	Formula SAE Race Car
Weight	1000kg	300kg
Drag Coefficient, Cd	0.35	0.5
Frontal Area	2m ²	1m ²
Coefficient of rolling resistance, Crr	0.010	0.015
Top speed required	120km/h	100km/h
Acceleration required (0-100km/h)	10 sec	5 sec
Wheel diameter	0.6m	0.5m
Tire friction coefficient	1.0	1.5

Using this data, we can calculate various power, torque and speed requirements for each vehicle as shown in Table 2.2. (See Appendix I for formulae and calculation methods.) A reasonable minimum top speed requirement for both is 100km/h, representing freeway capability for a road-going vehicle, and the maximum speed commonly seen at Formula SAE events. A second datapoint of 60km/h is also shown, representing a more average vehicle speed. Stated torque required represents the combined total from all driven wheels (i.e for 2WD vehicles each wheel will need half of the stated value).

Table 3.2: Power and torque requirements for various driving scenarios

Scenario	Typical Small Car		Formula SAE Race Car	
	Power	Torque	Power	Torque
Maintain 60km/h	3.6kW	64Nm	2.1kW	32Nm
Maintain 100km/h	12kW	97Nm	7.6kW	69Nm
0-100km/h in 10s	39kW avg	833Nm	11.5kW avg	217Nm
0-100km/h in 5s	78kW avg	1665Nm	23kW avg	433Nm
Hillclimb, 10% grade @ 60km/h	20kW	332Nm	7.0kW	105Nm
Limit of traction (accelerating)	–	2943Nm	–	1100Nm

Wheel speed at the maximum speed of 100km/h is calculated to be 884rpm for the small car and 1060rpm for the Formula SAE vehicle.

A 10% grade is a reasonable upper limit for continuous gradients found on public roads, and the results show hillclimbing can be the most power-intensive sustained operation for road-going vehicles. However power and torque required for acceleration are clearly much higher than any continuous duty requirements.

We can also observe that at different speeds, aerodynamic drag and rolling resistance represent varying portions of the speed. Figures 3.1 and 3.2 show this relationship graphically.

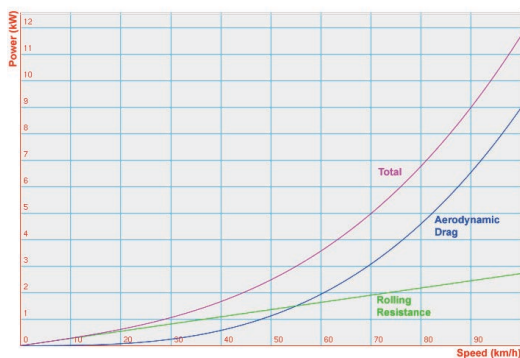


Figure 3.1: Speed-power graph for road-going car

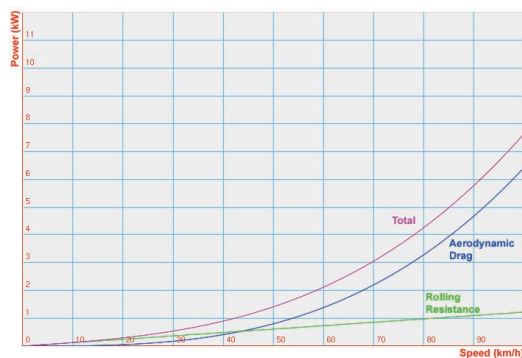


Figure 3.2: Speed-power graph for Formula SAE

At lower speeds the rolling resistance is the dominant factor, but at higher speeds it is aerodynamic drag. For the Formula SAE vehicle, aerodynamic drag is proportionately higher than for the road-going vehicle, since it has a higher drag coefficient and a lot less weight (which affects rolling resistance).

The maximum total torque from all four wheels for the Formula SAE vehicle was calculated at 1100Nm. Based on the maximum load transfer calculated for the vehicle (see Appendix I) this equates to a maximum torque of 423Nm at each back wheel and 127Nm at each front wheel under acceleration, or vice versa under braking.

An interesting observation from this figure is that if two wheel motor were able to provide ~120Nm each to the back wheels, they could cover acceleration requirements for the vehicle, plus all braking duties for the rear wheels – potentially doing away with mechanical rear brakes altogether, if the Formula SAE rules allowed it (which they do not).

3.3 QUALITATIVE REQUIREMENTS

Being close to the road surface, wheel hubs can not be considered a clean environment – particularly for road-going vehicles which travel long distances over various surfaces. In their case, it would be necessary to seal the motor against the ingress of contaminants and water, which rules out convection cooling. For road-going vehicles, it is expected that water-cooling would be required. Fortunately, water has far higher specific heat than air so tends to be much more effective than air (convection) cooling, which would facilitate a high continuous power rating required for hill climbing.

On the other hand, Formula SAE vehicles tend to be used solely on carefully-maintained race tracks, are used for far shorter distances, and have far shorter service intervals. Therefore for Formula SAE vehicles it seems viable to use convection cooled motors.

Since in-wheel motors are unsprung (other than compliance of the rubber tires), they may be exposed to significant vibration so would need robust construction. Also since the stator and rotor are separated by a very small air-gap, they would need to be rigid enough that gyroscopic forces could not cause enough distortion for interference.

Lastly, for the sake of passenger comfort, it would be desirable to minimise motor cogging (torque ripple) which may transmit noticeable unwanted vibrations through the vehicle.

3.3.1 Requirements Summary For Formula SAE Electric Vehicle

For this project the Formula SAE vehicle requirements are of primary interest, though the findings will be applicable to road-going vehicles as well. The basic performance requirements here are a wheel speed of 1000rpm, and 50Nm torque per wheel (assuming a 4WD solution) – though as with any race application, the higher the better. Convection cooled motors should be acceptable.

4 MOTOR THEORY REVIEW

4.1 ELECTROMAGNETIC FUNDAMENTALS

4.1.1 Fundamental Equations

Before analysing any existing in-wheel motor designs or attempting to create any new designs, it is important to have a good understanding of electric motors and the physics behind them. Almost all motors rely on the interaction of electrical currents flowing in magnetic fields. The force on a charged particle in an electromagnetic field was first explored in the 18th century. It became known as the Lorentz force, represented by the formula:

$$\mathbf{F} = q[\mathbf{E} + (\mathbf{v} \times \mathbf{B})] \quad (1)$$

(Quantities in boldface are vectors.) The first term in the square brackets \mathbf{E} is the electric field, the second the magnetic field, which is the cross product of the velocity and the magnetic field density, hence acting perpendicular to the field. Since current flow in a conductor is actually the movement of electrical charge, and amperes of current are simply coulombs per second, on a macroscopic scale the effect of a magnetic field on a current-carrying conductor is:

$$\mathbf{F} = \mathbf{IL} \times \mathbf{B} \quad (2)$$

In the 1830s, Michael Faraday introduced his law of induction, which states that the induced electromotive force in a circuit is equal to the rate of change of magnetic flux through the circuit.

$$\nabla \times \mathbf{E} = \frac{\partial \mathbf{B}}{\partial t} \quad (3)$$

A useful derivation of Faraday's law of induction relates flux density B , conductor length L and velocity V with induced voltage ε , sometimes known as the flux cutting equation:

$$\varepsilon = \mathbf{BLV} \quad (4)$$

Faraday's law of induction is related to Lenz's law, which states that an induced electromotive force (EMF) always gives rise to a current whose magnetic field opposes the original change in magnetic flux – the magnetic equivalent of Newton's third law, and showing that conservation of energy is being obeyed.

In the 1860s the laws relating electricity and magnetism were consolidated by James Maxwell and are commonly referred to as Maxwell's Equations. They basically describe the transfer of energy between electrical form and magnetic form. Current flow in a conductor creates magnetic field which interacts with any magnetic field around it.

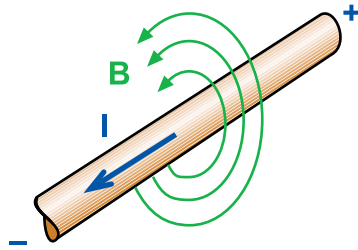


Figure 4.1: Electric current produces a magnetic field

Magnetic flux is a measure of the amount of magnetic field in a given area, and is represented by the symbol Φ with units weber (Wb). Diagrammatically, flux is often drawn using lines to represent the path and density of flux, though in reality flux is of course a continuous field.

It is related to magnetic flux density \mathbf{B} , with units Tesla (T) or webers per square metre, according to the following formula:

$$B = \frac{\Phi}{A} \tag{5}$$

Magnetic flux itself exists due to the presence of a magnetic field, with intensity H :

$$H = \frac{\text{MMF}}{L} \tag{6}$$

The magnetic field and the magneto-motive force (MMF) are related through reluctance R of the magnetic circuit, according to the following formula. It is analogous to Ohm's Law ($V = IR$) in electrical theory.

$$\text{MMF} = \Phi R$$

Reluctance is useful for calculating the quantity of magnetic flux generated in a given magnetic circuit. It is related to a physical property of materials called magnetic permeability, μ , which is covered in more detail in section 2.1.2.

$$R = \frac{L}{\mu A} \quad \text{or } R = \frac{L}{\mu_r \mu_0 A} \tag{7}$$

Figure 4.2 shows how a magnetic field is distorted around current-carrying conductors, and the resulting forces involved. It also represents a very basic model of an electric motor, where opposite movement (hence rotation) is induced in the two conductors due to an excitation voltage.

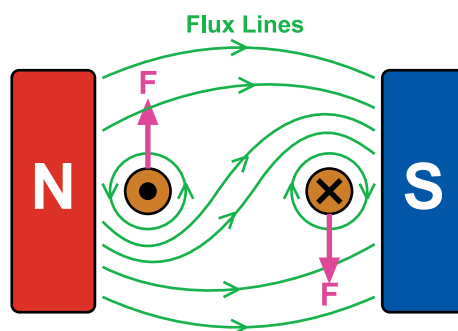


Figure 4.2: Conductors in a magnetic field distort flux and induce forces

Important note: It is convention to show the polarity of magnets with respect to the side facing the air gap between the magnets. In fact, magnetic monopoles (such a North pole by itself) do not exist, and the two magnets shown above would necessarily also have the opposite pole on their outer sides.

4.1.2 Magnetic Permeability

Magnetic materials are often described in terms of their permeability. Permeability can be thought of as *conductivity for magnetic flux*. Materials with high permeabilities allow magnetic flux through more easily than others. Permeability relates magnetic flux with field strength according to the formula:

$$\mathbf{B} = \mu \mathbf{H} \quad (8)$$

The constant μ_0 represents permeability of a vacuum and has a value of $4\pi \times 10^{-7}$ H/m. Most materials have linear B-H curves (i.e constant μ value) almost identical to that of a vacuum. Their permeability is often stated relative to the permeability constant of a vacuum, according to:

$$\mathbf{B} = \mu_r \mu_0 \mathbf{H} \quad (9)$$

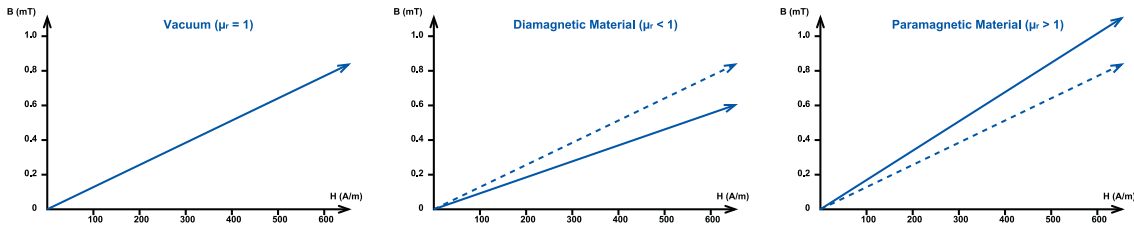


Figure 4.3: B-H curves for vacuum, diamagnetic or paramagnetic materials (Reproduced from Clarke 2008)

Materials with higher permeability (μ) than a vacuum are known as paramagnetic. Materials with lower permeability are known as diamagnetic. The nature of paramagnetic materials causes them to be attracted to magnetic fields, whereas diamagnetic are actually repelled. In most cases diamagnetism is too weak to be observed, but an extreme case is seen in superconductors, which have perfect diamagnetism as a result of their zero resistance; this is called the Meissner Effect, and can be used for superconducting levitation.

The most important class of magnetic materials is the *ferromagnets*, which includes iron, nickel, cobalt, manganese, and their compounds. These materials have a non-linear permeability which is best displayed on a B-H curve. Figure 4.4 shows the B-H curve of three common ferromagnetic materials.

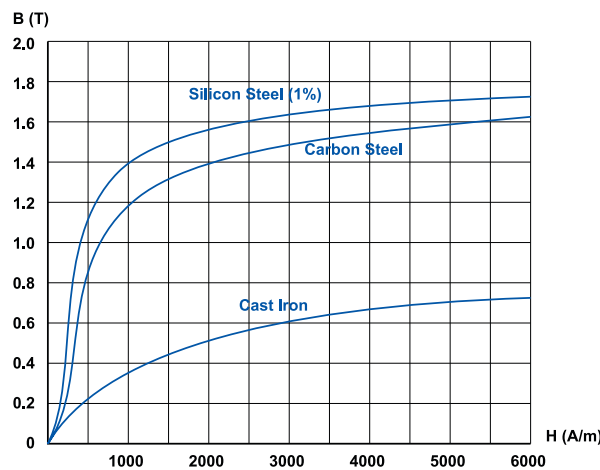


Figure 4.4: B-H curves of three common ferromagnetic materials (reproduced from Wildi 2002)

The B-H curve of ferromagnetic materials show a rapid rise – a relative permeability in the order of 10^4 – which then tapers off to an upper limit as the magnetic field intensity increases, a phenomenon known as “saturation”. Silicon steel has among the highest saturation point of around 1.8T. The very high permeability of ferromagnetic materials is why they are commonly used as magnetic substrates in electric motors, to maximise magnetic flux density.

4.1.3 Remanence, Coercivity and Hysteresis Losses

Coercivity and remanence are both related to the tendency for some ferromagnetic materials to retain a magnetic field after an externally applied field is removed. To be precise, remanence is the flux density which remains, denoted by B_r with units T (tesla), and coercivity is a measure of the field strength which must be applied to reduce the remnant flux to zero, and is denoted as H_c with units Am^{-1} .

In magnetic terms, “hard” and “soft” are sometimes used to describe materials with high and low coercivity respectively. Typically, materials with high coercivity tend to have low magnetic permeability, and vice versa. For any components in a motor which experience changes in magnetic field (such as the iron), a low remanence and coercivity is desirable for optimum efficiency.

Hysteresis losses in a motor are related to the magnetic remanence observed in most ferromagnetic materials. In practice, the energy required to reach a certain field strength in the material is greater than the energy released when the field collapses, resulting in some energy loss each cycle.

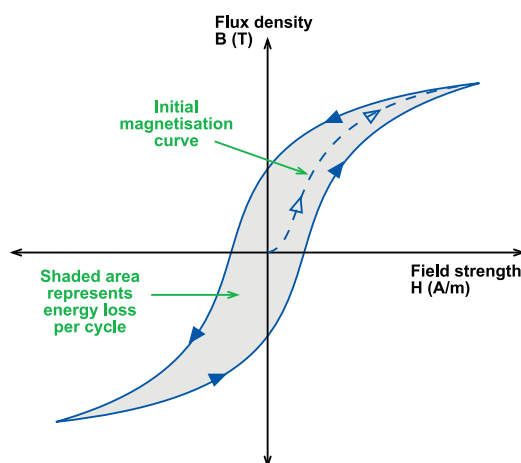


Figure 4.5: Hysteresis loop for magnetisation cycles in ferromagnetic material (Reproduced from Clarke 2008b)

Hysteresis power loss is given by the formula:

$$P_h = K_h f B^n \quad (10)$$

Where ‘n’ is the Steinmetz exponent, which varies for different materials but is typically around 1.6 for iron, and K_h is a constant relating to the material remanence. Clearly, magnetic materials with low remanence have lower hysteresis losses making them preferable for any components experiencing an oscillating magnetic field.

4.1.4 Eddy Currents

Sometimes called Foucault currents after their discoverer, Léon Foucault, eddy currents occur in any electrical conductor in relative motion to a magnetic field. These induced currents cause resistive heating in components and can be a major source of energy loss in electromagnetic machines such as motors. The eddy currents also have their own magnetic field which oppose the motion (Lenz's Law) and act to slow the motor.

Unfortunately most ferromagnetic materials used in motors are also electrically conductive and suffer from eddy current losses. However there are various methods of reducing electrical conduction without greatly reducing magnetic permeability. The most common is to use laminations parallel to the magnetic field, separated by a thin electrical insulator. The result if this is to reduce electrical conduction paths within the material, as shown in Figure 4.6.

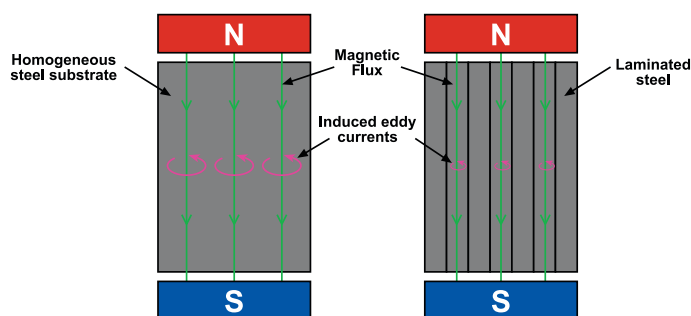


Figure 4.6: Use of laminated steel reduces electrical conduction paths and hence eddy currents

Eddy current losses are proportional to the square of the frequency plus the square of the conductor width – hence, the thinner the laminations the better, within reason. Typical lamination thicknesses used in commercial motors vary from 0.25mm to 1mm.

Another option is to modify the alloy or structure of the material to raise its electrical resistivity, such as using iron dust cores (often called ferrite cores), which are composed of iron powder bonded with electrically-insulating substrate such as epoxy. These are very effective at reducing eddy currents so are commonly used in high-frequency applications, but have significantly lower magnetic permeability than solid cores so are uncommon in motors (where electrical frequencies are usually under 1KHz).

Eddy currents are also observed in the copper windings of a motor. As well as the same resistive heating effect seen in the steel core, in conductors it also gives rise to the 'skin effect', whereby induced currents resist the flow of current in the centre of a conductor, and only the outer parts of the conductor (the skin) carry the current. This increases the effective resistance and hence

resistive losses.

The solution to both these problems is the use of ‘Litz wire’, which involves using individually-insulated strands of conductor to prevent eddy current conduction through the bundle.

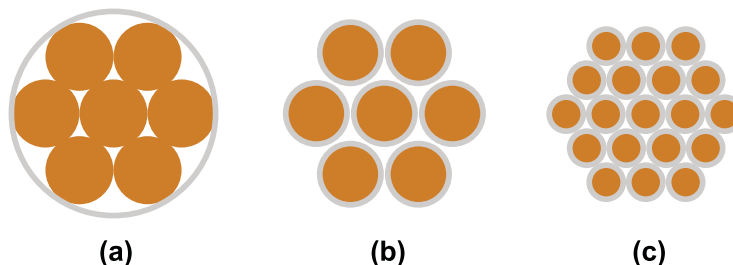


Figure 4.7: Litz wire, (a) regular copper bundle (b) Litz wire (c) finer wires for high frequencies

The downside with Litz wire is the reduction in copper fill factor, due to the space taken by the insulation material. As can be seen in Figure 4.7, progressively higher conductor subdivision results in increased area for insulator and hence less conductor area. As such selection of Litz wire is a balancing act between reducing eddy current losses, and increased resistive losses due to a reduction in conductor area. Greaves et al (2003) suggest a typical value of approximately 25% reduction in conductor area for Litz wire use in motor applications (<1kHz frequencies).

In some high frequency applications, it can actually be most economical to simply use hollow conductors, which both reduces eddy current losses and negates the skin effect (Sullivan 2001), but of course copper fill factor is significantly reduced.

4.1.5 Saliency and Cogging Torque

Saliency in a motor refers to whether or not there are salient poles – in effect, whether the airgap width varies around its circumference. Saliency results in varying magnetic reluctance for the flux circuit between rotor and stator as the rotor turns. As such, there are higher and lower energy states for the magnetic field. This variation results in torque ripple while the rotor is spinning, also known as cogging torque.

Cogging torque is undesirable in many applications including drive systems in passenger vehicles, where it can introduce vibration into the drivetrain.

4.1.6 Efficiency

Electric motors are very efficient compared with many other machines, but maximising operating efficiency is always desirable. This can be done through an understanding of the sources of energy loss, and optimising designs to minimise them.

High efficiency is partly important for performance, but also for cooling requirements. Typical electric motors are 85-95% efficient, and while this only represents a 10% difference in efficiency, it represents a three-fold range in *inefficiency*, and hence the amount of cooling required to remove heat.

Copper loss, or winding loss, is the largest source of inefficiency in many designs, and describes energy lost as heat due to electrical resistance of the wire used for windings (almost always made of copper, hence the name). It is the only source of loss that is independent of motor speed (frequency) – only RMS current.

A common metric for motors is the current density in the conductors, with units Amm^{-2} . This is commonly in the range of 3.5 Amm^{-2} for uncooled equipment (e.g sealed motors) or 10 Amm^{-2} for convection cooled motors. Some water cooled designs can sustain significantly higher current densities again.

The other main source of inefficiency in most motors is iron losses, which is the collective name for both eddy current losses and hysteresis losses in the core. Both of these losses are proportional to frequency (motor speed). These are minimised by using a core material with low remanence, and high electrical resistivity – often achieved using thin laminations.

Some other, smaller sources of loss in electric motors include magnetostriction (the distortion of materials due to magnetic forces), electromagnetic radiation (field leakage), windage (aerodynamic drag on the rotor) and dielectric loss in materials used to insulate the core and windings. All three of these combined typically account for under 1% of a motor's power consumption.

4.1.7 Pole Count

The pole count in a motor refers to the number of magnetic poles around its circumference. It will always be an even number, since there are always north-south pairs.

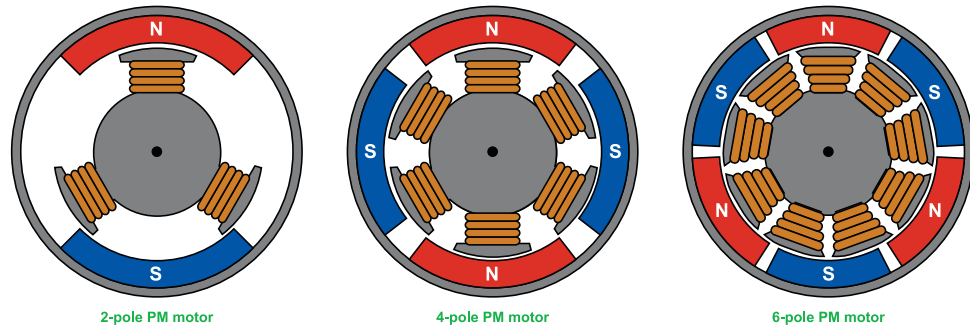


Figure 4.8: Illustration showing typical example of 2, 4 and 6 pole permanent magnet motors

In the case of 3-phase motors, the number of pole pairs (usually) gives the ratio of electrical excitation frequency to mechanical frequency. For example a four pole motor will need the magnetic field induced by the stator to rotate through 720° for the rotor to turn 360° .

In general, increasing the pole count will result in a higher torque motor, since the rate of change of flux for a given rotor speed increases proportionately.

A disadvantage with high pole-count motors is increased iron losses (eddy currents and hysteresis) at a given RPM, since they are proportional to electrical frequency. A “rule of thumb” upper limit for laminated electrical steel is about 1kHz, before iron losses become prohibitive.

4.2 TAXONOMY OF ELECTRIC MOTORS

Figure 4.9 provides a taxonomy of five common types of electric motor. The first criteria is the type of commutation (i.e how the rotating magnetic field is produced), either by a mechanical commutator in the motor or by AC current (typically 3-phase). The second level relates to differing types of stator (for DC motors) or rotors (for AC motors).

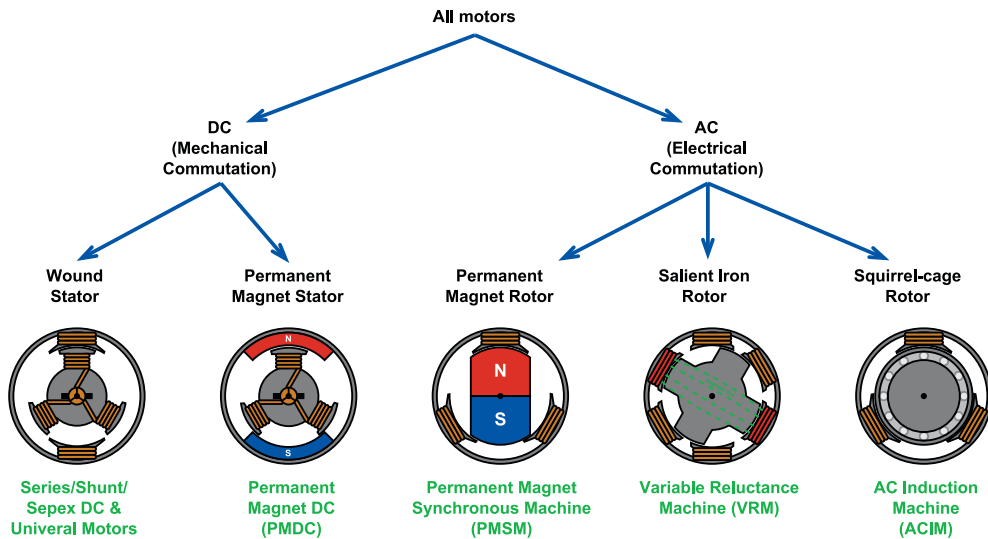


Figure 4.9: Taxonomy of five common types of electric motor

More information about each type of motor is provided in sections 2.2.1 to 2.2.5.

4.2.1 Permanent Magnet Direct Current (PMDC) Motors

PMDCs are one of the oldest types of motor. They use permanent magnets in the stator to set up stationary magnetic field, and pass current through conductors in the rotor to create a torque and hence rotation. Continuous rotation is achieved using a commutator. A commutator consists of fixed brushes in contact with a rotating segmented cylindrical conductor with electrical connections to each winding, such that as the rotor turns the commutator provides conduction to each rotor winding in sequence.

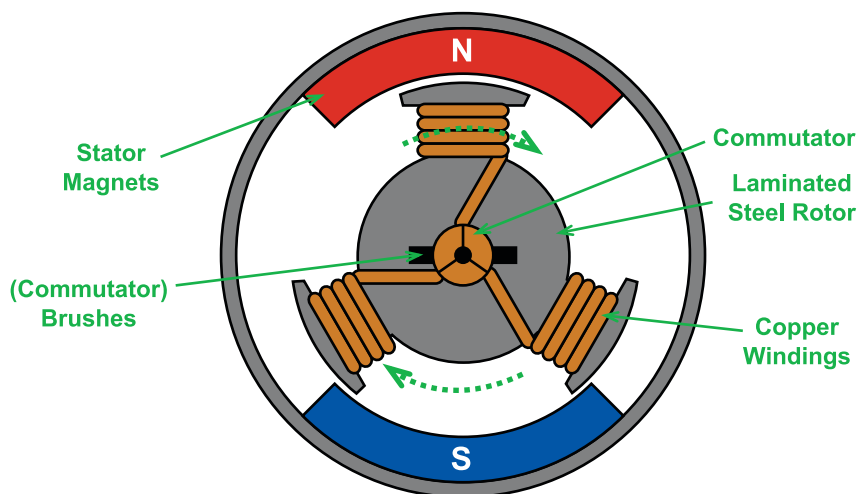


Figure 4.10: Typical brushed/commutated DC permanent magnet motor (2-pole, inner-rotor, radial flux)

Note: Dashed arrows in the diagram simply indicate which parts rotate – most electric motors can operate in either direction.

PMDC motors have historically been most common in small applications, under around 1kW. They are a relatively simple motor to construct, but until the proliferation of rare earth magnets in the 1980s, permanent magnets couldn't offer as strong a field strength as wound stators. Also the cost of large permanent magnets remains high.

Typical operating efficiency is around 85-90%, with a significant portion of the losses attributable to the commutator, and also low copper utilisation (commutator brushes often only energise a portion of the rotor windings at any time).

4.2.2 Dual-wound DC Motors

Many variants of motor use electromagnets for generating both stator and rotor fields, known as dual-wound motors. The main variants are classified according to how the stator and rotor are wired electrically, namely Series DC (windings in series), Shunt DC (windings in parallel) or SepEx (windings are separately excited). The physical topology of all three is basically identical.

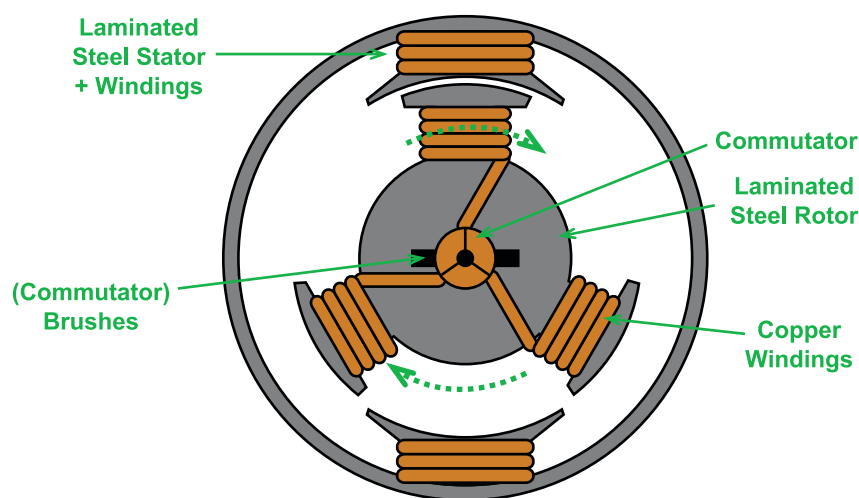


Figure 4.11: Typical wound-stator DC motor (2-pole, inner-rotor, radial flux)

Since the polarity of both stator and rotor swap for negative voltages, rotation direction remains the same for positive or negative voltages. A useful symptom of this is that they can operate from either DC or AC power, sometimes called Universal Motors.

Dual-wound motors have historically been one of the most popular topologies, more cost-effective than PMDC motors for large mobile applications such as electric vehicles, and as Universal

Motors in single-phase AC equipment such as power tools.

Efficiency is typically around 85-90%, similar to PMDC motors. Although there can be extra resistive losses in the stator windings, field strengths are typically higher which results in more electromotive force per unit current, so the result is a similar overall efficiency.

4.2.3 AC Induction Motors

Sometimes called “squirrel cage” motors after the shape of the rotor conductors (which resembles a cage), the invention of AC Induction motors is attributed to Nikola Tesla (1883). Its operation can be a little difficult to conceptualise, but in brief they employ a wound stator with rotating magnetic field, and use electromagnetic induction to induce current flow in conductors in the rotor and hence generate its own a magnetic field. The induced rotor field resists the relative movement between stator and rotor fields (Lenz’s Law) which causes the rotor to follow the stator field.

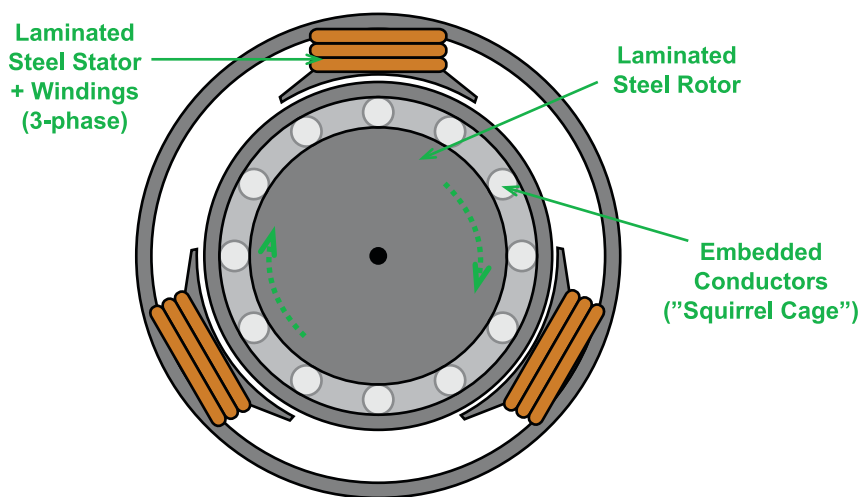


Figure 4.12: Typical AC induction motor with “Squirrel Cage” rotor

Of course, if there was no relative movement between rotor and stator, there would be no current induced in the rotor and hence no torque. So the actual speed of the rotor is always slightly slower than the electrical excitation frequency creating the rotating magnetic stator field. This difference is referred to as “slip”, and makes them an asynchronous motor.

AC Induction motors are most popular in industrial applications where they are driven off 3-phase power. They are relatively easy to construct and with no commutator, they are both more reliable and more efficient (typically 90-95%) than DC or Universal motors.

Whilst it is possible to build AC induction motors with more than three phases (Lyra & Lipo 2001)

the vast majority in use are three-phase because it is considered the best compromise between performance and complexity, and can be operated directly from industrial 3-phase power.

In recent years the progress of Variable Frequency Drives has also enabled them to be used in variable speed applications, and to be run from DC power. They are a good candidate for use in electric vehicles, and as 3-phase motor controllers come down in price, ACIMs are starting to replace DC motors in many applications.

4.2.4 Variable Reluctance Motors

Also known as Switched Reluctance or Synchronous Reluctance motors, variable reluctance motors consist of a salient iron rotor with neither conductors nor permanent magnets, and a set of stator poles. They make use of magnetic reluctance to produce torque. When a pair of opposing stator coils are energised, a magnetic flux path is created in the rotor, and forces are induced in the rotor to align it with the path of least reluctance / maximum flux linkage (as shown in Figure 4.13).

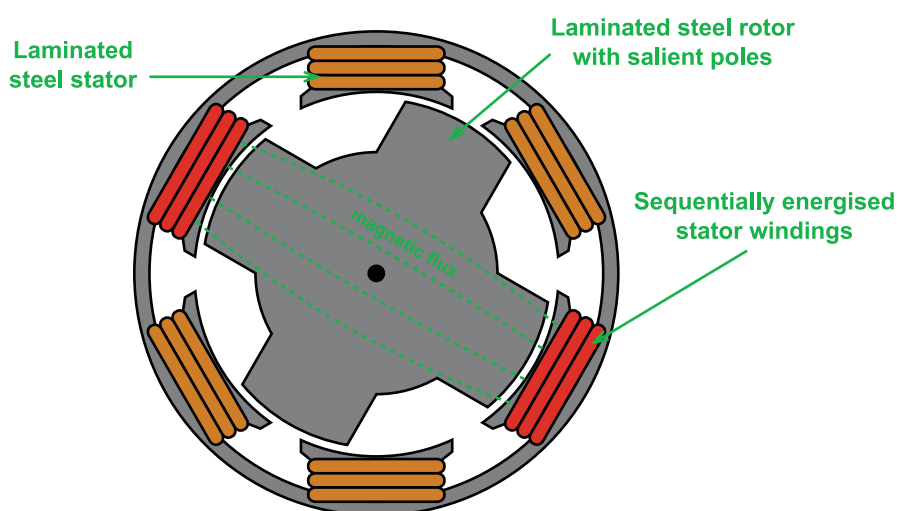


Figure 4.13: Example of a Variable Reluctance motor design

The basic concept has been in existence since electric motors were first introduced, but hasn't been very common until recently, since control techniques can be complicated (Wadnerkar, Das & Rajkumar 2005).

The primary advantages they offer are simple, rugged construction, fault tolerance, and low cost. The disadvantages are relatively low efficiency (usually <90%), high torque ripple, acoustic noise, complex control algorithms, and EMI noise emission (Wang et al 2005).

4.2.5 Permanent Magnet Synchronous Motors (PMSMs)

PMSMs consist of a rotor with a number of permanent magnets, and a stator with phase windings providing a rotating field which the PM rotor follows. They are an electronically commutated synchronous motor, meaning the controller must create a rotating magnetic field (usually 3-phase) in sync with the rotor. The concept was first described in a 1962 paper by engineers T.G Wilson and P.H Trickey, but as with variable reluctance motors the more complex control of electronic commutation meant they did not become commercially competitive until the late 1980s.

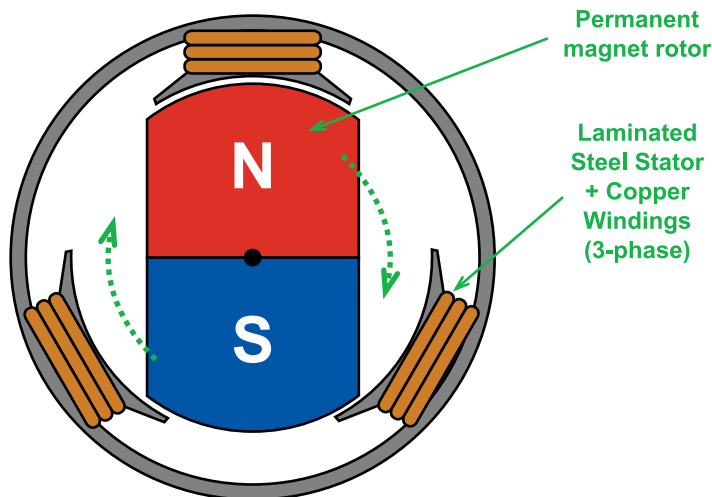


Figure 4.14: Example topology of a PMSM (2-pole, inner-rotor, axial flux)

As discussed by Mevey (2009), there are a plethora of different names given to this motor topology. The most common are Brushless DC (BLDC) and Permanent Magnet Synchronous Motor (PMSM). Often the use of these two terms depends on the control system for the motor (Colton 2010), where BLDC implies trapezoidal electronic commutation and PMSM implies multiphase sinusoidal drive (see chapter 3 for more information on electronic motor control techniques). However the term PMSM will be used here, since it is considered a more accurate description of the topology.

The vast majority of motors for other topologies have a rotor which spins within a stator, known as inner-rotor radial flux. However PMSMs are often constructed in different arrangements, such as outer-rotor radial flux or axial flux, aka “pancake” motors.

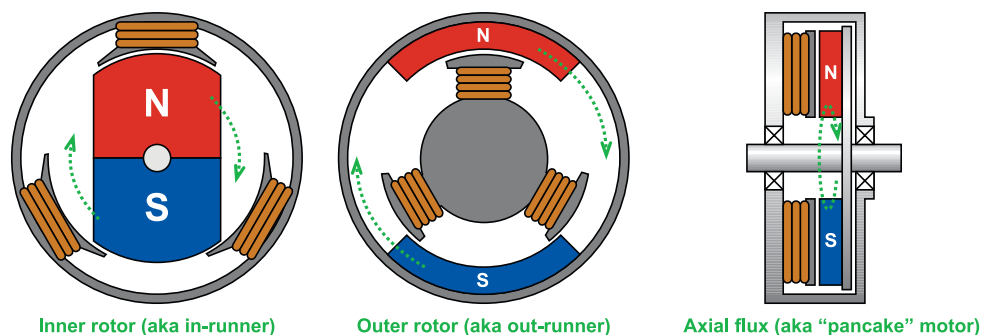


Figure 4.15: Three common topologies for PMSM motors: Inner rotor, outer rotor and axial flux

Each topology has its own advantages in certain applications. Outer-rotor PMSMs can be constructed with fairly thin rotors, which results in a very large airgap radius compared with the overall motor diameter, to maximise torque production – though sometimes it is not convenient having the outside of a motor spinning.

Axial flux motors are constructed with a rotor ring and stator ring side-by-side along the rotating axis, with air gap magnetic flux parallel to the axis of rotation - hence the name axial flux. These are most commonly used in applications where their aspect ratio (shorter body and larger diameter) is beneficial.

Because the rotor field strength is constant, PMSM motors exhibit a linear relationship between excitation voltage and rotor speed, since the back-EMF is always proportional to speed. The constant relating the two is known as the motor speed constant, represented as K_v . Similarly due to conservation of energy, the current flow in the rotor is proportional to the torque produced according to the reciprocal of the speed constant, and known as the torque constant K_t .

PMSMs are frequently cited as having (potentially) the highest power density and efficiency, typically around 95%.

The two main disadvantages of PMSM are (typically) high cogging torque due to iron saliency, and the high cost of high-strength permanent magnets. Another disadvantage is lower operating temperature range compared with wound motors, due to the potential for demagnetisation of permanent magnets at high temperatures. This can occur simply from rotor heating due to eddy currents, including within the magnets themselves (Zhang, Wen & Wang 2010)

4.3 HALBACH ARRAYS

Halbach Arrays are an arrangement of permanent magnets which result in an asymmetric magnetic field. The concept was introduced in the late 1980s by Klaus Halbach, a physicist at the Lawrence Berkeley National Laboratory, for the purpose of focusing particle accelerator beams (Wikipedia: Halbach Arrays).

Halbach Arrays have two advantages: The field is twice as large on the side which flux is confined (in the ideal case), and minimal stray field is produced on the opposite side, which helps with confinement (reduced flux leakage).

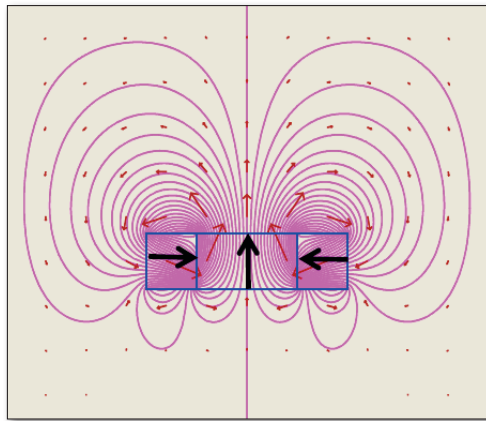


Figure 4.16: Asymmetric magnetic field around 3-magnet Halbach array (Copied from Volk 2008)

In practice this means motors can be constructed without the use of magnetic materials other than the permanent magnets – there is reduced need for the use of iron to contain/conduct magnetic fields. With careful design it can also improve uniformity in the field strength, which can help reduce cogging torque (Merritt et al 1994). Halbach Arrays have been successfully used in many high-efficiency low-iron motor designs.

4.4 VERNIER DRIVE MOTORS

“Vernier drive” refers to electric motors where changes in the electrical angle cause only incremental rotation in the rotor. It is commonly seen in both PMSM and Variable Reluctance designs, and is sometimes called “magnetic gearing”.

All else being equal, as rotor speed steps down, motor torque steps up. As such vernier drive designs are attractive in applications requiring low speed and high torque, and where mechanical reduction gearing is undesirable (Lee 1963). Furthermore by using fractional number of slots per pole, cogging torque can be greatly reduced (Tseng & Chen 1997). The concept has existed for a

long time but was neglected in early days due to poor power factor (0.15 to 0.2) when used with conventional AC supplies (Rhodes 1977). Recent advances in motor controller technology have resolved this shortcoming.

Vernier drive motors are distinct from normal multipole motors, where electrical frequency is a multiple of mechanical rotation frequency. For example, a typical 3-phase motor with 12 slots/windings will have a ratio of electrical to mechanical frequency of 4:1. Vernier drive motors have a significantly higher reduction ratio.

The most widespread example is the stepper motor, which is may be described as a vernier drive switched reluctance motor. However it can also be applied to permanent magnet synchronous motors, the most common example of which is the “LRK” design (an acronym of it’s inventors Lucas, Retzbach and Kühfuss), which has become very popular in motors for electric aircraft.

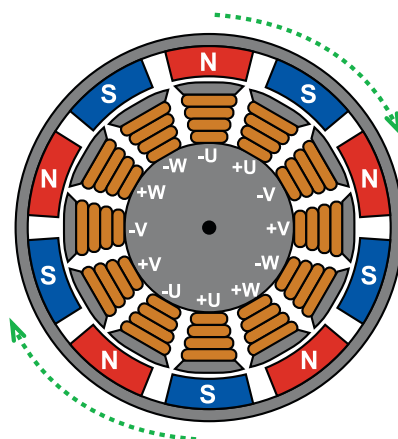


Figure 4.17: Common example of a 10-pole 12-slot outer-rotor LRK, a PMSM vernier drive motor

The standard LRK design has 12 stator slots/windings and either 10 or 14 permanent magnet poles, such that the number of windings to poles varies by two (one pair of poles). As visualised in Figure 4.17, at any time there can only be one winding pair aligned with a rotor pole pair. Adjacent windings/poles are only slightly misaligned. As such if the windings are sequentially energised the rotor only moves incrementally with each step. The short physical distance between energised windings and associated magnetic poles facilitates high magnetic forces and hence torque.

The general formula for pole count in a vernier motor is given by: (Lee 1963)

$$N_1 = N_2 \pm P \quad (11)$$

Where N_1 is the number of stator slots (poles), N_2 is number of rotor slots/magnets, and P is the number of pole (pairs) of the rotating magnetic field. The ratio of the mechanical frequency to

electrical frequency is then given by $\mathbf{P} / \mathbf{N2}$.

Hence, in theory, torque is $\mathbf{N2} / \mathbf{P}$ times higher than an equivalent conventional PM motor. Ishizaki et al (1995) confirmed this formula for torque amplification of magnetic gearing, and presented a motor design yielding 112 kNm/m^3 – a major improvement over typical figures for common industrial AC induction motors at about $15\text{-}30\text{kNm/m}^3$.

Toba & Lipo (1999) presented an axial-flux vernier drive motor design based on a stator ring between concentric rotor rings. As well as a high torque density they noted a very low cogging torque, which is a result of fractional slot-width-to-pole ratio. In other words, there are no regular intervals where stator slots line up with rotor magnet poles.

In general, the higher the least common multiple between number of rotor poles and number of stator slots, the lower the cogging torque (Güemes et al 2008). However having fractional slots per pole does increase fundamental order (deformation of the waveform of magnetic flux density in the airgap) since stator slots are misaligned with rotor magnets.

A major advantage of this type of motors is the ratio of slots to poles. In most 3-phase PMSM motors, number of slots/windings to poles are in the ratio of 3:2. For high pole count motors this results in a very narrow slot pitch, which quickly reaches feasibility limit due to small slot width-to-depth ratio, which reduces slot filling factor and increases slot leakage (Zielinski & Schoepp 1991). Additionally it makes winding (manufacturing) more difficult. In contrast such vernier motors have slot width fairly close to pole pitch regardless of the pole count.

A further advantage is the absence of lap windings – which refers to windings coupling nonadjacent slots. End windings represent inactive copper, so reducing their length increases copper utilisation and reduces resistive losses in the motor (Meier 2008).

4.5 MOTOR CONTROL REVIEW

4.5.1 Introduction

Particularly since the proliferation of variable speed 3-phase motors, the behaviour of motor controllers is integral to the operation of the motors themselves. Although an in-depth analysis of motor controllers is beyond the scope of this thesis, it is valuable to review the basic operation of motor controllers for different types of motor in order to understand how they work together.

It can also help understand how the limitations of one effect the other, such why 3-phase is considered the best trade-off between performance and complexity (of motor controller), and how torque ripple can be minimised by the controller.

4.5.2 Pulse Width Modulation

The fundamental principle behind all modern motor controllers is the use of pulse width modulation to control the flow of power to the motor. It involves switching the voltage supply to the motor at a high frequency (typically $\sim 20\text{kHz}$), and the duty cycle dictates the average voltage seen by the motor.

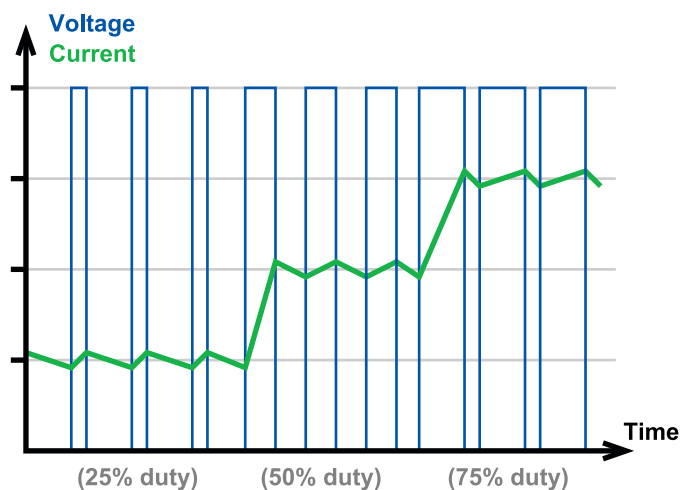


Figure 4.18: Effect of Pulse Width Modulated voltage on motor current flow

Motor inductance causes the current to change slowly compared with switching frequency, resulting in a small amount of current ripple (shown exaggerated in Figure 4.18). In general the switching frequency and motor inductance need to be high enough to avoid significant current ripple, as this can have unwelcome effects on the system such as introducing high frequency harmonics.

Early motor controllers typically used analog electronics to generate the PWM signal and thyristors as power switches. More modern designs (circa 1990 onwards) are usually based on MOSFETs or IGBT type transistors, with PWM signal(s) generated from a microcontroller.

4.5.3 DC Motor Control

Motors with a commutator will rotate when DC voltage is applied to them. Typically such motors are controlled by either a half-bridge for monodirectional control or a full bridge for bidirectional control.

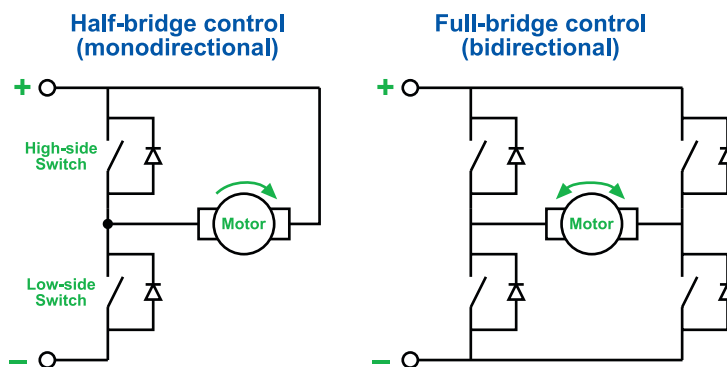


Figure 4.19: Half-bridge and full-bridge control of (mechanically-commutated) DC motors

Most DC controllers will include current sensing and/or speed sensing as feedback, to provide accurate control and to protect the motor. The simplicity of controllers for DC motors is one of the primary reasons for their popularity during the 20th century.

4.5.4 Three-phase Motor Control

Three phase motors are somewhat more complicated to control, since they require the controller to produce a continuously rotating magnetic field via AC excitation of three electrical phases, rather than having a mechanical commutator perform this function.

The simplest three-phase control is trapezoidal, sometimes called 120-degree control or square wave drive. This involves having two phases on at a time in sequence. A more advanced system is to use sinusoidal excitation, sometimes called 180-degree control, where all three phases have a sinusoidal AC voltage apart in phase by 120° .

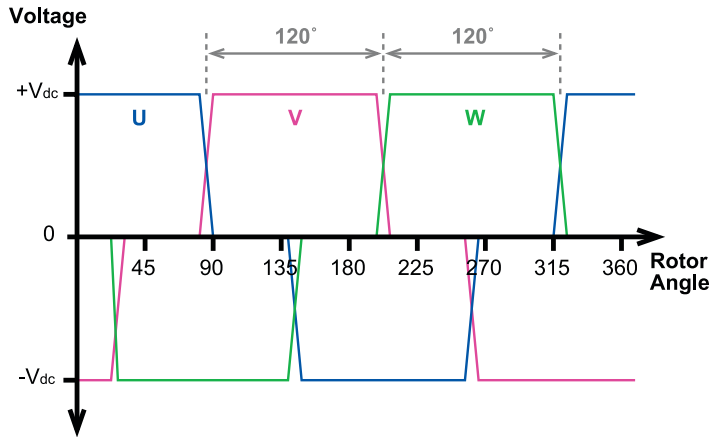


Figure 4.20: Graph of trapezoidal control waveforms

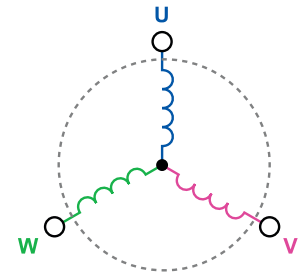


Figure 4.21: 3-phase windings

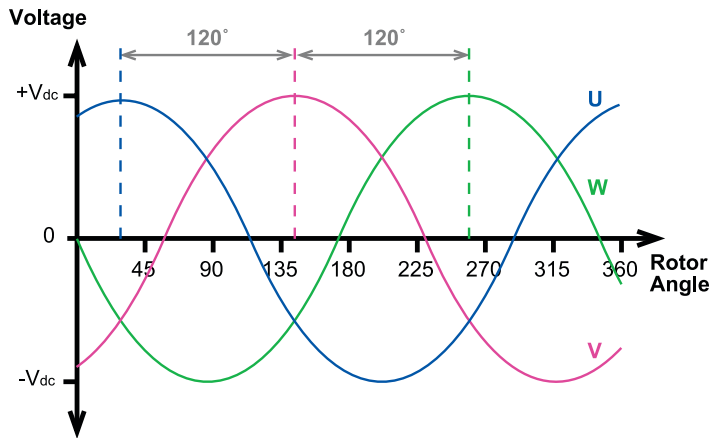


Figure 4.22: Graph of sinusoidal 3-phase voltage waveforms

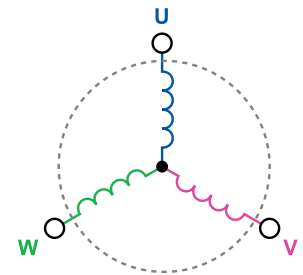


Figure 4.23: 3-phase windings

Three-phase motors are usually controlled by a three-phase bridge, which is effectively three half-bridges – one per phase.

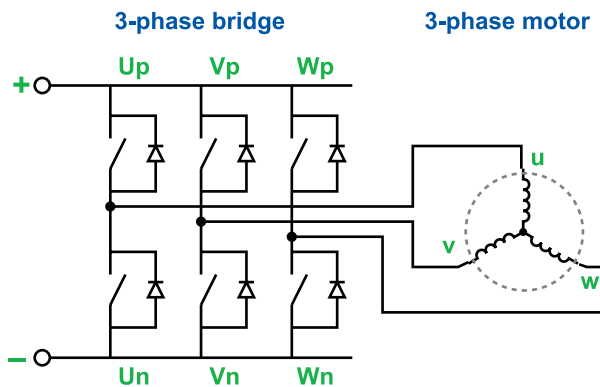


Figure 4.24: Typical circuit for three-phase bridge and motor

Figure 4.25 shows the functional topology of a typical 3-phase motor controller, with throttle input and feedback from the motor enabling the motor model logic to calculate the required voltage vector for the rotor, converted into six PWM signals to drive a 3-phase bridge amplifier (inverter) which in turn energises the stator windings, creating the rotating magnetic field which keeps the motor rotating.

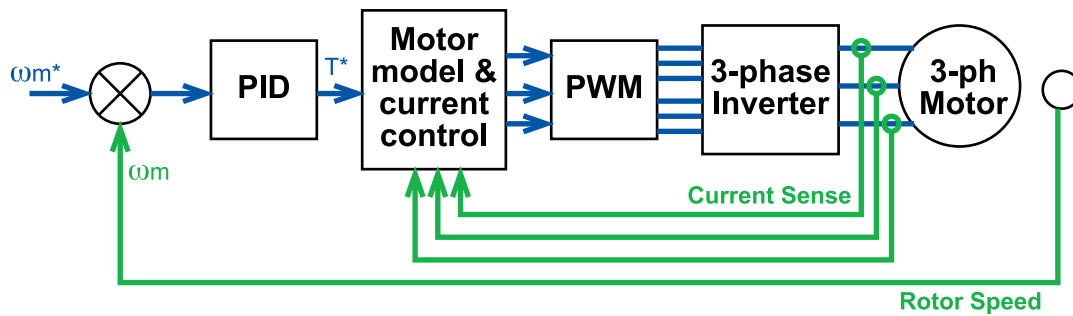


Figure 4.25: Generic 3-phase drive system (Reproduced from Murray, Kettle & Moynihan 1997)

The overall design is applicable to both AC induction and PMSM motor controllers, with different behaviours implemented for the motor model block. Historically such controllers were implemented with analogue electronics, but modern controllers typically employ microprocessors or Digital Signal Processors (DSPs) for superior performance.

4.5.5 Field Oriented Control

Field-oriented control is a more advanced motor control technique used with AC induction or PMSM motors. In brief, its purpose is to optimise torque production by automatically compensating for current phase lag.

A motor winding energised by a sinusoidal voltage also exhibits sinusoidal current flow. However the inductance of the motor windings cause a phase lag in the current waveform, which varies with motor speed and load.

The most efficient torque production is achieved when the rotor field is 90° out of phase with the stator field, so it is of interest to compensate for the current phase lag for optimum performance. This is usually done via current sensors on each phase with zero-crossing detection, allowing the controller to calculate and compensate for phase differences.

4.5.6 Sensored vs Sensorless Control

All synchronous motors require the controller to supply a excitation voltages which are synchronised with the rotor in order for rotation to continue. In most cases this is done using three magnetic Hall Effect sensors spaced 120° apart magnetically, which provide triggers for electronic commutation as they switch.

Sensorless control generally refers to the monitoring of back-EMF to sense appropriate electronic commutation times, rather than through physical rotor position sensors. A more accurate term may be “self-sensing” control (Murray, Kettle & Moynihan 1997).

Various techniques have been experimented with including open loop flux estimators, third-harmonic voltage-based estimators, back-emf waveform detectors, saliency based position estimators, and model-based estimators (e.g Batzel & Lee 2005, Chen & Cheng 2006). The most common by far is back-EMF zero-crossing detection, which only works with trapezoidal/ 120° control since the back-EMF can only be measured on the one phase that is inactive at any given time.

Such sensorless control is unable to measure rotor position when no back-EMF is present – that is, when the rotor is stationary – so the controllers usually need to implement a kick-start algorithm to start the motor turning, which is neither as smooth nor as reliable as physical rotor position sensors. Sensorless control is normally only found in low-cost applications which do not have a starting torque requirement (which rules out traction use), where it’s cost advantage outweighs its performance disadvantage.

5 IN-WHEEL MOTOR SYSTEMS REVIEW

5.1 INTRODUCTION

The potential advantages of in-wheel motor systems has resulted in much research being done in the area. Most has concentrated on the feasibility of direct drive systems, plus a few examples of systems involving reduction drives.

The requirements of motors for traction applications differs significantly from industrial applications, primarily due to high load variations and environmental variations (Nanda & Kar 2006). Historically, commutated DC motors have been the most common type used in traction applications, primarily due to the simple speed control requirements. Also their torque characteristics are suited to traction applications, offering high starting torque. Most were dual-wound motors, since large permanent magnets are quite expensive (despite the efficiency gains their use permits).

Recent advantages in motor controller and power electronics technology has made 3-phase motors a more viable proposition for traction applications, and they have many advantages over DC motors including higher reliability, lower maintenance, and higher efficiency. Also AC drive systems can offer effective regenerative braking, which is very valuable for vehicles.

Chang (2004) believes AC induction motors are the best option for EVs with conventional drivetrains due to their low cost, high reliability, low torque ripple/noise, and absence of position sensors. AC induction motors are also a very mature technology, widely used in industrial applications.

However in-wheel motor systems present some unique technical challenges, in particular the space constraint of fitting a motor inside a wheel hub, avoiding excess unsprung weight, and maximising efficiency to minimise cooling requirements. This requires very high torque, power density and efficiency.

PMSM motors offer approximately double the power density of AC induction (Melfi, Evon & McElveen 2008), as well as better power factor (Halkosaari 2006), lower rotor temperatures due to no rotor conductors, and slightly higher efficiency. As a result PMSM type motors are almost ubiquitous suggested as the best candidate for in-wheel motor systems (Caricchi et al 1996, Cheng, Duan & Cui 2005, Halkosaari 2006, Rajagopal & Sathaiah 2006, Güemes et al 2008, Jian, Xuhio & Lili 2009, etc).

One of the enabling factors in high-power PMSM motors was the development of rare earth magnets, with very high magnetic remanence ($\sim 1.3\text{T}$). Rare earth magnets were first introduced around 1970 based on samarium cobalt (SmCo) alloys, and carried a high cost which precluded their use outside specialised applications. In the 1982, neodymium (NdFeB) magnets were invented which were substantially cheaper to produce than SmCo and were feasible for use in a wider range of products. Early NdFeB magnets were susceptible to demagnetisation at relatively low temperatures, but modern ones offer stability up to 180°C .

In this chapter we review a variety of in-wheel motor systems, both academic research and several commercial prototypes. Most of the designs are based on either axial flux or outer-rotor radial flux PMSM. Some more exotic motor topologies are also explored including spherical motors, transverse flux motors, and variable reluctance motors. Finally some high-performance PMSM motors are reviewed as candidates for in-wheel systems with reduction drive.

5.2 AXIAL FLUX MOTORS

AFPM is one of the most popular motor topologies proposed for in-wheel motor systems. With a large diameter to length ratio, the topology is mainly used in high-torque low-speed applications and the aspect ratio is well suited to fitting within a wheel. Also they offer a significant volume saving over radial flux motors where much of the internal volume does not contribute to torque. Another interesting advantage is the potential for field weakening by changing the airgap thickness, which changes the torque/speed characteristics of the motor and has been used in some solar cars (Oh & Emadi 2004).

Some recent designs of axial flux PMSM wheel motors are presented, firstly some ironless designs which have been commonly and successfully used in some solar cars and small vehicles, then several which make use of an iron core.

Since hub motors for road-going vehicles would be operating in a fairly dirty environment, they would require a high Ingress Protection (IP) rating, best achieved with a totally sealed housing – which precludes effective convection cooling. As such successful in-wheel motors will most likely require water cooling.

Carrichi et al (1996) present a multistage axial flux PM machine with a water-cooled ironless stator. The design features two stator planes with three permanent magnet rotor planes. Stator windings are wrapped around water cooling channels also in the air gap.

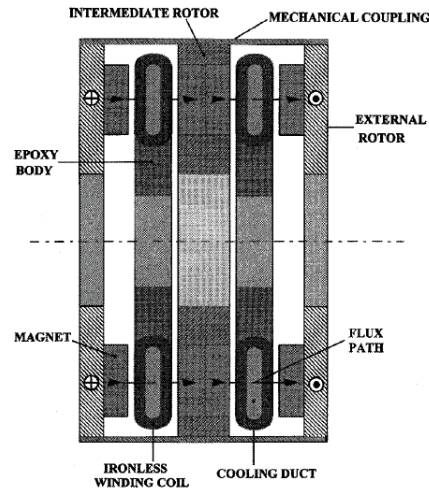


Figure 5.1: Cross section of two-stage axial-flux permanent magnet machine with ironless water-cooled stator winding (Copied from Caricchi et al 1996)

The design yielded 215Nm torque with a rated speed of 1100rpm. An interesting feature of the twin stator design was the ability to perform electrical series/parallel switching of the two stator windings to change the torque/speed characteristics of the motor. Windings in series would have half the motor speed constant K_v but twice the torque constant K_t , which would behave similarly to having two mechanical gears.

A notable downside of this design is the very large air gaps, which would have very high magnetic reluctance resulting in a relatively low magnetic flux density in the airgap.

One of the most well-known and successful applications of in-wheel motor technology was developed by Australia's CSIRO. The design was first presented in 1997 (Lovatt, Ramsden & Mecrow 1997) and subsequently used in the Aurora solar car which won the World Solar Challenge in 1999.

In the world of solar cars, operating efficiency is paramount, which led to the first design decision of a PMSM-type motor. The CSIRO motor is widely accepted as the most efficient wheel motor ever made for solar-car racing, achieving 98% efficiency at rated load. The design uses an axial flux topology since radial flux of equivalent air-gap area would not fit in the narrow wheel area, and features an iron-free design to completely eliminate the iron losses (eddy currents and hysteresis losses) which occur in most motors.

The design basically consists of two rotor rings of magnets in a Halbach Array, with copper Litz wire windings in the airgap between them.

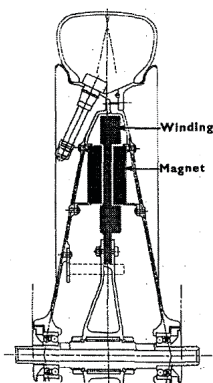


Figure 5.2: Cross-sectional drawing of CSIRO wheel motor (Copied from Lovatt, Ramsden & Mecrow 1997)

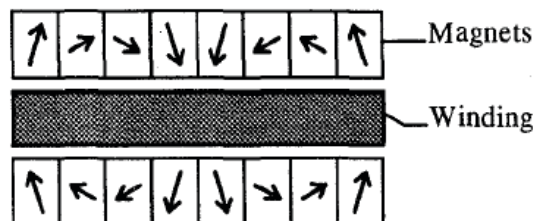


Figure 5.3: Halbach magnet array and air-gap winding (Copied from Lovatt, Ramsden & Mecrow 1997)

Based on this general topology, an optimised design was reached which featured a 40-pole design, and thanks to the Halbach array managed 0.91T peak air-gap flux density.

The motor has a continuous power rating of 1.8kW, or up to 5.6kW for 72 seconds (such as for acceleration or when climbing a short hill). Continuous torque is 16.2Nm with a peak of 50.2Nm. The motor has a total active mass of 6.4kg (4.8kg of which being magnets), with a total wheel weight of 14kg.

Copper loss is identified as the main source of inefficiency in the design, and heat buildup in the stator windings is the limiting factor in continuous power rating. One disadvantage identified with ironless stators is the low thermal mass, which means heat builds up quickly if the motor is used above its continuous rating.

Although the motor is extremely efficient, its power and torque density of around 0.3kW/kg and 2.5Nm/kg is not particularly impressive, and would be inadequate for either road-going cars or Formula SAE vehicles.

Another motor based on axial flux topology with ironless stator was presented by Pullen & Mansir (1999). It features a multistage design which puts several rotors and stators in series to achieve extremely high power densities up to 7.5kW/kg – although these are at very high speeds of around 60,000rpm, and the motor has surprisingly low torque density.

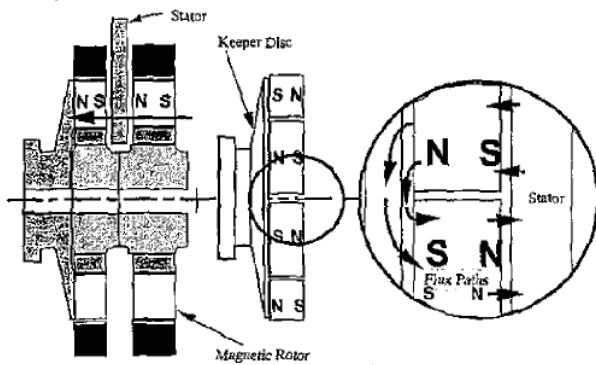


*Figure 5.4: Cross-section of motor topology
(Copied from Pullen & Mansir 1999)*

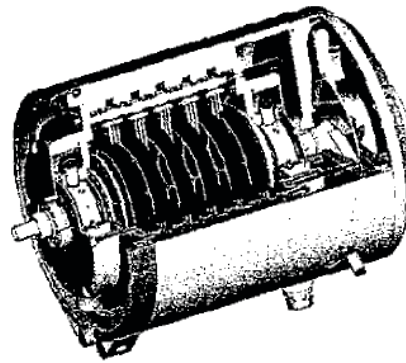


*Figure 5.5: Cutaway view of motor
(Copied from Pullen & Mansir 1999)*

Their largest prototype manages 100kW at 60Krpm in a Ø230mm x 310mm housing. This translates to just 16Nm torque, so the design would definitely need a reduction drive to the wheel, though the remarkable potential power densities do make it attractive.

The rotor diameter appears to be quite small in this design, but it raises the possibility of a larger diameter design like the CSIRO motor combined with a multistage design, in order to achieve sufficient torque while maintaining very high efficiency.

Another ironless AFPM wheel motor design was presented by Greaves et al (2003). The application was to drive the two rear wheels in a 600kg vehicle, direct drive. Peak torque of 500Nm (5-second rating) and 250Nm (3-minute rating) were required, and a maximum speed of 1500rpm.

An ironless design was chosen to allow high frequencies (without suffering excessive eddy current losses) as well as avoiding cogging torque.

Like the CSIRO motor, it featured dual Halbach Arrays either side of copper windings in the airgap. This design also used steel backplates on the magnet arrays in order to better contain the magnetic field.

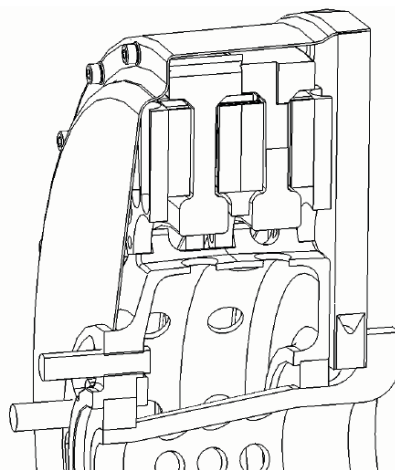


*Figure 5.6: Cross section of the UltraCommuter Rear Wheel Mounted Direct Drive Motor
(Copied from Greaves et al 2003)*

The final design had 24-poles with dual stators, a total mass of 24kg (with 9kg of magnets) and a diameter of 390mm. It achieved real-world operating efficiencies in the range of 94-97%.

A disadvantage cited with ironless designs is the difficulty in maintaining high airgap flux density. In this design, only 0.65T was achieved. However it demonstrates that high torque density possible with ironless (stator) motors.

A similar design was presented by Xiaoyuan et al (2005), having dual stators with air-gap windings, and three permanent magnet rotors. The two outer rotors used Halbach Arrays to maximise flux containment and airgap flux density, and the central rotor standard magnetic dipoles to help maintain flux across both stators.

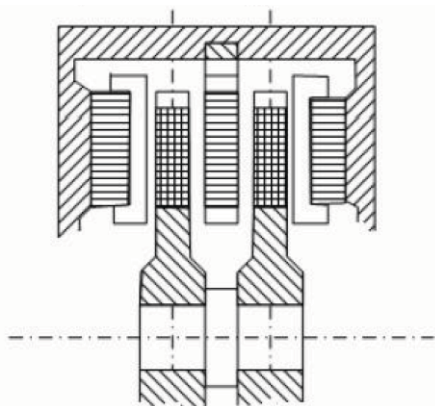


*Figure 5.7: Cross-section of motor design
(Copied from Xiaoyuan et al 2005)*



*Figure 5.8: 3D view of three-disc magnet layout
(Copied from Xiaoyuan et al 2005)*

Often in situations where high torque is required, it makes sense to use a ferromagnetic stator core in order to maximise magnetic flux density, despite the iron losses it introduces which result in slightly lower operating efficiency, and the additional weight which is generally unwelcome for hub motors.

Yang, Lui and Chueng (2004) were one team who believed having an iron core was a better option. They started with the concept of an axial flux PMSM topology with dual stators either side of a permanent magnet rotor, and developed a mathematical model to iteratively optimise the design, ending up with a 16-pole, 24-slot layout, as shown in Figure 5.9.

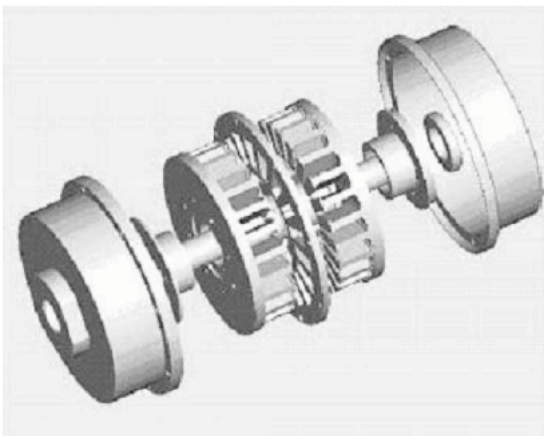


Figure 5.9: Exploded diagram of axial-flux wheel motor (Copied from Yang, Luh & Cheung 2004)

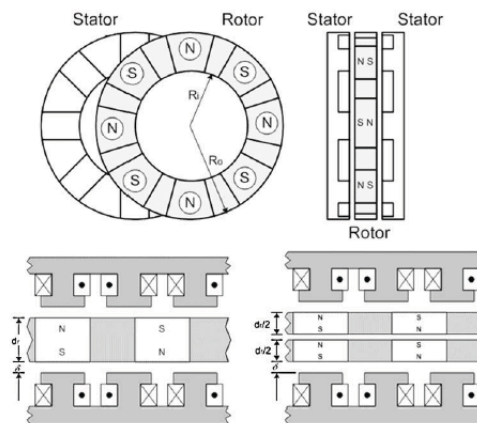


Figure 5.10: Dual axial-flux motor topology and its 2D configuration (Copied from Yang, Luh & Cheung 2004)

Rahman et al (2006) present another design based on an iron stator core. With an iron core, a major challenge for the direct drive system was keeping the size and weight of the motor low.

Axial flux was chosen due to high efficiency and specific torque - the latter being best achieved with large motor diameter and high magnetic pole count. Their design features dual 30-pole rotors either side of a torus inner-stator, and achieves up to 500Nm with 1200rpm maximum speed.

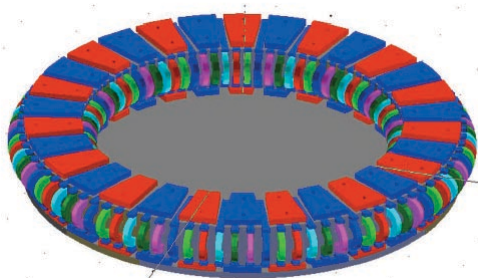


Figure 5.11: 3D render of AFPM wheel motor design (Copied from Rahman et al 2006)



Figure 5.12: Picture of test unit installed on mule vehicle (Copied from Rahman et al 2006)

Axial flux motors often have relatively low winding inductance which can make controller electronics more difficult (rate of change of current may exceed response rates of motor controllers). A workaround featured in their motor is additional permanent magnets in the stator to increase winding inductance – though perhaps superior motor controller electronics are a better option.

The problem of cogging torque associated with PMSM motors is ameliorated by “short pitching” the magnets, i.e magnets are at a slightly reduced pitch compared with the stator windings to remove any regular saliency interactions. They claim this does not affect output torque, however if the effect is similar to vernier drive motors then a small reduction in torque would be inevitable compared with perfectly stator/rotor alignment.

Another interesting feature of the design is the removal of rotor backplate material in areas where magnetic flux density is lower, in order to reduce motor weight (and hence unsprung weight).

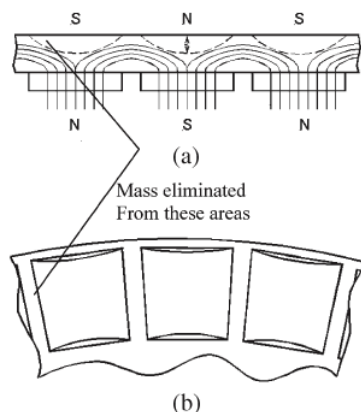


Figure 5.13: (a) Flux in the rotor back iron showing the area of low flux concentration. (b) Area of low flux concentration removed from the back iron to reduce mass. (Copied from Rahman et al 2006)

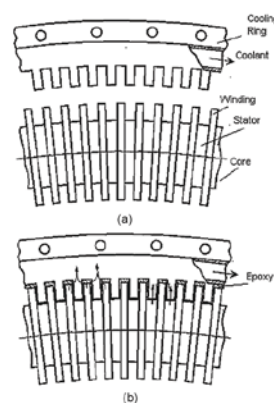


Figure 5.14: Winding cooling arrangement. (a) Stator and cooling ring separate. (b) Stator and cooling ring engaged. (Copied from Rahman et al 2006)

As previously mentioned, PMSMs have an advantage over other motor types in having low rotor heating. Only the stators typically require much cooling. In this design, an aluminium tube forms a water cooling ring around the stator and is bonded with thermally-conductive epoxy to remove heat from the stator coils and core.

Overall, this design appears to be one of the most well thought out and viable designs for in-wheel motor systems.

Kim et al (2009) review the attributes of the two most common types of axial flux PM considered for in-wheel motors, namely the surface winding PM (aka torus winding) and the interior winding PM. Figure 5.15 shows these two topologies.

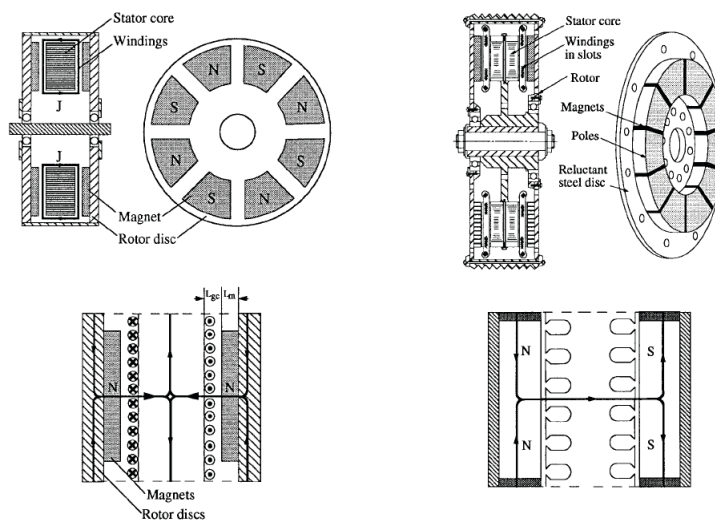


Figure 5.15: Comparison of axial flux motor topologies: Surface-PM (left) or interior PM (Copied from Profumo, Zhang & Tecomi 1997)

The surface (torus) winding design has stator windings wrapped around a toroidal iron core between two PM rotors. It has the advantages of a non-salient stator so has no cogging torque, and is easy to build. However they have a relatively large air gap which reduces flux density and/or requires larger magnets, and since windings are not held in place by stator laminations they can be stressed by electromagnetic forces.

The interior-winding design has a slotted iron stator with concentrated windings between two PM rotors. Due to the stator slotting this design can have significant cogging torque, however the mechanical strength of having embedded windings was considered important in a harsh environment, and the much smaller airgap allows for better flux (and hence torque) density. The

interior-winding design was considered the better option for in-wheel motors.

Their research also investigated the merits of 2-phase motors and controllers, with full bridges for each phase, which increases DC link voltage since each phase can have (\pm) the full DC voltage across them, but advantages over conventional 3-phase drive systems were not convincing.

Although not specifically intended for in-wheel motor use, a team at Oxford University led by Woolmer & McCulloch (2007) developed a very high torque axial-flux motor which appears to offer suitable performance. They refer to the design as Yokeless and Segmented Armature Topology (YASA).

Once again it is based on an axial flux design with dual rotors either side of an iron-cored stator. Basically the design appears to be an axial-flux version of the vernier drive / LRK concept, having 10-pole rotors with 12 stator windings.. As well as the torque advantage of the vernier drive design, they cite the lack of lap windings as offering significant advantages in terms of copper utilisation, overall machine size, and construction simplicity.

Figure 5.16 shows topologies of two of the common best performing axial flux PMSM designs, and the new YASA concept.



Figure 5.16: Comparison of axial flux motor topologies: inner-rotor (left), torus inner-stator (middle), and segmented armature torus (right) (Copied from Woolmer & McCulloch 2007)

The motor uses powdered iron cores instead of steel laminations, primarily because laminations are more difficult to produce for an axial flux machine since they have to go radially. Unfortunately powdered iron cores are known to have somewhat lower magnetic permeability than laminated steel cores, and based on their findings the cores show significant eddy current losses from about 250Hz, which works out around 2500rpm for this motor.

Another interesting feature of the design is the use of epoxy coated magnets, which removes electrical conduction paths between magnets and the rotor backplates, reducing eddy current losses in the rotors.

A 20% torque advantage is claimed over equivalent conventional AFPM designs, and an efficiency of over 95% is achieved at rated load.

The design has been successful enough that it is currently being commercialised through a newly-formed company YASA Motors.

The first production model offer very high power density of 9kW/kg. They have a maximum torque of 750Nm, and power of 60kW continuous / 100kW peak from on 25kg motor weight.



Figure 5.17: Image of YASA-750 motor
(From YASA Motors 2011)

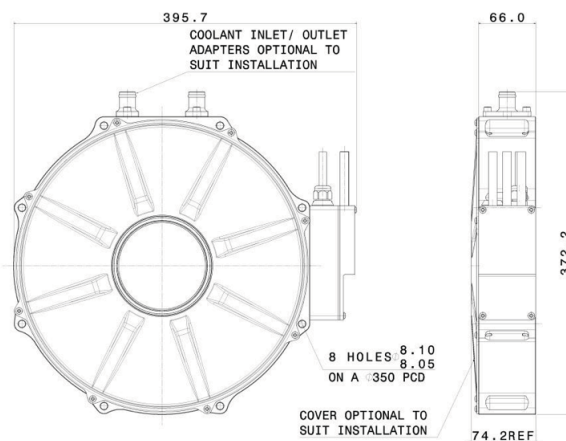


Figure 5.18: Dimensions of YASA-750 motor
(From YASA Motors 2011)

These figures are significantly higher than required per-wheel in either of the example applications being considered in this project, so a scaled-down version of such a motor may be a viable candidate for small road-going cars or Formula SAE vehicles in the future.

5.2.1 Outer-rotor Radial Flux Motors

The second motor topology to receive a lot of attention as a candidate for in-wheel motor systems is the outer-rotor radial flux PMSM. It seems an intuitive choice since the rotor can be integrated with the inside of the wheel rim itself.

Wu, Song & Cui (2007) cite several other advantages of the outer-rotor radial flux motors over axial flux motors including higher field intensity across stator, easier manufacturing of magnets,

and equalized magnetic forces between stator and rotor (though this is also the case for dual-rotor or dual-stator AFPM designs, which covers all candidates discussed here).

One of the most prevalent and successful applications of wheel hub motors in recent years is in electric bicycles and scooters. The direct drive hub motors used in these applications are almost ubiquitously outer-rotor PMSM. Brand, Ertugrul and Soong (2003) studied the performance of a PMSM outer-rotor direct drive example, shown in Figure 5.19.



Figure 5.19: Typical example of direct drive bicycle hub motor (Copied from Brand, Ertugrul & Soong 2003)

For safety reasons Australian law (and that of many other countries) prohibits wheel motors for electric bicycles exceeding 200W, and discourages them from going above 20km/h. So unfortunately all bicycle wheel hub motors are at least an order of magnitude lower powered than required for a Formula SAE application.

Hub motors for electric scooters are typically up to around 3kW (for small scooters equivalent to 50cc engines), but unfortunately these are still much too small for Formula SAE use. However, that does not mean that the technology cannot be scaled up to suit larger vehicles.

An early example of an outer-rotor PMSM for in-wheel motor use was published by Terashima et al (1997), developed for a vehicle using four in-wheel motors. Each motor weighed 33kg with a continuous power rating of 6.8kW. A maximum torque of 420Nm is claimed, with 25kW peak power.

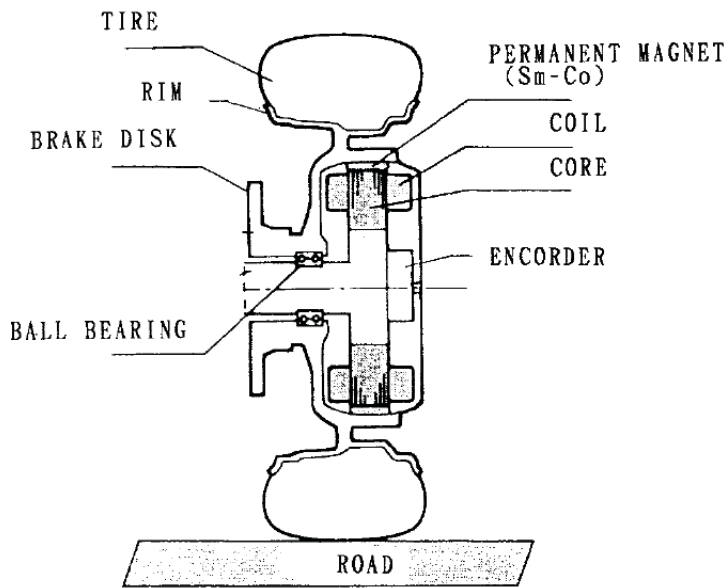


Figure 5.20: Cross section of in-wheel motor (Copied from Terashima et al 1997)

Part of their research with the project was determining ways to reduce cogging torque with this type of motor, to improve passenger comfort.

Another example of an outer-rotor PMSM is presented by Chung (2008). It is 350mm diameter and only 50mm in length, so has similar aspect ratio to many axial flux designs.

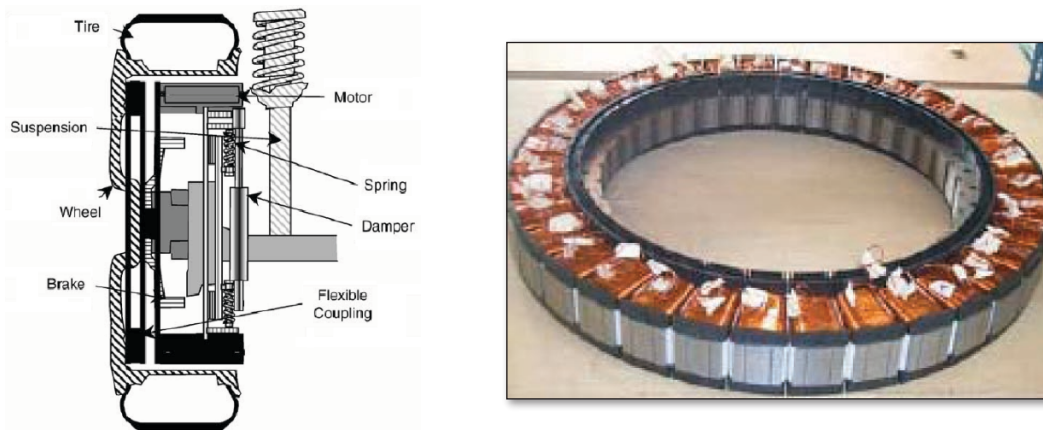


Figure 5.21: Configuration of the in-wheel motor system (Copied from Chung 2008)

Figure 5.22: Assembled stator and rotor of the in-wheel motor (C Copied from hung 2008)

The design achieves a respectable 5.7kW of power, however this occurs at 4000rpm and just 15Nm torque, so a design with higher torque (perhaps at the expense of speed) would be required if it were to be used as a direct-drive wheel motor.

Prior to their 2003 paper featuring an axial flux in-wheel motor design, Greaves, Walker and Walsh (2001) published a design of a radial-flux PMSM. The design was somewhat unique in its use of an ironless stator for a radial flux motor, and used a passive iron ring inside the stator as a return path for the magnetic flux.

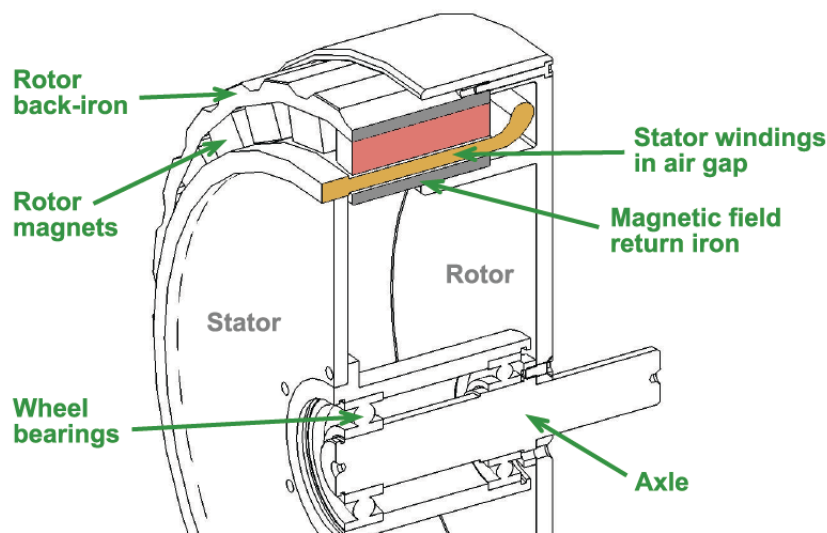


Figure 5.23: 3D Cross-section of PM ironless machine (Modified copy from Greaves, Walker & Walsh 2001)

This design was intended for epicyclic (planetary) reduction drive to the wheel, rather than direct drive like their 2003 axial flux design. A 24-pole design was chosen, with an 8mm air-gap width and 38-gauge Litz wire used for the stator windings, resulting in a 38% copper fill factor.

A peak air-gap flux density of 0.56T was achieved, which is significantly lower than many other designs, certainly those with an iron core but even many other ironless designs such as the CSIRO motor, suggesting the magnetic flux in the motor was hindered by a relatively high reluctance (the field from the magnets effectively having to cross the airgap twice from a north to south pole).

It yielded a peak speed of 7000rpm, with 30Nm continuous and 60Nm peak torque. Dimensionally the motor was approx Ø300mm x 150mm and weighed 10kg (with 2.1kg magnets). One of the downsides of the outer-rotor PMSM topology is clearly shown in the diagram above, where a large volume of the motor is inactive. The saving grace for this type of motor is that some designs allow this space to be used for items such as disc brakes and suspension mounts.

5.3 MORE EXOTIC MOTOR TOPOLOGIES

Not all researchers have assumed 3-phase PMSM motors are the best option for wheel hub motors. Here, several other ideas are presented.

5.3.1 Transverse Flux Permanent Magnet (TFPM) machines

TFPM machines are basically a variant of PMSM, using north-south magnetic pairs axially adjacent, such that flux paths are perpendicular to rotation.

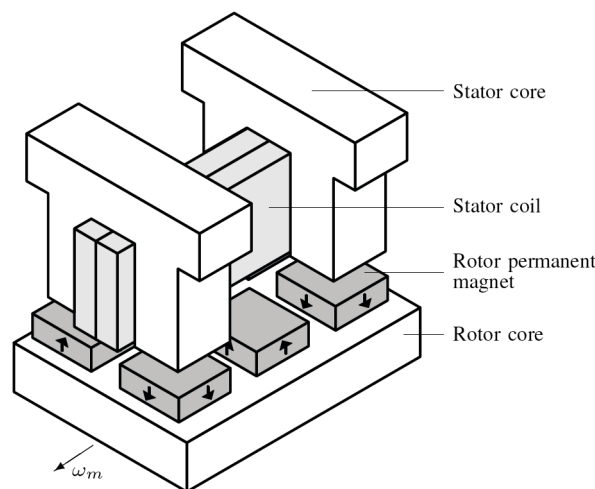


Figure 5.24: Transverse flux PM topology, where w_m is the direction of movement (Copied from Svehkarenko et al 2008)

The primary advantage cited is high torque density due to the possibility of very high pole count, which makes them potentially attractive for in-wheel motor systems. Their primary disadvantage is poor power factor and high magnetic leakage – often leading to lower power density and operating efficiencies.

A paper by Espanet, Kauffmann and Barnard (2006) compares two in-wheel PM motors for military applications, one being a conventional outer-rotor axial-flux PMSM motor, and the other a transverse flux hybrid reluctance motor.

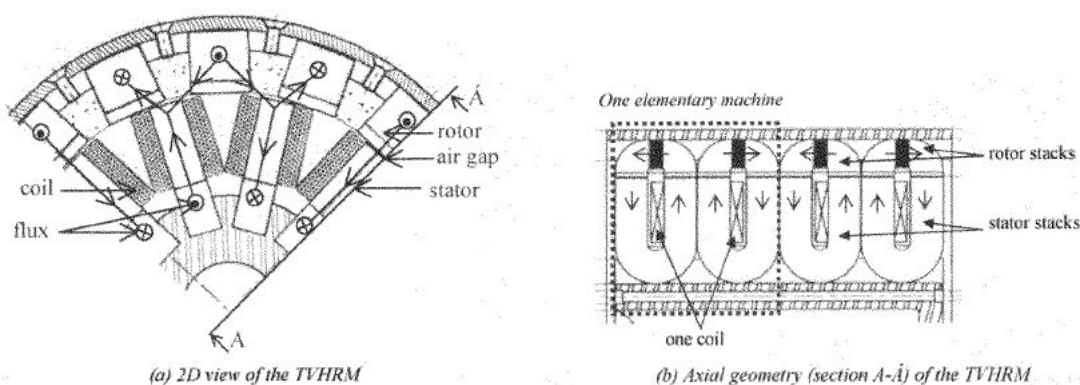


Figure 5.25: Geometry of the TVHR motor (Copied from Espanet, Kauffmann & Bernard 2006)

For this application a fairly large space of $\text{Ø}480\text{mm} \times 200\text{mm}$ is available within the wheel hubs, and 30kW of power is required per wheel. The two motors were designed with identical overall size of $\text{Ø}240\text{mm} \times 180\text{mm}$ in order to provide a fair comparison of performance.

Motor weight is listed as 92kg for both with 20kg of permanent magnet - though it may be suspected that it is a mistake in the paper because the magnet weight in the TVHR is explicitly stated as being less in their conclusion (and indeed TVHR's primary advantage).

They concluded that although the TVHR topology had some advantages, the PMSM's greater efficiency and much higher torque (twice that of the TVHR) made it a better choice for an in-wheel motor. The main disadvantage mentioned for the PMSM was the expense of having a larger quantity of permanent magnets in the design.

5.3.2 Variable Reluctance Motors (VRM)

Some researchers have explored the use of Variable Reluctance Motors for in-wheel motor use. In his Masters thesis, Cakir (2004) describes the design of an experimental outer-rotor VRM direct drive hub motor. VRM was chosen for exploration because of its mechanical simplicity, as well as fault tolerance (since it can lose one phase and keep working).

The high torque ripple seen in VRM designs was cited as one of the main disadvantages for their use in traction systems, though it was proposed that large inertia of vehicle would render the problem insignificant.

Wang et al (2005) describe a 50kW VRM developed for a hybrid bus application. The motor is an 8 stator pole, 6 rotor pole design requiring four-phase control. The prototype motor achieved

1 kW/kg power density and 2.21 Nm/kg torque density, which is respectable but well below the best PMSM motors.

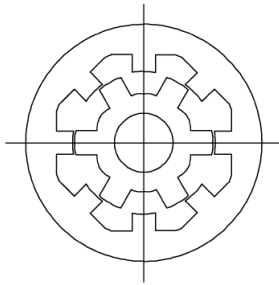


Figure 5.26: Cross section of the four-phase 8/6 VRM (Copied from Wang et al 2005)

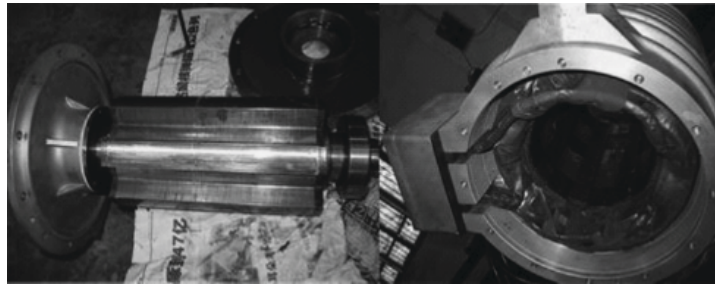


Figure 5.27: Rotor and stator of the prototype VRM (Copied from Wang et al 2005)

Also an efficiency of 88% was observed at the rated power, which is significantly lower than AC induction or PMSM motors, and explains why they found the need for additional cooling systems for sustained operation. A typical AC induction or PMSM motor would only require half as much cooling for equivalent sustained power output.

Finally, significant acoustic noise was observed which may be unwelcome in passenger vehicles. Overall it was concluded that more work would be needed before VRMs are a commercially viable option for traction applications.

5.3.3 Spherical Wheel Motors

Spherical motors are an interesting topology in that the rotor has three degrees of freedom with respect to the stator.

Kang et al (2008) investigate a spherical wheel motor with four magnetic poles and two rows of six stator windings. If the two sets of stator coils are excited equally in a normal 3-phase fashion, the rotor aligns and rotates between them. The stator coils can also be excited unevenly (off-axis) in order to turn the rotor off-axis, up to ± 18 degrees. In this way, it is possible for spherical motors to actuate both drive and steering in vehicles.

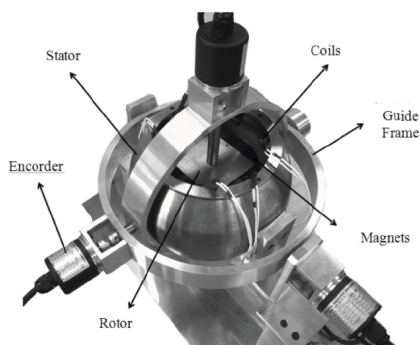


Figure 5.28: Photo of PM spherical wheel motor (Copied from Kang et al 2009)

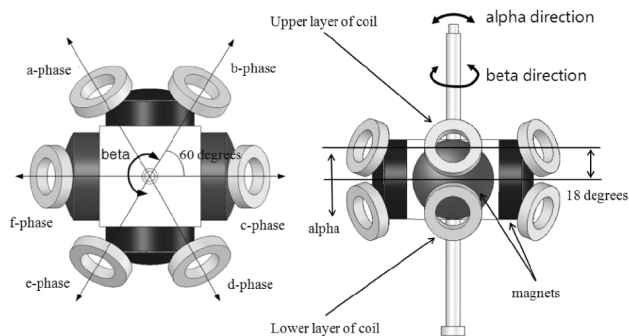


Figure 5.29: Structure and operation of PM spherical wheel motor (Copied from Kang et al 2009)

It is an interesting idea which may be useful in some applications, however it is difficult to construct, difficult to control (requires two 3-phase bridges instead of one), and does not yield particularly high power densities due to low copper utilisation (windings necessarily span an area larger than the rotor).

In road-going vehicles such designs may also have problems with compliance of what is effectively magnetically-coupled steering. For example if the wheel hits a bump, the steering angle could change and induce instability.

Lee, Son & Joni (2005) present a spherical wheel motor based on a variable reluctance design instead of a permanent magnet rotor. It would seem that such a design is exposed to all of the same disadvantages, plus those inherent to variable reluctance motors.

5.3.4 Reducing Permanent Magnet Volume

Often the single most expensive part of a PMSM motor is the rare earth permanent magnets. In most designs large enough to drive a car, there is a significant volume of magnet. Laskaris & Kladas (2008) explore an inner-rotor PMSM design which uses thin magnets embedded in a laminated rotor with tangentially-aligned fields.

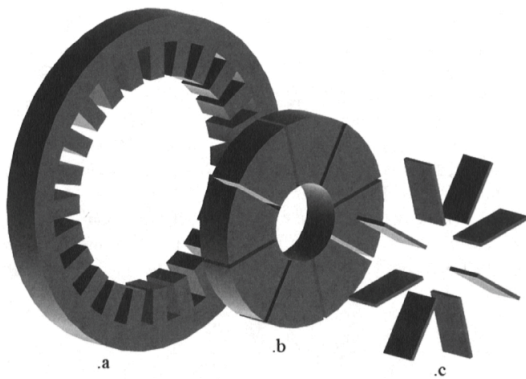


Figure 5.30: IPM Wheel Motor magnetic components geometry (Copied from Laskaris & Kladas 2008)
 (a) Stator - 0.5mm laminated silicon steel
 (b) Rotor - Solid iron magnetic core blocks
 (c) Rotor - NdFeB permanent magnet blocks

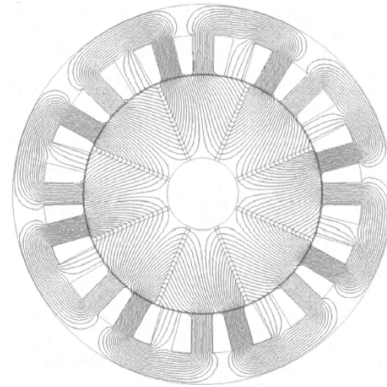


Figure 5.31: Magnetic flux density distribution in the motor under full load (Copied from Laskaris & Kladas 2008)

The primary advantage cited is high utilisation of magnets, with a small volume of magnetic material yielding a high airgap flux. A notable disadvantage of the design is the large amount of steel required for flux conduction in the rotor, which increases weight. So the design basically equates to a cost saving in PMs at the expense of power density.

In a later paper by Laskaris & Kladas (2010), use of this motor is discussed for in-wheel drive in the two rear wheels of an experimental vehicle, and performance results are presented from a prototype constructed. An efficiency of 95% is observed – typical of a good PMSM motor. Maximum torque of 41Nm and a continuous power of 12.1kW for a 12kg motor is observed (approx 1kW/kg), indicating that (as predicted) this design does not offer sufficient torque or power densities for hub motor applications.

5.3.5 Polyphase Motors and Controllers

The vast majority of AC induction and PMSM motors are designed to run off 3-phase power, with each phase 120° apart. Generally, 3-phase is considered the optimum trade-off between motor/controller complexity, and smoothness of operation.

We have already reviewed one example of different case, being the 2-phase full bridge motor/controller evaluated by Kim et al (2008). Tseng & Chen (1997) present a novel 5-phase PMSM outrunner, based on 20 slots and 22 poles – i.e a 5-phase equivalent of the vernier drive LRK design, with a salient laminated iron stator and concentrated windings.

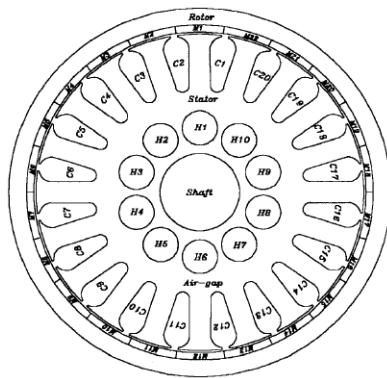


Figure 5.32: Radial cross-section of proposed wheel motor (Copied from Tseng & Chen 2005)

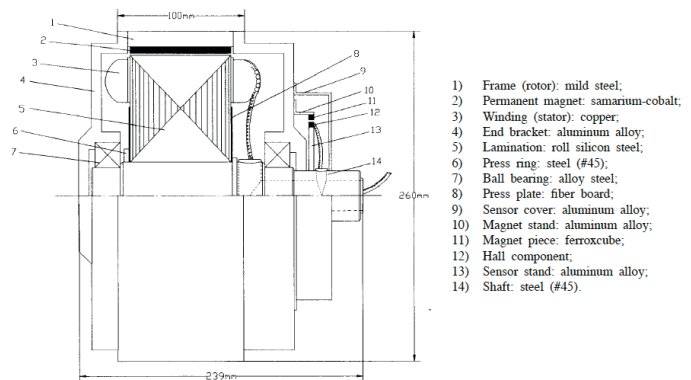


Figure 5.33: Axial cross-section of proposed wheel motor (Copied from Tseng & Chen 2005)

Their paper does not discuss many performance advantages of the 5-phase system, other than significantly reduced cogging torque, which is claimed to be about 20x lower with this type of fractional slot-width to pole-width vernier design, compared with a conventional 3-phase PMSM of equivalent pole count. However this is primarily a result of being a vernier drive design rather than specifically 5-phase.

In theory a 5-phase controller would not be much more difficult or expensive to make than a typical 3-phase controller. More phases means less power per phase, so overall the same power ratings / power device ratings, and a microcontroller would need to output five phase signals instead of three to the power stage.

5.4 PREVIOUS HUB MOTOR DESIGNS FOR FSAE VEHICLES

Ivanescu (2009) investigated conversion of an existing Formula SAE Electric (FSE) vehicle to in-wheel motor drive, with significant budget constraints. Due to a lack of commercial motors suitable for direct drive, a reduction drive was decided upon. Many options were considered including chain drive, spur gears and planetary gearboxes, but ultimately a belt drive solution was chosen due to the low cost and accessibility of parts, and tolerance of some misalignment/vibration.

The desired 5:1 reduction ratio was not feasible with a single pulley pair due to space and power constraints, so a two stage reduction design was developed as shown in Figure 5.34:

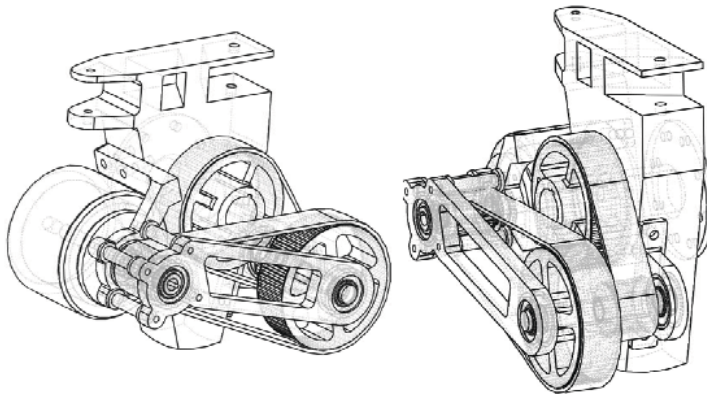


Figure 5.34: Two views of the in-wheel two-stage pulley system (Copied from Ivanescu 2009)

A qualitative criticism of the design is the complexity (large number of moving parts) and considerable volume occupied. Also many decisions were dictated by the avoidance of major modifications to the existing upright, which may have compromised design elegance.

Harris (2000) investigated adding front wheel drive to a FSE vehicle using in-wheel motor drive. Requirements for a front wheel drive system are less demanding since load transfer reduces the traction of front wheels under acceleration. Design criteria were for low weight, simplicity, performance, budget and availability. This led to the selection of a commercial high-speed motor mated to a epicyclic (planetary) reduction gearbox.

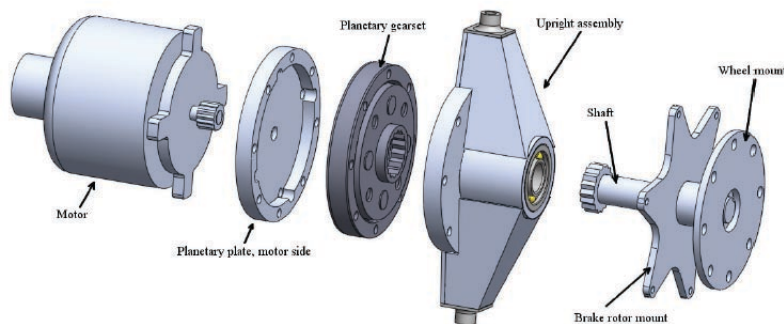


Figure 5.35: Exploded view of in-wheel drive system (Copied from Harris 2010)

The design appeared to be significantly more compact than the dual belt drive from Ivanescu (2009). One issue not addressed was the limit of 4000rpm for the gearbox, which is only half the motor's maximum 8000rpm. Matex suggested the RPM limit was primarily a result of heating, and that it may be possible to run at higher speeds with sufficient circulating oil lubrication – but this would need further investigation.

5.5 COMMERCIAL PRODUCTS AND PROTOTYPES

5.5.1 Introduction

Hub motors are commonly used in some applications such as electric bicycles and solar cars, but are yet to be seen much use in road-going automobiles. Many commercial prototypes have been developed, though being outside academia little technical information is available for them, and none have been adopted in any mass-manufactured vehicles as yet. In this section several examples are reviewed.

5.5.2 Protean Electric (formerly PML Flightlink)



Figure 5.36: Cutaway view of Protean Electric's electric wheel motor (Copied from Brooke 2010)

One of the most well known companies developing wheel motors for road-going vehicles is Protean Electric (formerly PML Flightlink). The company built its first wheel motor in 2003 and has demonstrated prototypes in various concept vehicles.

Their current model, the PD18, is a high pole-count (72-slot, 48-pole) outer-rotor PMSM motor. The design uniquely includes motor controller electronics in the wheel hub itself, actually having 8 sub-controllers per wheel. Stator and power electronics are water cooled.

Motor size is 420mm diameter by 115mm length, with a motor mass of 31kg. Some impressive statistics are cited, such as 64kW continuous @ 400VDC per wheel, with a continuous torque of 500Nm and a peak of 800Nm. Of course, these figures are not independently substantiated.

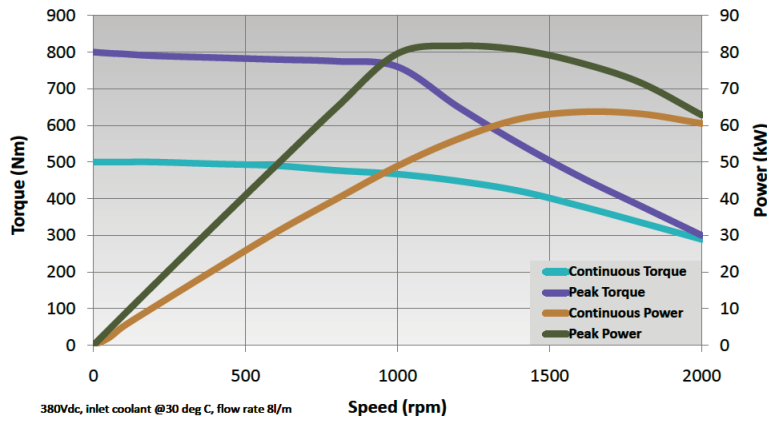


Figure 5.37: Performance graph of Protean Electric PD18 In-Wheel Motor System (Protean Electric 2011)

Although prototypes have been demonstrated in vehicles, they have not been adopted in any mass-produced vehicles. Around 2008 these wheel motors were listed as available for purchase, though with a hefty price tag around US\$25 per wheel – a prohibitive figure for many road-going vehicles or SAE projects.

5.5.3 Michelin Active Wheel

A prototype of the Michelin Active Wheel was first demonstrated in October 2008 at the Paris Motor Show. The drive system is based on a small water-cooled 30kW permanent magnet motor with gear reduction to the wheel. Braking is achieved with an inverted disc (outer-rotor with caliper inside). An interesting feature of this design is that it also packages suspension within the wheel hub, based on a coil spring for static loading plus an electric motor for active damping. The whole assembly has a weight of 42kg.

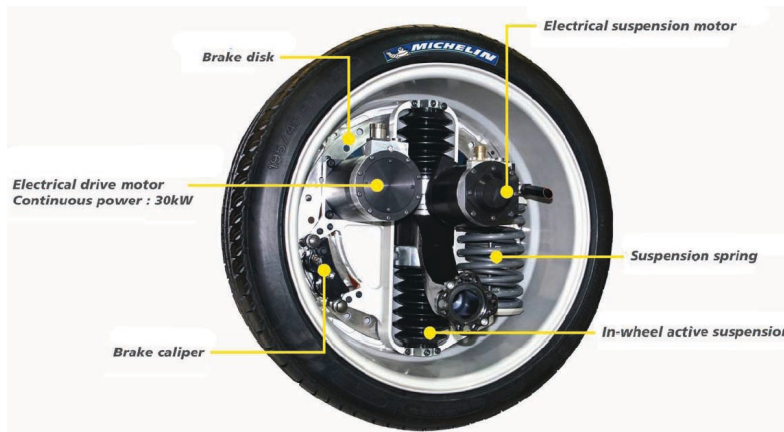


Figure 5.38: Components of Michelin Active Wheel (Copied from Michelin 2008)

Michelin press kit reiterates the advantages of such hub motors in freeing up space in the vehicle body by moving drive components (and here suspension as well) into the wheel hubs. As yet the design remains a concept only and has not been adopted in any production vehicles – perhaps for undisclosed technical limitations.

5.5.4 Siemens VDO eCorner

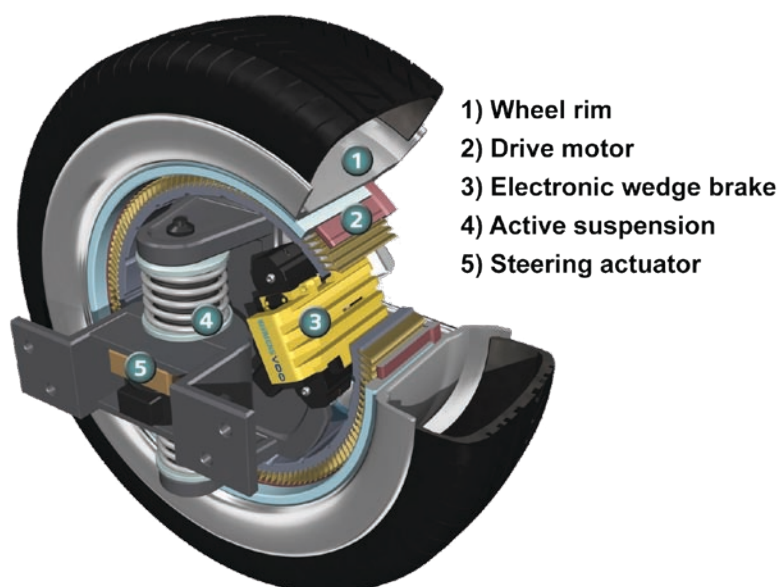


Figure 5.39: Cutaway view of Siemens eCorner wheel motor solution (Copied from Autospectator 2006)

The Siemens eCorner is similar to the Michelin Active Wheel insofar as it too incorporates drive, braking and suspension into a wheel hub design, however there are several significant differences.

Firstly the drive motor is direct drive to the wheel, based on a large diameter, high pole-count outer-rotor PMSM motor (a ring motor). Based on research so far, this appears to be a viable way to get enough drive torque, though it may be fairly challenging to build.

The other notable difference is the use of an electronic wedge brake, which is a new type of brake caliper based on an electric linear actuator (with mechanical advantage) rather than a hydraulic system.

A design goal was to keep unsprung weight below 20% of total vehicle weight, to avoid degraded suspension behaviour. Siemens claim 150Nm per wheel for convection cooled (or 250Nm per wheel if water cooled) which would certainly satisfy the requirements identified in section 3.2 for

a small road-going car. An operating efficiency of 96% is cited, which Siemens point out is much higher than conventional drive systems (Sawyer 2006).

As with the Michelin Active Wheel, for reasons unknown the concept is yet to be adopted in any production vehicles.

5.5.5 E-traction

US company e-traction have presented designs for in-wheel motor systems, imaginatively called TheWheel, targeting large vehicles such as busses and trucks. They claim an efficiency more than 90% (not particularly impressive for an electric motor) with torque up to 15kN for their largest design which, extrapolating from the requirements analysis in section 2.2, would certainly be enough to power a large vehicle such as a bus or truck.

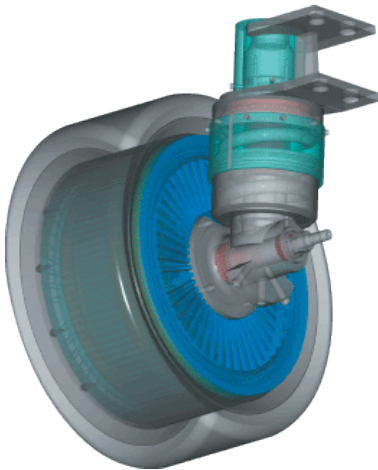


Figure 5.40: 3D render of TheWheel system (Copied from e-Traction 2011)

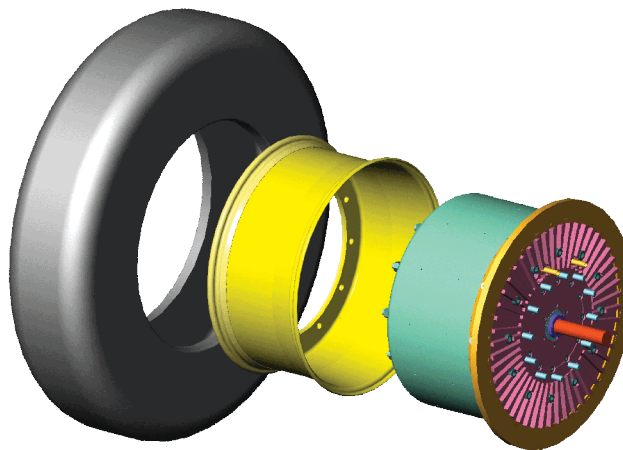


Figure 5.41: Exploded view of TheWheel system (Copied from e-Traction 2011)

Not much technical information is available but based on available images, it appears to be a high pole-count outrunner PMSM design. Power densities in the order of 3kg per kW are claimed, which is probably too heavy for a road-going vehicle or SAE vehicle, but may be acceptable for lower-performance vehicles such as their target market of busses and trucks.

Once again, there is a notable lack of real-world usage of this design, suggesting it may still be in development phase and/or has hit insurmountable technical problems.

5.6 HIGH PERFORMANCE MOTORS

Since no commercial motors suitable for direct drive in a wheel motor of a Formula SAE vehicle were identified, the next option was to consider using a high performance, high speed motor plus reduction drive to the wheel – similar in principle to the Michelin Active Wheel and the designs from Ivanescu (2009) and Harris (2010).

Many motors were considered, but in line with other academic research the PMSM topology was found to be the clear leader in terms of power and torque density.

However there are still not many good commercial options available. A typical example of a PMSM motor used in small electric vehicles (such as motorbikes or service vehicles) is the Motenergy ME0201, an axial flux, single air-gap 8-pole PMSM. This motor weighs approximately 10kg and offers a continuous power rating of 5kW (15kW peak), representing a power density of 0.5kW/kg.



Figure 5.42: Motenergy ME0201 PMSM motor

The power rating is about right for Formula SAE applications, and indeed two of these motors were used for a more conventional drive system in a Formula SAE Electric prototype built at UWA in 2008/9, but the physical size and weight of the motor would make fitting within a wheel hub difficult.

This appeared to be a common story with motors intended for conventional drivetrains in traction applications, where power density is generally not such a high priority.

However one industry where power density is equally critical is electric aircraft. In recent years there have been motors released for small electric aircraft claiming up to 15kW power ratings

which would be sufficient for Formula SAE use, and with 3-5x higher power density than typical traction motors such as the Mars ME0201. They are invariably outer-rotor PMSM type motors, usually based on LRK (vernier drive) topology.

One caveat is that spinning a propeller requires virtually no starting torque so these motors tend to be designed for sensorless control, but this is not insurmountable as Hall sensors can be added to sensorless motors (Endless Sphere 2009) to make them more suitable for traction applications.

Table 5.1 summarises some potential candidates identified.

Table 5.1: Summary of four high performance PMSM motors for electric aircraft

Hacker A200	Plettenberg Predator 37
	
<p>Specifications:</p> <ul style="list-style-type: none"> • Voltage: 48V • KV: 151 rpm/V • Maximum power: 9.2kW* • Weight: 2.6kg • Dimensions: Ø110x126mm • Power density: 3.5kW/kg <p>(Source: Hacker 2007)</p>	<p>Specifications:</p> <ul style="list-style-type: none"> • Voltage: 48V • KV: 150 rpm/V • Continuous power: ~7kW* • Weight: 1.9kg • Dimensions: Ø100x90mm • Power density: 3.7kW/kg <p>(Source: Plettenberg 2010)</p>
Turnigy CA120-70	Astroflight 8150-5T
	
<p>Specifications:</p> <ul style="list-style-type: none"> • Voltage: 48V • KV: 150 rpm/V • Maximum power: ~7kW* • Weight: 2.6kg • Dimensions: Ø118x120mm • Power density: 2.7kW/kg <p>(Source: Turnigy 2011)</p>	<p>Specifications:</p> <ul style="list-style-type: none"> • Voltage: 55V • KV: 197 rpm/V • Continuous power: ~4kW* • Weight: 1.4kg • Dimensions: Ø80x70mm • Power density: 2.8kW/kg <p>(Source: Astroflight 2009)</p>

* Power ratings would assume sufficient convection cooling

5.7 UNSPRUNG WEIGHT CONSIDERATIONS

A commonly-cited concern with in-wheel motors is the consequence of additional unsprung weight, in its effect on suspension performance.

“Unsprung” simply refers to any part of a vehicle between the road and the suspension. The concern stems from the potential for “wheel hop”, where the inertia of the unsprung mass causes the response of the wheel to lag behind the surface changes of the road, causing it to lose contact and hence lose traction.

Figure 5.43 shows a “quarter suspension” model for a typical vehicle, i.e the dynamics of one wheel.

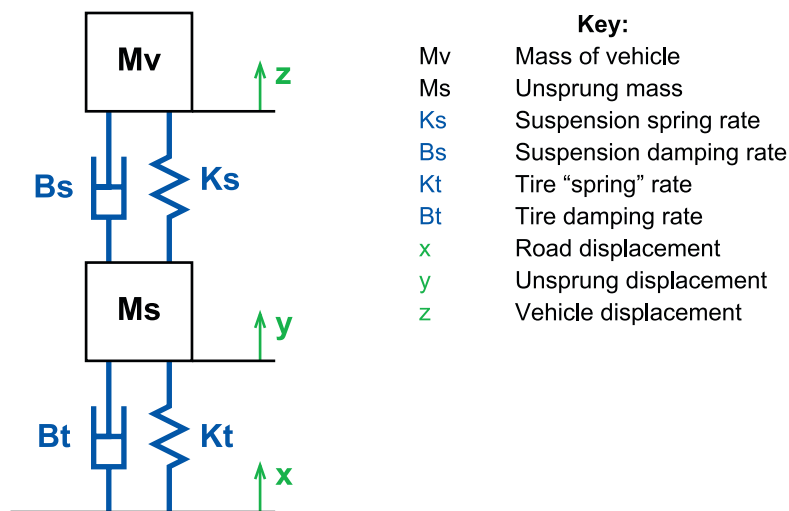


Figure 5.43: Quarter vehicle suspension model (as per Schalkwyk & Kamper 2006)

The problem was studied by Schalkwyk & Kamper (2006), who considered a typical road-going vehicle of mass 1500kg. Two cases were evaluated mathematically, either a 40kg unsprung mass per wheel typical of conventional drivetrains, or 100kg unsprung mass representing an additional 60kg allowance for in-wheel drive systems. Based on previous research, 60kg seems a fairly generous/conservative/worst case allowance. For their dynamic modelling, suspension and tire parameters kept the same (namely $K_s = 36\text{KN/m}$, $B_s = 3\text{KNs/m}$, $K_t = 110\text{KN/m}$, $B_t = 200\text{Ns/m}$). A simulation was created in Matlab/Simulink to analyse the suspension response. Figure 5.44 shows the Bode plot from the model, showing that the frequency response is in fact fairly similar for both cases. The first order natural frequency of the suspension changes by under 10%.

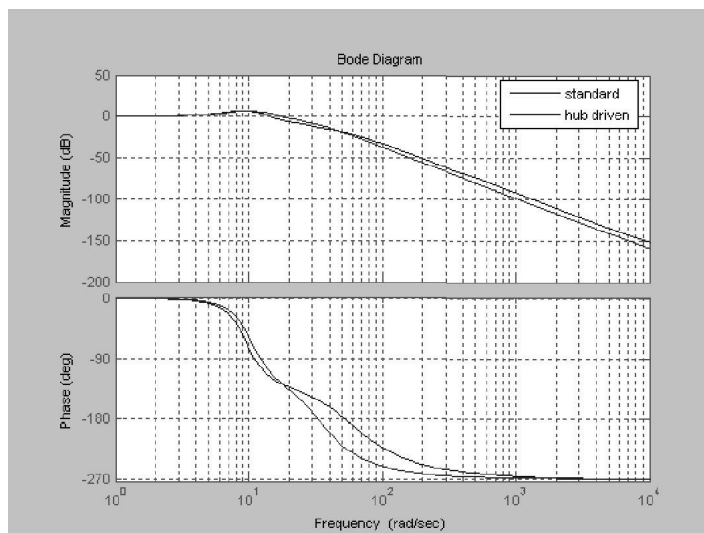


Figure 5.44: Bode plot of suspension frequency response (Copied from Schalkwyk & Camper 2006)

They also used the model to simulate a step response, which is a common test for vehicle suspension where there is a sudden drop of approx 8cm. Again a very similar response observed, as shown in Figure 5.45. A slightly larger peak force was observed for the case with higher unsprung mass, indicating higher impulse on tires which may need consideration for vehicles with very low-profile tires, but had minimal effect on the sprung mass and hence vehicle comfort.

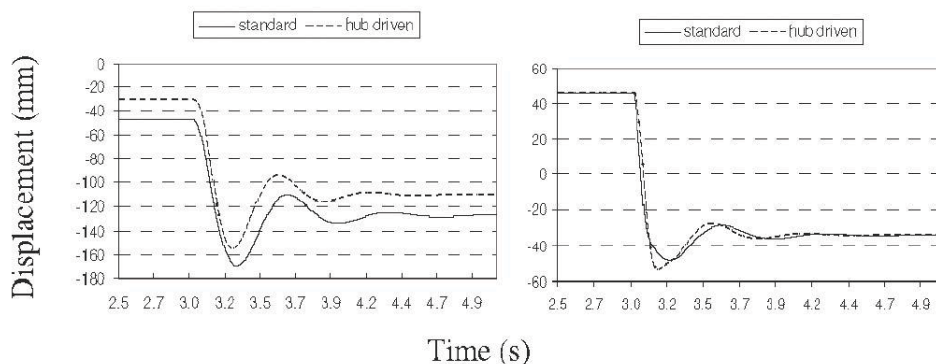


Figure 5.45: Sprung and unsprung mass step response (Copied from Schalkwyk & Kamper 2006)

Their conclusion was that behaviour of the two suspension systems does not differ significantly, so performance and comfort of the vehicle should not be significantly worse.

A novel idea for circumventing the issue of higher unsprung weight was proposed by Li-qiang, Chuan-xue & Qing-nian (2010) involving separately-suspended motors. A free-body diagram of this is shown in figure 5.45.

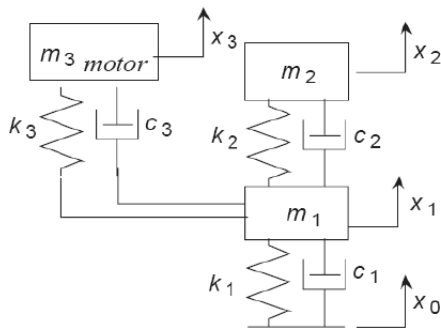


Figure 5.46: Dynamic model for separately-suspended wheel motor (Copied from Li-qiang, Chuan-xue & Qing-nian 2010)

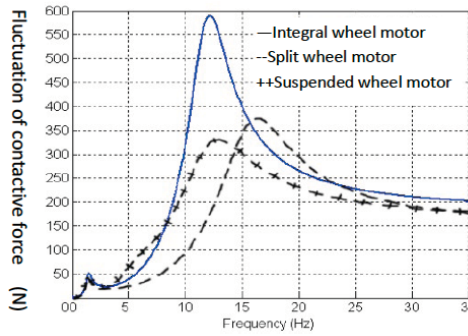


Figure 5.47: Frequency response for separately-suspended wheel motor vs conventional wheel motor and inboard drivetrain (Copied from Li-qiang, Chuan-xue & Qing-nian 2010)

Figure 5.47 shows the frequency response for three simulated systems: A conventional drivetrain, a typical in-wheel system with higher unsprung, and an in-wheel system with separately-sprung motor. The simulation showed a significantly higher peak in contact force fluctuation at the natural frequency of the system with larger unsprung mass vs conventional hub design, though similar performance at other frequencies. A significant improvement in contact force fluctuations is observed for the separately-suspended motor case.

Unfortunately the paper does not describe how a separately-sprung motor system could be implemented in practice, and it seems like it could be complicated (and make motor fitment even more challenging).

Another novel solution proposed to the unsprung weight problem was proposed by Hredzak, Gair & Eastham (1996), who suggested that since an axial-flux motor can tolerate radial misalignment, the stator could be sprung while the rotor unsprung. Figure 5.48 shows this effect graphically.

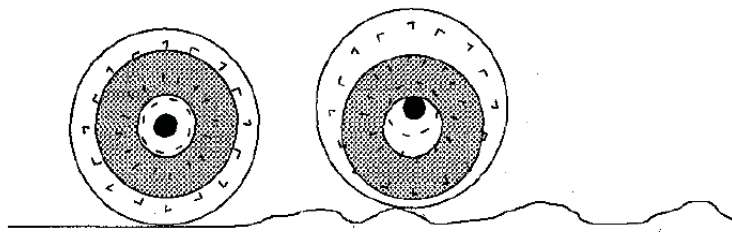


Figure 5.48: Illustration of rotor perturbation by the road surface (Copied from Hredzak, Gair & Eastham 1996)

The main limitations with this solution would be a fairly low limit of travel for the suspension, as well as compromised motor performance whenever the rotor and stator were misaligned. Also it

may make motor control algorithms difficult since the motor characteristics change depending on rotor displacement. Basically, the sacrifices do not seem justifiable for the gains.

A final thought on the unsprung issue which seemed to have gone unexplored in other academic research (but nevertheless seems appropriate to be discussed at this point) is the possibility of reducing brake size and weight due to the potential for electric motors to partially supplant them with regenerative braking.

Based on vehicles surveyed, a typical small road-going car has about 20kg in total unsprung mass of braking equipment, half of which is the steel brake rotors. For single-stop events, the brake rotors serve as the primary energy absorbing component (Walker 2005). In practice, aerodynamic drag, rolling resistance, mechanical losses etc are all absorbing some energy as well during a braking event, but contributions are relatively low.

A 1 tonne vehicle travelling at 100km/h has approximately 385kJ of kinetic energy. Decelerating at the traction limit of 1G (for typical road tires) requires the brake discs to absorb approximately 135kW of heat. Hence in theory, if wheel motors were able to provide a combined regenerative braking power of 135kW, they could completely replace mechanical brakes, which would reduce unsprung weight as well as free up space within the hub for the motor.

In Formula SAE, it is a requirement for vehicles to have mechanical brakes on all four wheels powerful enough to lock up all wheels and stop the vehicle safely from maximum speed, so supplanting mechanical brakes entirely is not possible. However the thermal mass of the discs could be reduced significantly if much of the sustained braking energy is absorbed through regenerative braking.

5.8 DISCUSSION

In this chapter, the state of the art of in-wheel drive systems has been reviewed. Firstly some academic research on the subject including prior research at the University of Western Australia, then some commercial hub motor designs, and finally some high performance motors possibly suitable for use in hub motor designs. The potential issue of increased unsprung weight has also been explored.

A consistent theme among research and designs is favouring PMSM as the most suitable motor type for in-wheel drive systems, since they can offer the highest power density (both gravimetric and volumetric) and highest efficiency – which is good for both performance and lower cooling requirements. A wide range hub motor designs based on PMSM motors have been reviewed in this chapter (Caricchi et al 1996, Lovatt, Ramsden & Mecrow 1997, Terashima et al 1997, Pullen & Mansir 1999, Greaves, Walker & Walsh 2001, Brand, Ertugrul & Soong 2003, Greaves et al 2003, Oh & Emadi 2004, Yang, Luh & Cheung 2004, Cheng, Duan & Cui 2005, Xiaoyuan et al 2005, Espanet, Kauffmann & Barnard 2006, Halkosaari 2006, Rahman et al 2006, Rajagopal & Sathaiah 2006, Woolmer & McCulloch 2007, Wu, Song & Cui 2007, Chung 2008, Güemes et al 2008, Melfi, Evon & McElveen 2008, Kim et al 2009, Jian, Xuhio & Lili 2009, Laskaris & Kladas 2010).

A frequently-cited drawback with in-wheel drive systems is the increase in unsprung mass. Schalkwyk and Camper (2006) confirmed that its effects would not be prohibitive, allowing for typical additional mass. However keeping unsprung mass low is certainly a design consideration.

Broadly speaking, hub motor designs may be divided into direct drive – where the motor drives the wheel directly at 1:1 ratio, or those integrating a reduction gearbox in the hub. Direct drive is generally considered the more elegant solution since it has fewer moving (wearing) parts, however it comes with its own technical challenges.

One of the biggest challenges for direct drive solutions is achieving sufficient torque. Large diameter and high pole-counts appear to be the best way to design a high torque motor. Iron losses can be significant for motors with very high pole count designs due to the electrical frequencies involved, though a saving grace for direct drive hub motors is that they only need to run up to 1000rpm, so can be built with a much higher pole count than normal high-speed motors.

Motors suitable for direct drive are necessarily heavier since they need far higher torque, and hence require more conductors cutting through more magnetic flux at a larger diameter. On the

other hand, although small high speed motors can offer higher power density, they require a reduction drive to the wheels in order to achieve the required torque, which itself adds weight. Whether or not a high torque motor weighs more than a high speed motor plus reduction drive remains to be seen, and will be further investigated in this research.

Cogging torque in permanent magnet motors is a commonly-identified issue when considering their use in traction applications. It is primarily due to saliency in iron stators, which results in varying magnetic reluctance as the rotor turns. The problem is effectively eliminated with iron-free designs like the CSIRO motor (Lovatt, Ramsden & Mecrow 1997) and others. Further advantages with iron-free designs are higher efficiency due to no iron losses, and a significant reduction in motor weight. However torque density appears to be the biggest challenge for iron-free designs due to the difficulty in maintaining high flux density over a much larger air gap (which had much higher magnetic reluctance than a ferromagnetic core). Eddy current losses also become more pronounced in the copper conductors since the windings themselves are exposed to a greater magnetic field. This generally requires the use of Litz wire, which reduces copper fill factor due to the extra insulation.

Some iron-core designs reviewed are based on vernier drive/LRK topology and appear to offer several advantages over conventional motor designs including lower cogging torque, shorter end windings, and easier construction. For high pole-count motors with a laminated stator core, the LRK winding seems to make sense.

As far as type of motor and overall hub layout, there are three main options commonly considered, as shown in figure 5.49.

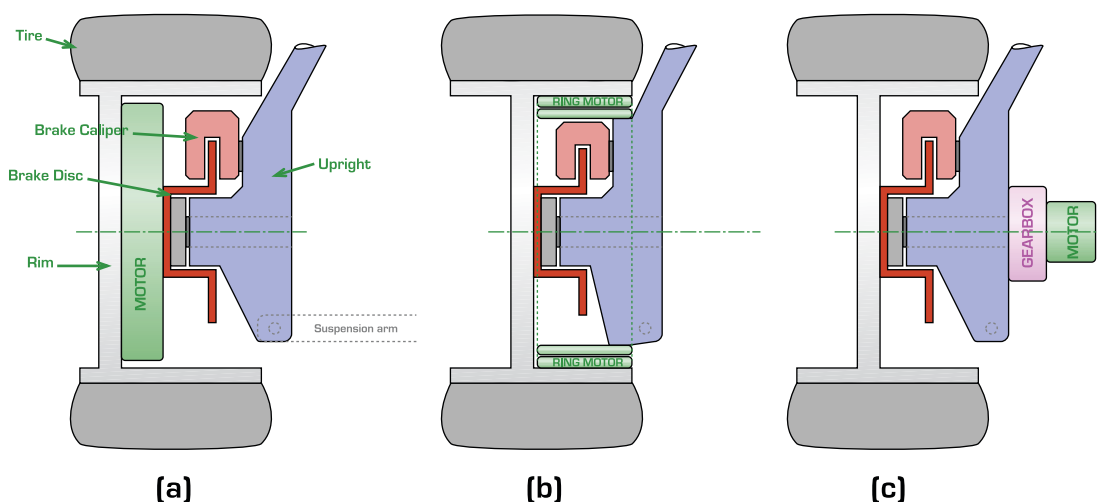


Figure 5.49: Three basic layouts for in-wheel motor drive: (a) Axial flux motor, direct drive (b) Outer-rotor (ring) motor, direct drive (c) High speed motor with reduction drive

Particularly for direct drive solutions, axial flux motors seem to have received the most attention, having a shape conducive to fitting into a wheel hub, and efficient use of space.

The other promising candidate is the outer-rotor PMSM. Its primary advantage is having a very thin rotor, with the air gap (and hence magnetic forces) occurring at a large radius with respect to motor size. As shown in Figure 5.49b, an outer-rotor PMSM could be constructed as a ring motor attached to the wheel rim itself. There are also some high performance (high speed) commercial outer-rotor PMSMs originally intended for electric aircraft which are promising candidates for an in-wheel system using a reduction drive.

As a result of this literature review, two promising solutions will be investigated further in this project through design and analysis:

- A direct drive solution, based on a large diameter, high pole-count, water-cooled, iron-less axial flux motor, with design parameters optimised through simulation and performance predicted analytically
- A reduction drive solution, based on a commercially available high-speed, convection cooled, outer-rotor PMSM motor, with motor selection based on real-world performance testing, and a variety of reduction drive systems considered.

In both cases their suitability will be considered with respect to both road-going automobiles, and the Formula SAE Electric application.

6 MAGNETOSTATIC FEA EXPERIMENTS

6.1 INTRODUCTION

Having decided on a basic motor topology to explore further, namely an axial flux PMSM with dual rotors and airgap windings, the dimensions and magnetic parameters of the design can be explored and optimised using computer aided design tools.

Ansys Maxwell SV is a 2D magnetostatic simulator which uses finite element analysis to calculate magnetic fields around magnets, materials and conductors. It is useful for visualising magnetic fields for motor designs, gain better understanding of how fields interact with different materials and magnet layouts, optimising designs, and predicting performance.

Unfortunately the software user interface leaves a lot to be desired, lacking support for basic operations such as Undo, which makes experiments cumbersome to set up. It did not appear that it supported scripting, so experiments were set up for various data points manually.

The following experiments in Maxwell SV test various design parameters such as airgap thickness, magnet thickness, backplate thickness and magnet width.

6.2 BACKPLATE MATERIAL

6.2.1 Introduction

In most PMSM motors, steel is used as a backing plate behind the rotor magnets, in order to contain the magnetic field. A simple experiment can be set up using Maxwell to observe the difference in magnetic field when using a ferromagnetic backing plate, to get a better feel for the how materials with high permeability influence magnetic fields.

The follow simulation shows two identical configurations, other than changing the backing plate material between steel (high μ) and aluminium ($\mu \sim 1$). Magnets are 12x6mm Neodymium grade 42, and backplates are 3mm thick.

6.2.2 Simulation Results

Figure 6.1 shows the Maxwell simulation result for the experiment, with colouring for magnetic flux density (0-1T range) and grey magnetic flux lines.

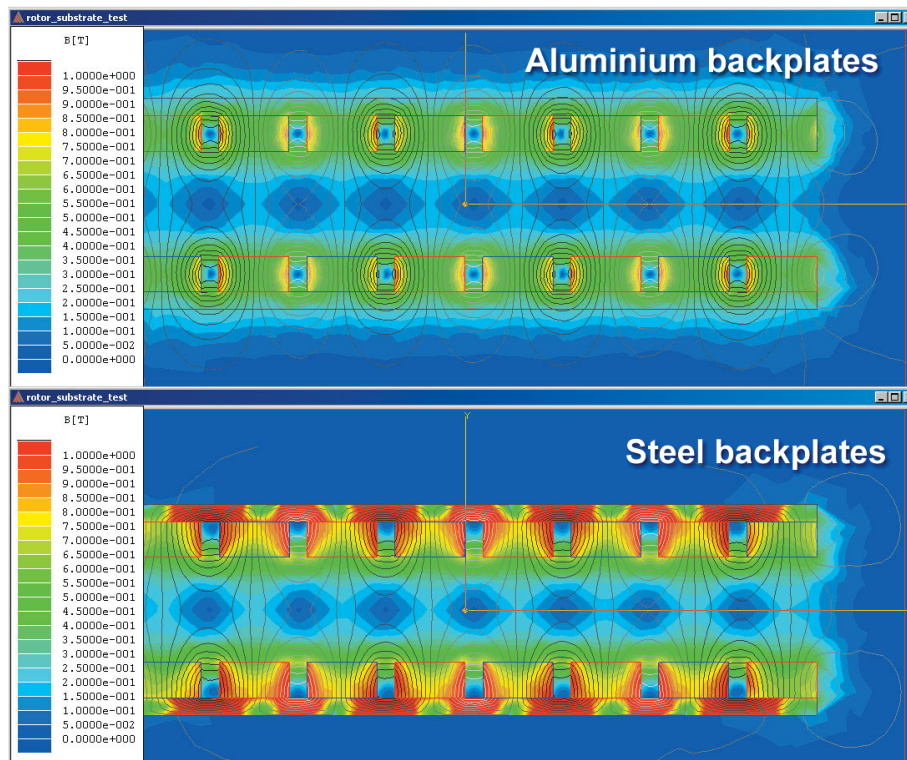


Figure 6.1: Comparison of magnetic fields for steel vs aluminium rotor backplates

Note that copper conductors have not been included in the simulation (or any to follow) since the magnetic permeability of copper is almost identical to vacuum and air (within 0.01%).

6.2.3 Summary

The FEA results clearly show how effectively steel, with its high magnetic permeability, can contain magnetic flux compared with materials such as aluminium which have a relative permeability around 1 (very close to that of a vacuum). In a PMSM motor it is preferable to avoid stray magnetic fields outside the rotor which could induce eddy currents in nearby electrically-conductive materials, such as the motor housing, and reduce operating efficiency.

Maximum field strength observed in the middle of the airgap is approximately 0.17T with aluminium substrate and 0.23T for steel – approximately a 30% increase in field strength – so it also makes a significant difference to air gap field strength.

6.3 EFFECT OF AIRGAP WIDTH

6.3.1 Introduction

Due to the relatively low magnetic permeability of air compared with the steel which makes up the majority of a motor's substrate (and magnetic flux path), most motors employ a relatively narrow air gap in the order of 1mm, in order to minimise reluctance in the magnetic flux path.

Ironless stator designs such as the one under consideration necessarily employ a larger airgap between parallel rotor poles, to allow space for stator windings. However for a given thickness of rotor magnet, the average airgap field strength falls as airgap width increases. Colton (2010) offers a formula which approximates magnetic field strength in an air gap:

$$\mathbf{B}_{\text{peak}} = \mathbf{B}_r \left(\frac{t}{t + g} \right) \quad (12)$$

Where \mathbf{B} is field strength, t is magnet thickness and g is airgap dimension. FEA may be used to check the validity of this formula. For this experiment, N35-grade neodymium magnets (peak field strength $\sim 1.3\text{T}$) of 6mm thickness and steel backplates 3mm thick are either side of a varying-width airgap, being 3mm, 6mm, 12mm and 18mm.

6.3.2 Simulation Results

Figure 6.2 shows the Maxwell simulation result for the experiment, with colouring for magnetic flux density (0-2T range) and grey magnetic flux lines.

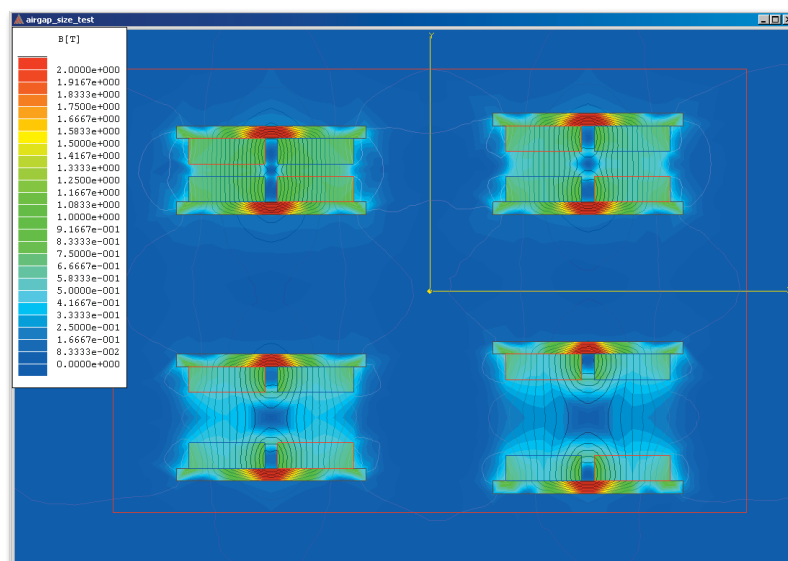


Figure 6.2: Magnetic simulation showing effect of varying air gap

The relevant simulated field strength data is represented graphically in Figure 6.3.

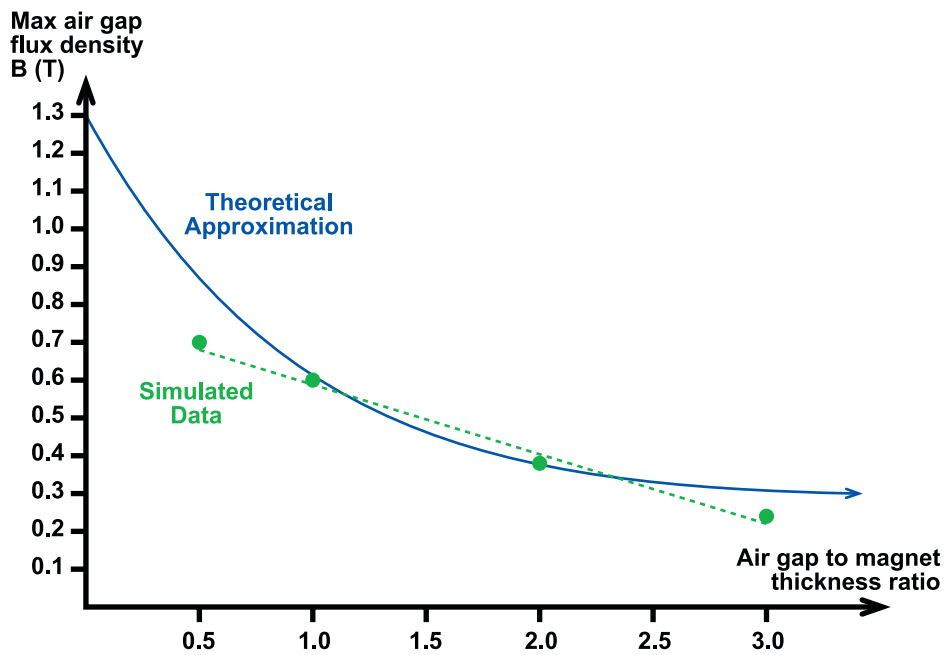


Figure 6.3: Graph of field strength for varying air gap

6.3.3 Summary

Figure 6.3 shows that there is certainly some correlation between data samples and the mathematical approximation provided by Colton (2010). However there is much less observable curvature over the range, and in fact for the experimental data acquired a linear approximation appears quite close (indicated by dotted line). For the air gap to magnet thickness ratio range of 0.5 to 3.0 above, air gap flux density may be represented with the formula:

$$B_{\text{peak}} = 0.6 B_r - 0.2 \left(\frac{g}{t} \right) \quad (13)$$

It is unlikely that the above linear relationship could be extrapolated outside the measured range since an inverse-proportional relationship makes more sense as the data approaches the extremities (axes).

6.4 BACKPLATE THICKNESS

6.4.1 Introduction

Most motor designs make use of steel's high magnetic permeability to contain and direct magnetic flux. In this experiment the significance of backplate thickness vs magnet thickness is explored.

Four scenarios are presented, in each case there are two pair of north/south magnets attached to steel back plates of varying thickness, to simulate a small section of a dual-rotor axial flux design.

Magnet thickness is 6mm and airgap thickness 6mm, with steel backplates 2mm, 4mm, 6mm and 8mm. These dimensions were chosen as typical for the size of motor in a wheel hub motor, but it is expected that results can be extrapolated for other sizes. (More significant is the ratio of magnet thickness to backplate thickness, rather than absolute sizes.)

6.4.2 Simulation results

Figure 6.4 shows the Maxwell simulation result for the experiment, with colouring for magnetic flux density (0-2T) and grey magnetic flux lines.

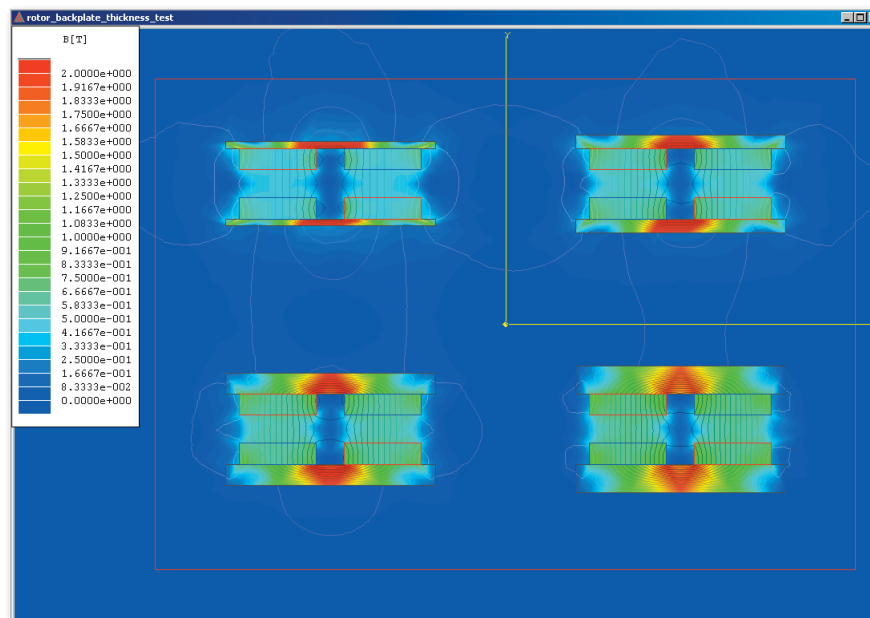


Figure 6.4: Magnetic simulation showing effect of steel backplate thickness

The peak flux observed at the centre of the airgap can be compared graphically with the maximum flux observed outside the backplates (also called flux leakage) for the four simulated cases, as shown in Figure 6.5.

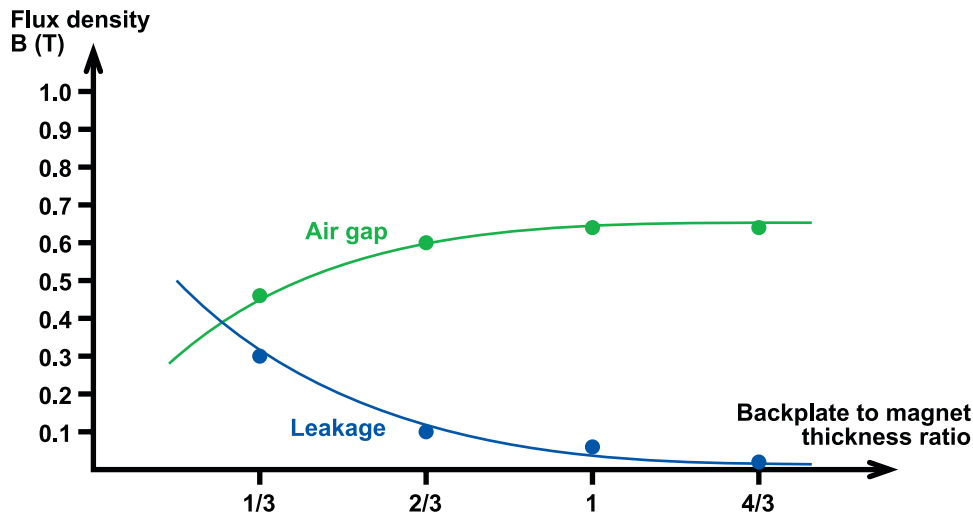


Figure 6.5: Graph of air gap flux vs leakage flux for various backplate thicknesses

6.4.3 Summary

As backplate thickness increases airgap field strength increases while leakage flux decreases, tending towards zero flux leakage and – for this simulation at least – a peak airgap flux around 0.7T. There appears to be negligible improvement beyond a backplate-to-magnet thickness ratio of 1.

Maximum flux density in the backplate is observed between the magnets rather than behind them. This validates the optimisation performed by Rahman et al (2006) who removed backplate material directly behind the magnets, having full backplate thickness only between magnets.

Magnetic saturation of the backplate steel appears to be a major factor for flux leakage. The N35 Neodymium magnets have a maximum field strength around 1.3T, and electrical steel saturates at a magnetic flux density of approximately 1.7T. It stands to reason that if the backplate is thinner than the magnets, it would need to contain a higher magnetic flux density than the magnets. This would suggest a ratio of around 1.3/1.7 or ~75% if a steel backplate is to contain the field from neodymium magnets without saturation. The simulation results appear to support this – minimal flux leakage is observed for cases where backplate thickness exceeds 75% of magnet thickness.

6.5 EFFECT OF MAGNET THICKNESS

6.5.1 Introduction

A further experiment on the same basic design involves maintaining a fixed backplate and airgap thickness, and only varying the magnet thickness.

Four cases are considered, each with 6mm steel backplate and 12mm airgap, and varying magnet thicknesses of 6mm, 12mm, 18mm and 24mm.

6.5.2 Simulation Results

Figure 6.6 shows the Maxwell simulation result for the experiment, with colouring for magnetic flux density (0-2T) and grey magnetic flux lines.

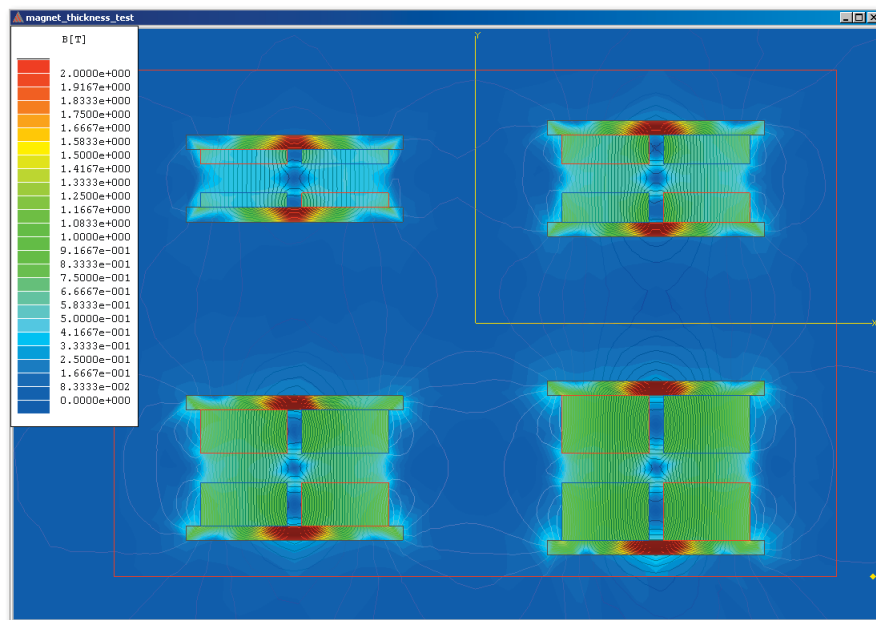


Figure 6.6: Magnetic simulation showing effect of varying magnet thickness

Peak airgap and leakage flux density can be represented graphically, as shown in Figure 6.7.

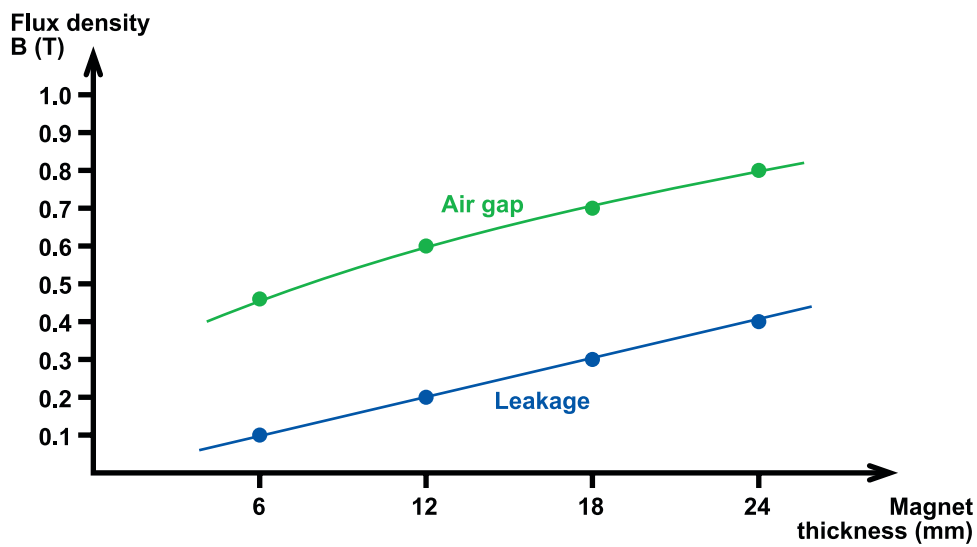


Figure 6.7: Graph of air gap and leakage flux for various magnet thicknesses

6.5.3 Summary

Fairly linear results are observed for both air gap and leakage flux densities, with both increasing as magnet thickness increases.

As discussed in section 5.3.3, it is unlikely that the linear characteristics of the data could be extrapolated far beyond the sampled range, since flux densities would necessarily be constrained between approximately 0-1.3T.

6.6 INTER-POLE LEAKAGE VS POLE PITCH

6.6.1 Introduction

The dual-rotor airgap-stator axial flux PMSM topology under consideration gets its torque from magnetic flux lines parallel to the conductors in the airgap - that is, flux passing directly from one rotor ring to the other, perpendicular to both current flow and the direction of rotation.

However as seen in previous experiments, particularly in designs with large airgaps some flux also travels between adjacent on the same rotor ring, flowing tangentially to the rotation and hence not contributing to motor torque.

In this experiment the effect of pole pitch to airgap ratio is explored over a range of 1:1 to 4:1, and the percentage of flux observed as inter-pole leakage rather than inter-rotor is measured.

6.6.2 Simulation Results

Figure 6.8 shows the Maxwell simulation result for the experiment, with colouring for magnetic flux density (0-1T) and grey magnetic flux lines.

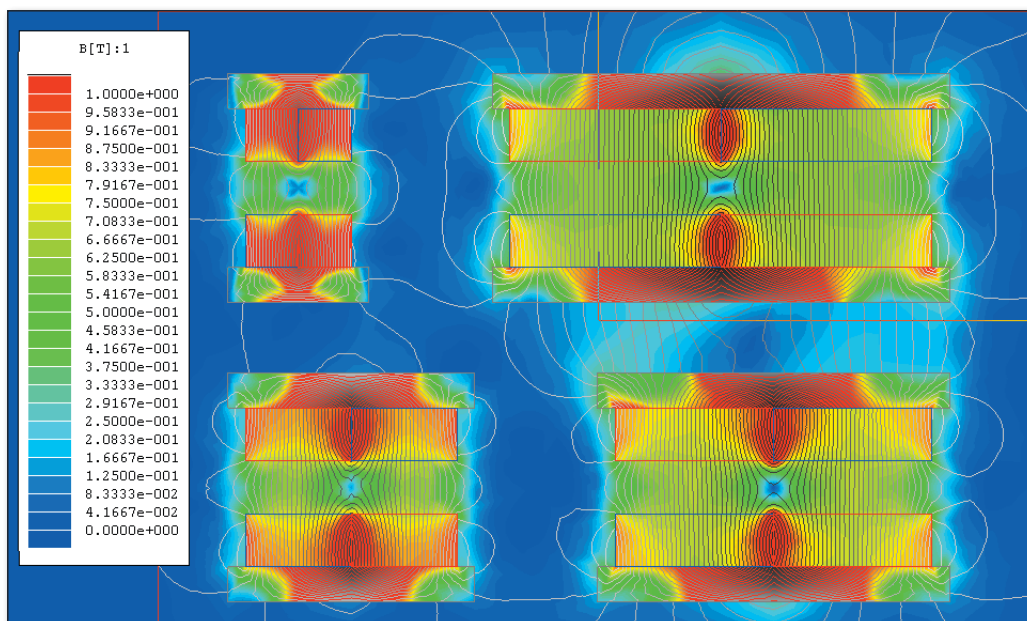


Figure 6.8: Magnetic simulation showing flux for various pole pitch to airgap ratios

The relevant data from the simulation can be displayed graphically, shown in Figure 6.9.

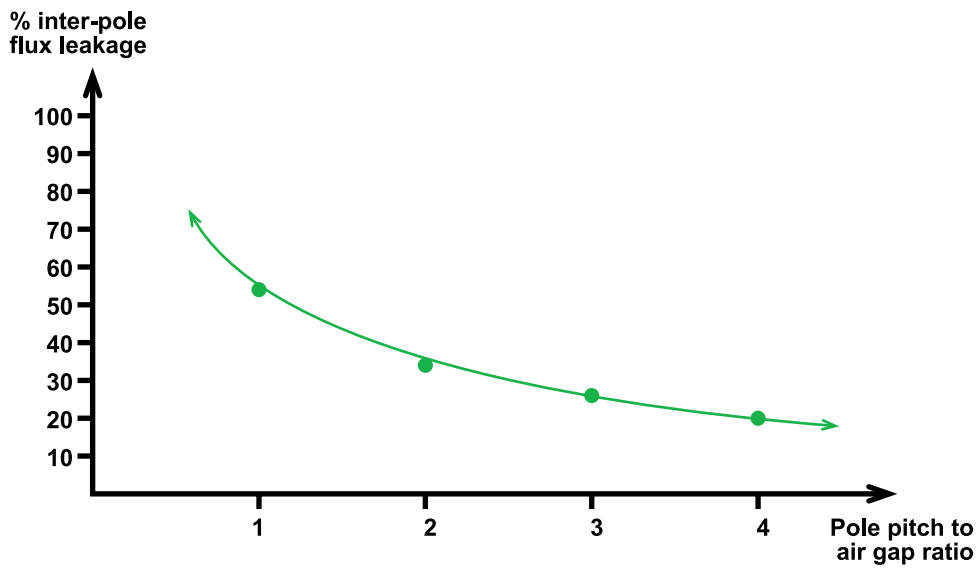


Figure 6.9: Graph of inter-pole leakage vs pole pitch:airgap ratio

6.6.3 Summary

As expected, the lower the pole pitch to airgap ratio, the more inter-pole flux leakage is observed. The data from the simulation correlated very closely with an inverse proportional relationship, calculated to match the following formula:

$$\% \text{ leakage} = \frac{1}{1 + \frac{\text{pole pitch}}{\text{air gap size}}}$$

Also observed during this experiment is that magnet width vs backplate thickness appears to have a significant effect on leakage flux, with an increasing portion of the backplate material in saturation due to an increasing amount of total magnetic flux as magnet width increases.

6.7 EFFECTIVENESS OF HALBACH ARRAY

6.7.1 Introduction

As mentioned in section 3.3, Halbach Arrays offer a method of directing and containing flux between magnets using extra intermediate magnets. It is interested to visualise this effect on a magnetic field, and quantify the efficacy with respect to a dual-rotor AFPM motor design.

Three cases are compared, firstly a Halbach Array with intermediate magnets at 90-degree polarity to main field magnets. The second case is a standard row of magnetic dipoles with no back plate. The third case is similar to the second with the addition of steel backplates, which is the usual method of containing the magnetic field in a motor.

6.7.2 Simulation Results

Figure 6.10 shows the Maxwell simulation result for the experiment, with colouring for magnetic flux density (0-1T) and grey magnetic flux lines.

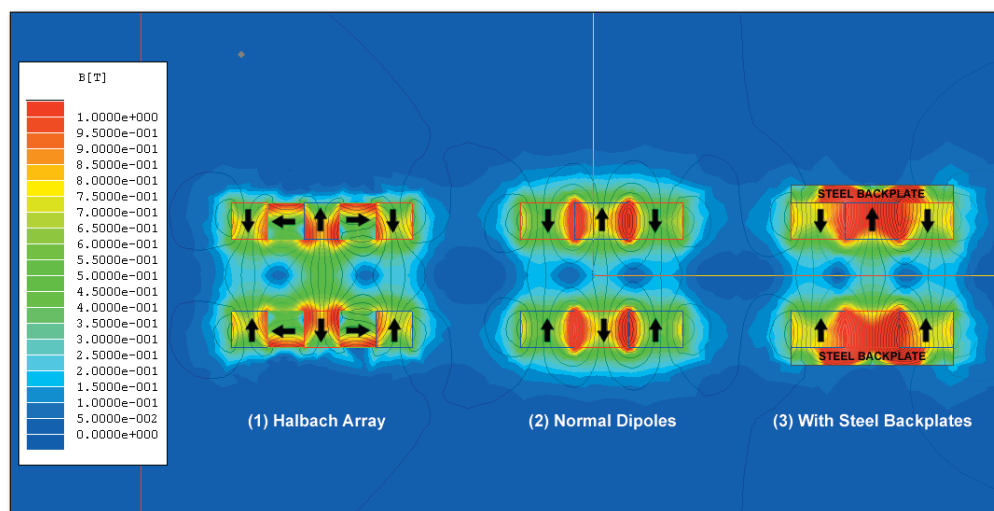


Figure 6.10: Magnetic simulation comparing Halbach Arrays with typical magnet arrangements

The magnetic field strength at various point of interest can be read from the above results.

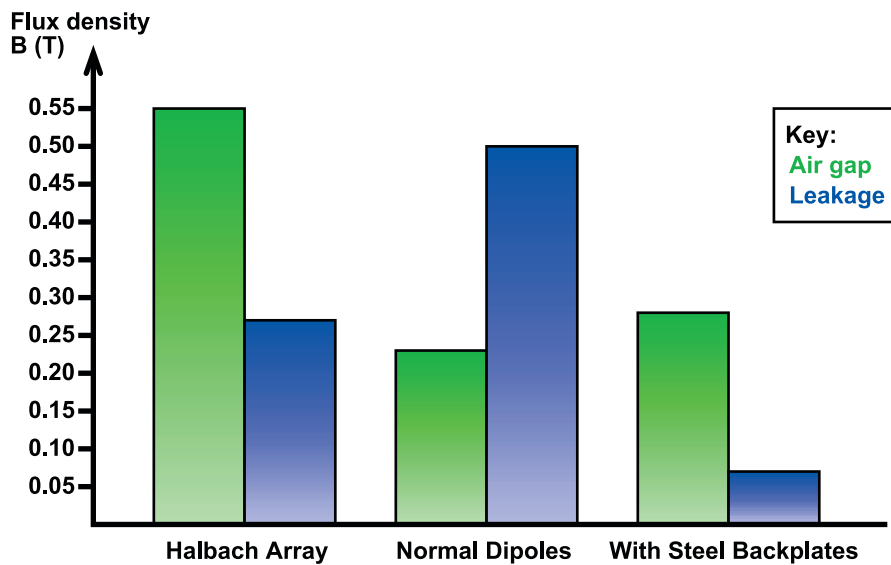


Figure 6.11: Graphical comparison of air gap and leakage flux for Halbach vs typical configurations

In each case air gap flux measurements are the strongest observed at the midpoint between paired magnet arrays, and leakage flux stated is the measured immediately behind the same magnets.

6.7.3 Summary

This simulation demonstrates that Halbach Arrays offers clear advantages to standard dipole configuration, approximately doubling the airgap field strength and reducing leakage by more than half.

Steel did prove to be more effective at containing the magnetic field and reducing leakage flux, though interestingly its effect on improving air gap flux density was not as pronounced (a similar result observed to that from section 5.1).

It is possible that a combination of Halbach Array plus (relatively thin) steel backplate may offer the optimum solution for both airgap flux density and minimum leakage flux.

6.8 SUMMARY OF RESULTS

In this chapter, magnetostatic FEA simulation tool Ansys Maxwell SV has been used to investigate the magnetic field produced in a dual-rotor axial flux PMSM with airgap stator. By varying the geometry of various parameters, simulation results can help in optimising machine dimensions. As is often the case, many parameters represent design trade-offs.

Regarding airgap width, the greater it is, the lower the airgap flux density. Some space is needed for stator windings of course, so it would seem reasonable to use an airgap width in the order of 1-2x magnet thickness.

Steel backplates are very effective at containing magnetic flux. The thicker the backplate used, the lower the flux leakage, but with diminishing gains. A backplate thickness approaching the magnet thickness appears to offer sufficiently good flux containment.

In any motor design there is some flux which travels between adjacent magnets rather than across the air gap. The narrower the pole pitch compared with the airgap width, the higher this inter-pole leakage flux as a percentage of total flux. It appears that magnets should be 3+ times wider than the airgap is thick, in order to keep this leakage at a reasonable level. This will limit the feasible pole count for any motor.

Halbach Arrays appear to be very effective at raising airgap flux density, which is very important for motor performance. However the flux behind the array is not as well contained as with a steel backplate, so a combination of Halbach Array plus steel backplate will offer the best combination of high airgap field strength and minimum leakage flux.

7 DIRECT DRIVE DESIGN & ANALYSIS

7.1 INTRODUCTION

The first in-wheel solution to explore is using a direct-drive motor. This is a more elegant solution since it features fewer moving parts, and should offer lower maintenance and higher efficiency. The disadvantage is that torque requirements from the motor are much higher.

A review of similar research of in-wheel drive systems identified axial flux PMSM as a promising candidate. In this chapter an optimal design is attempted based on understanding gained through FEA experiments, and research on similar projects.

The FEA simulations described in chapter 6 demonstrate that there is a complicated interplay of many variables in motor design. Greaves, Walker & Walsh (2001) identified many design variables for AFPM motors such as magnet dimensions, active axial length, peak magnetic flux density, back-EMF waveform, number of poles, average radius of air gap, thickness of stator, mass of the machine, gauge of litz wire, etc. Many of these are dictated by the constraints of the application, and several others can be decided based on FEA results.

7.2 DESIGN DECISIONS

The main physical constraint for the motor is that it must fit inside a typical 13x6" Formula SAE wheel. This limits the outer diameter to approximately 300mm. Allowing some space for housing and cooling tube, it leaves approximately 250mm for the rotor diameter.

The conductors in an AFPM motor are aligned radially, as such the total conductor cross section is limited by the inner airgap circumference and width, with lower fill factor at the outer radius. However a smaller inner airgap does mean a larger airgap area, and more active conductor length, so a trade-off is required. Versele et al (2009) found that an inner radius at 58% of the outer radius was the optimum value.

As such an inner radius of approximately 145mm would be ideal. For ease of manufacturing, an inner airgap diameter of 144mm and outer 244mm was chosen, giving 50mm magnet height. A Halbach Array plus steel backplate has been identified as the best way to both maximise airgap flux density and minimise leakage flux. A simple Halbach Array based on primary wedge magnets and 90° rectangular magnets between was chosen to keep manufacturing simple.

With magnets 6mm thick, an airgap thickness of 8mm was chosen as a compromise between field

strength and space for stator windings. A high pole-count was desirable for torque production and shorter end windings (Rajagopal & Sathaiah 2006), but poles couldn't be too narrow without excessive flux leakage between adjacent magnets. A 24-pole design results in an average pole pitch to airgap thickness ratio of just over 3:1, which should be acceptable based on earlier FEA simulation results.

The airgap winding need to be embedded in some substrate to provide mechanical strength. Potting windings in epoxy or injection moulded plastic seems like a viable solution. With any motor having airgap windings the conductors themselves it is necessary to use Litz wire to avoid excessive eddy currents, though it reduces copper fill factor by approximately 25% (Greaves et al 2003).

Since the motor would be operating in a dirty environment, water cooling rather than convection cooling through the motor would be the best way to remove heat. An idea for this is to use a circumferential cooling tube similar to Rahman et al (2006), except actually wrapping the conductors around the tube for optimum heat transfer. The downside with this concept is longer end windings which reduce the copper utilisation factor.

7.3 PROPOSED DESIGN

Based on these design decisions, the following design was created.

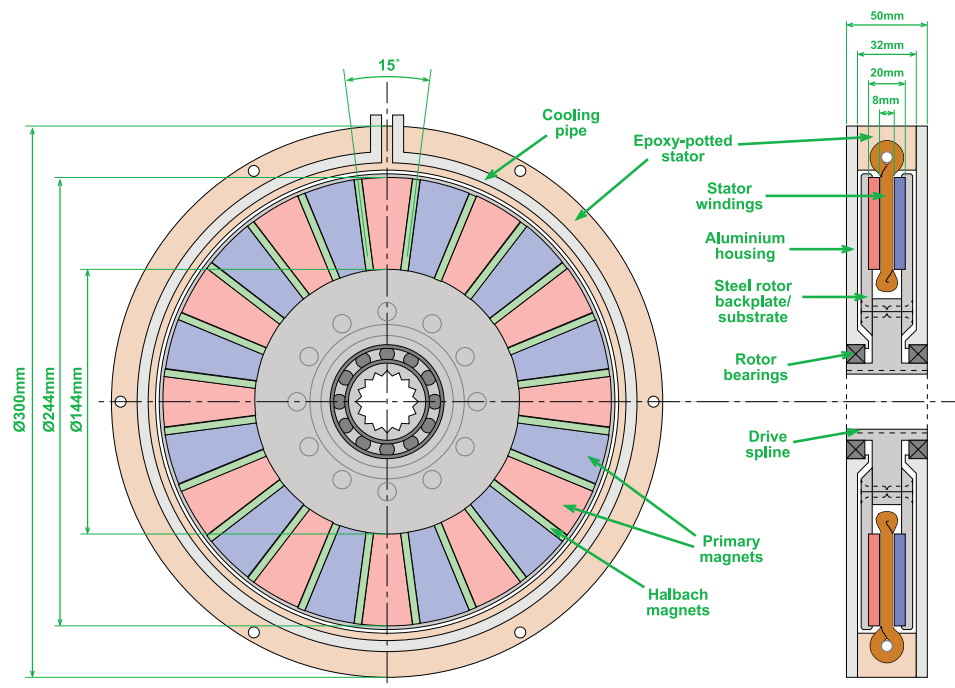


Figure 7.1: Orthographic projection of proposed axial flux PMSM motor

The stator winding design is basically the same as the airgap-winding inner-torus topology, minus the iron core and with windings combined into a single plane.

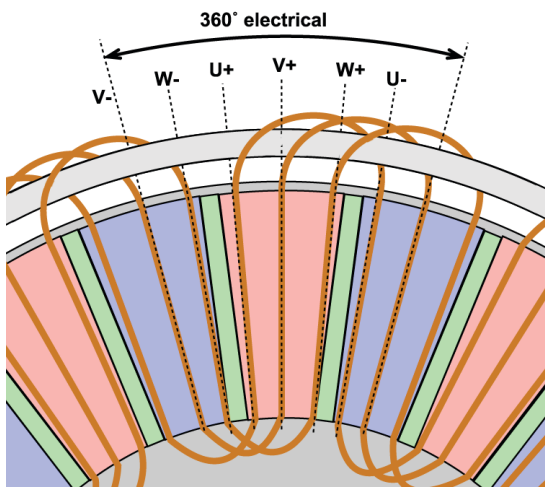


Figure 7.2: Winding diagram (conductors shown at reduced diameter for clarity)

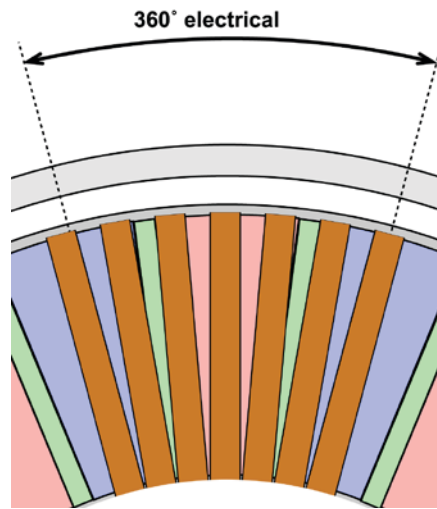


Figure 7.3: Actual active conductor fill factor

Conductor bundles 6mm diameter were chosen to maximise fill factor at inner airgap radius. With an 8mm airgap this gives an acceptable 1mm clearance on either side of conductors to the rotors. Table 7.1 summarises the general motor specifications.

Table 7.1: Motor specifications

Technology	Permanent Magnet Synchronous Motor
Topology	Axial Flux, dual rotor, ironless stator, airgap winding
Dimensions	Ø300mm x 44mm
Rotor	Dual 24-pole Halbach Array, ID Ø144mm, OD Ø244mm
Stator	Airgap-winding, Ø6mm Litz wire conductor bundles, epoxy-potted
Cooling	Circumferential aluminium heat pipe
Motor body	Aluminium end plates, epoxy stator

Mass properties for the motor are summarised in Table 7.2.

Table 7.2: Mass properties

Component	Material	Mass
Rotor		
Backplates	Silicon steel (8g/cm ³)	2 @ 1545g
Magnets	NdFeB (7.5g/cm ³)	48 @ 64g + 48 @ 12g
Hub	Silicon steel (8g/cm ³)	1170g
Stator		
Conductors	Copper (9g/cm ³)	1510g
Epoxy substrate	Epoxy (1g/cm ³)	690g
End plates	Aluminium (2.7g/cm ³)	180g
Bearings	Steel (8g/cm ³)	80g
Machine screws	Steel (8g/cm ³)	70g
Total:		10438g

A total weight of approximately 10.4kg is calculated for the motor.

The fitment of this motor into a typical Formula SAE wheel hub is shown in Figure 7.4.

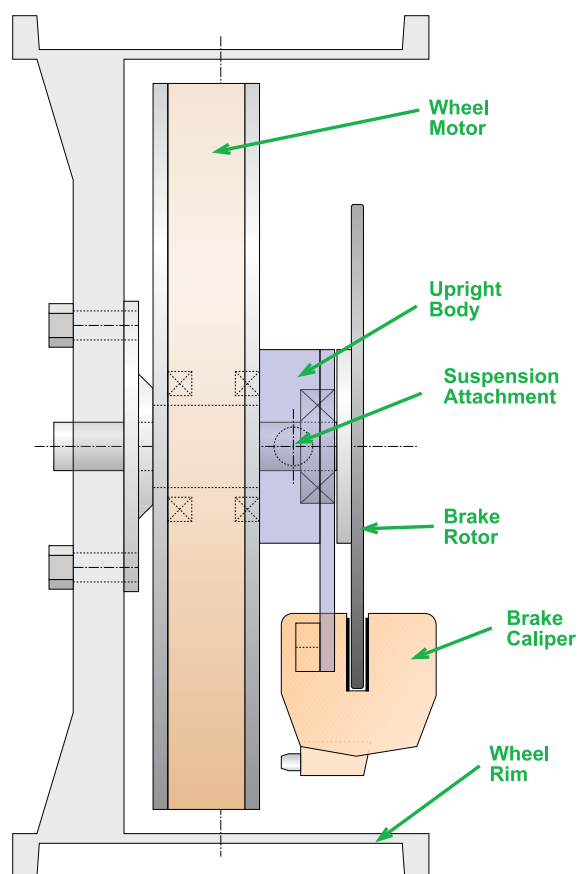


Figure 7.4: Proposed hub layout with direct drive motor (top view)

7.4 THEORETICAL PERFORMANCE ANALYSIS

7.4.1 Copper Fill Factor

Fill factor is a measure of how much of the stator volume is made up of conductor. In general, the higher the better since it allows for more current flow in more magnetic field. With axial flux motors, since the circumference of the airgap varies depending on the radius, it is common to use the middle of the airgap as an average.

The maximum conductor bundle diameter is 6mm. Assuming 75% fill factor in the bundle itself due to Litz wire insulation (Greaves et al 2003), the copper area is 21mm².

The centre of the airgap has a circumference of 609mm and width of 8mm, equating to an area of 4875mm². With 72 conductors in this area (24 poles x 3 phases) there is 1512mm² of copper, which means a fill factor of 31%.

7.4.2 FEA Simulation

The airgap flux density can be determined through FEA simulation using Ansys Maxwell SV. The results are shown in Figure 7.5.

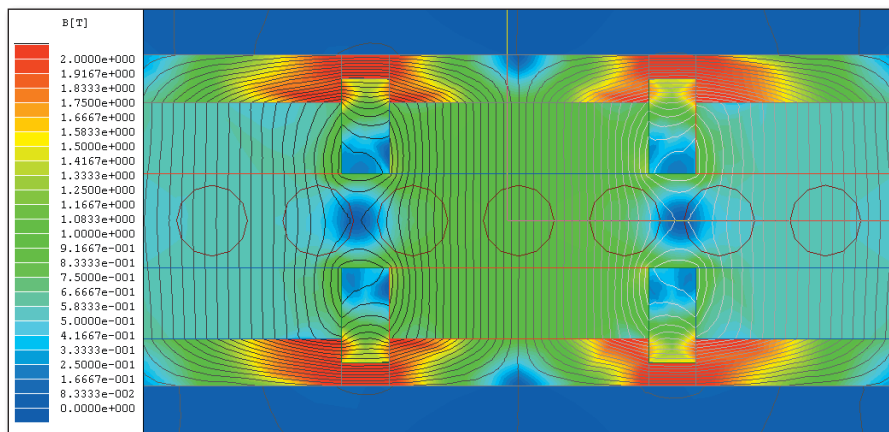


Figure 7.5: Maxwell simulation of proposed motor

Outlines of the stator conductors also visible in the airgap. Note that only the central third is representative of the real rotor flux, since side magnets are missing adjacent Halbach and primary magnets which clearly influence flux density. The flux density observed over one pole span can be graphed as shown in Figure 7.6.

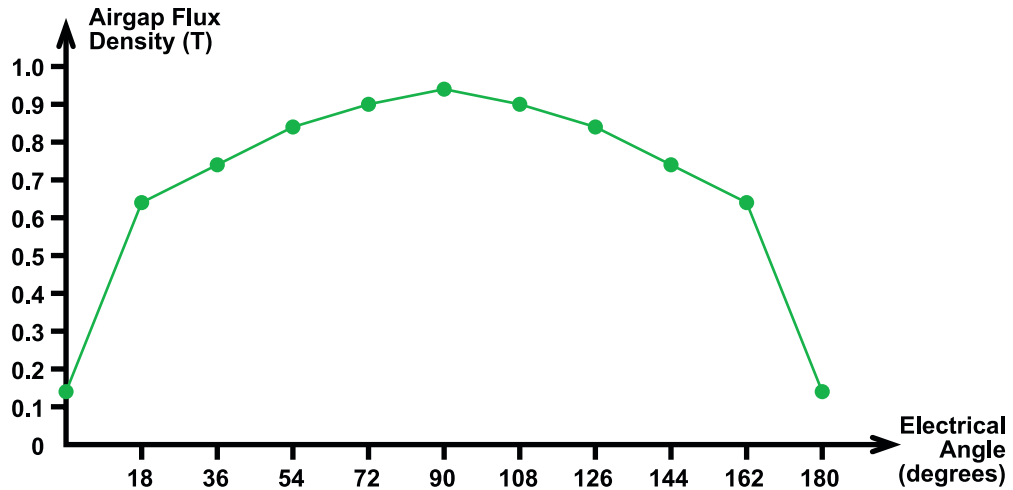


Figure 7.6: Plot of airgap field strength

A peak airgap flux density of 0.95T is observed, with RMS magnitude of 0.74T.

7.4.3 Estimating Torque/Speed Characteristics

Rigorous mathematical models of ironless AFPM motor are very complicated (Ravaud, Lemarquand & Lemarquand 2009) and beyond the scope of this thesis, but reasonable approximations can be made with a combination of FEA simulation (as performed in the previous section) and magnetic theory.

Colton (2010) covers a method for approximating the torque constant of a PMSM motor, derived via Lorentz's law:

$$F = BIL$$

$$\text{Active conductor length: } L_{\text{active}} = N_{\text{turns}} \cdot L_{\text{stator}} \cdot 2$$

$$\text{Torque: } \tau = \text{Force} \cdot \text{Radius}$$

$$\tau = 2NIBLR$$

$$\text{Torque constant: } K_t = \tau / I$$

$$= 2NBLR$$

Where N is the number of active turns in the motor, B the flux density, L is the stator stack length and R the airgap radius. Analysis of AFPMs are usually based on average airgap radius, $R_{\text{ave}} = (R_{\text{in}} + R_{\text{out}}) / 2$. (Versele et al 2009).

Table 7.3: Estimating motor torque constant K_t

Active turns, N	36
RMS airgap flux density, B	0.74T
Active conductor length, L	0.050m
Airgap radius, R_{avg}	0.097m
Torque constant, $K_t = 2NB_L R$	0.129 Nm/A
Speed constant, $K_v = 1/ K_t$	7.75 rad/s/V (74rpm/V)

7.4.4 Estimating Torque Ratings

A basic way to get a feel for continuous torque is to use the NEC ampacity rating based on the conductor cross-sectional area. In this case, insulated 21mm² copper is rated to 95A (to 90°C). With a torque constant of 0.129 Nm/A, this equates to continuous torque of 12Nm.

A better estimate is based on motor heat buildup vs heat dissipation. In the case of ironless motors, copper loss is the primary source of inefficiency (Lovatt, Ramsden & Mecrow 1997). Copper loss can be calculated as follows:

$$\text{Resistive power loss} \quad P = I^2 R$$

$$\text{Winding resistance} \quad R = \rho L / A$$

$$\text{Total conductor length} \quad L_{total} = (L_{active} + L_{end}) \times N_{poles} \times N_{phases}$$

$$\text{Hence,} \quad P = I^2 \frac{\rho (L_{active} + L_{end}) \times N_{poles} \times N_{phases}}{A} \quad (14)$$

With a copper's resistivity $\rho = 1.68 \times 10^{-8}$ and taking active length 50mm, end windings of 60mm, 24 poles, 3 phases and 21mm² conductor area, we get:

$$\text{Hence,} \quad P = I^2 \frac{1.68 \times 10^{-8} (0.05 + 0.06) \times 24 \times 3}{0.000021}$$

$$P = 0.00634 I^2$$

This can be represented graphically as follows:

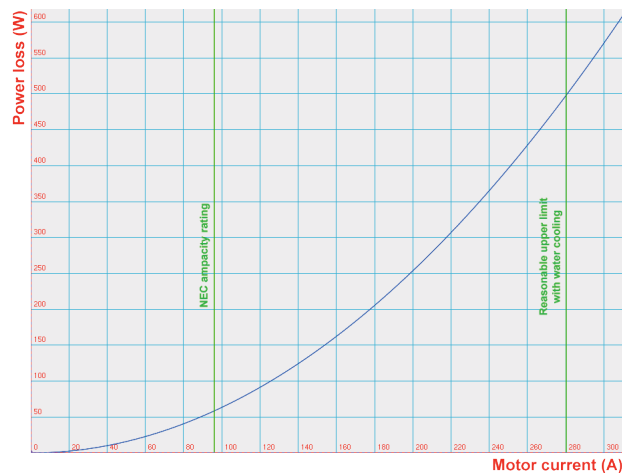


Figure 7.7: Graph of resistive power loss vs motor current

The two green lines indicate the NEC ampacity rating for the conductors, equating to a heat around 60W, and a second for a reasonable upper limit for a motor with good water cooling able to remove 500W of heat, which would represent a limit of 280A (36Nm torque).

With a torque constant of 0.129 Nm/A, the peak torque requirement of 108Nm per wheel (433Nm for all four) would require 837A of RMS motor current, which would result in 4.4kW of heat. Unfortunately, this figure seems unfeasibly high.

7.5 CONCLUSION OF FINDINGS

This chapter has presented the design of an axial flux wheel motor. Design decisions were based on a combination of research on similar motors, magnetostatic FEA simulations, and various constraints imposed by the application (such as fitting inside a typical Formula SAE rim). From this a 24-pole axial flux PMSM design was created based on dual Halbach Array rotors either side of a stator featuring airgap windings with epoxy substrate.

Analysis of the design including performance estimates were performed. Based on these estimates, it appears that the design would unfortunately be unable to meet the torque requirements for a Formula SAE vehicle.

The motor presented is only an early conceptual design, and without further analysis (or prototyping) it is uncertain if tolerances between rotor and stator components is sufficient, i.e if the rotors are rigid enough to maintain less than 1mm deflection under extreme conditions.

8 COMMERCIAL MOTOR TESTING

8.1 INTRODUCTION

Due to the lack of motors available which are suitable for direct drive in-wheel use, and the inadequate torque performance of the direct drive motor design presented in Chapter 7, a drive system based on a high-speed motor plus reduction drive was explored.

Over the course of this project, three different motors were purchased as candidates for in-wheel motor systems. All three are outer-rotor PMSM vernier drive motors based on LRK design, originally intended for electric aircraft (which shares the high power density requirements of in-wheel motor systems).



Figure 8.1: From left to right: Plettenberg Predator 37, Turnigy CA120-70, Turnigy CA80100-130

The specifications of each motor are summarised in Table 7.1.

Table 8.1: Specifications of motor candidates

Motor	Claimed Power	Weight	Max Voltage	Max Current	KV (rpm/V)	Price (~AU\$)*
Turnigy CA80100-130	6.5kW	1.6kg	48V	130A	130	\$120
Plettenberg Predator 37	15kW	1.9kg	48V	300A	150	\$1100
Turnigy CA120-70	15kW	2.6kg	48V	300A	150	\$300

*Prices as of mid-2011.

The smallest of the three is too small to meet the power requirements for this project, but was purchased first for early prototyping/testing. The other two motors both claim to offer sufficient power. Plettenberg motors are made in Germany, whilst Turnigy motors are made in China and are much lower priced for equivalent (claimed) power, so one of the priorities for testing was to determine if there was a performance difference to justify the cost.

Being designed for electric aircraft use – that is, spinning a propeller – where there is minimal requirement for stall/starting torque, the motors do not include any rotor position sensors (e.g magnetic Hall Effect sensors) and were designed for sensorless control. However for traction applications a high starting torque is required which generally requires rotor position sensors. These can be added to sensorless motor designs (Endless Sphere 2009).

In this chapter a variety of experiments are performed on the motors to evaluate performance and discern suitability for in-wheel motor use. Firstly the basic design of each motor is compared. Also a range of experiments were performed with the motors to evaluate their performance, including magnetic leakage, back-EMF, Hall sensor modification, no-load operation, and performance under load.

8.2 DESIGN ANALYSIS

8.2.1 Introduction

The performance of any motor is of course constrained by the laws of physics, but well designed motor will be designed to maximise performance while minimising detrimental effects such as resistive losses, eddy current losses and magnetic saturation effects. It is also possible to estimate motor performance based on dimensional analysis and application of magnetic theory.

8.2.2 Physical Measurements

The following table summarises measurements taken from the motors.

Table 8.2: Dimensional analysis of motors

Parameter	Plettenberg Predator 37	Turnigy CA120-70
Topology	PMSM vernier drive (distributed LRK design)	
Construction	Aluminium core & mounting brackets, laminated steel stator, steel rotor can, copper Litz wire windings	
Weight	1860g	2470g
Outer diameter	103mm	118mm
Body length	85mm	79mm
Centre shaft diameter	12mm	n/a (coreless)
Rotor		
Can thickness	2mm	2.6mm
Magnet size	40 x 10 x 2mm	30 x 10 x 2.6mm
Airgap width	~1mm	~1mm
Number of poles	20 (10 pair)	28 (14 pair)
Stator		
Number of slots	24	24
Stator diameter	93mm	106mm
Stator stack length	40mm	30mm
Lamination thickness	0.33mm (120 total)	0.33mm (90 total)
Stator tooth size	4x40mm (160mm ²)	4x30mm (120mm ²)
Slot depth	12mm	22mm
Wire size (approx)	Ø3.0mm (~4.8mm ² *)	Ø5.0mm (~13.3mm ² *)
Wire turns per stator tooth	3	3

* Estimate based on 90% fill factor for hex-packed conductors plus 75% compensation for Litz wire insulation

8.2.3 Design Analysis and Discussion

As first seen in Chapter 7, a method for approximating the torque constant of a PMSM motor, derived via Lorentz's law:

$$\text{Torque constant: } K_t = 2NBLR$$

Where N is the number of active turns in the motor (always 2 of 3 phases for trapezoidal commutation), B the flux density, L is the stator stack length and R the airgap radius. Also from Colton (2010) we can approximate flux density using:

$$\mathbf{B}_{\text{peak}} = \mathbf{B}_r \left(\frac{t}{t + g} \right) \quad (15)$$

Where t is the magnet thickness, g the airgap thickness, and B_r the remanence of the permanent magnets (typically 1.3T for neodymium).

Table 8.3: Estimating motor torque constant K_t

	Plettenberg Predator 37	Turnigy CA120-70
Active turns, N	48	48
PM remanence, B_r	1.3T	1.3T
Magnet thickness, t	2mm	2.6mm
Airgap thickness, g	1mm	1mm
Airgap flux density, B	0.8T	0.94T
Stator stack length, L	0.040m	0.030m
Airgap radius, R	0.047m	0.054m
Torque constant, $K_t = 2NBLR$	0.072 Nm/A	0.073 Nm/A
Speed constant, $K_v = 1/K_t$	13.7 rad/s/V (132rpm/V)	13.7 rad/s/V (130rpm/V)

Despite differences in design the torque and speed constants are almost identical. (The larger radius, thicker magnets and higher pole count of the Turnigy is offset by the longer stator length of the Plettenberg.)

A significant difference between the two motors is conductor size, with almost 3x larger copper cross-section for the Turnigy. Since copper losses due to resistance are proportionate to resistance and hence inversely proportional to conductor area, this would certainly have a large effect on maximum continuous power rating. Unfortunately continuous current ratings depend greatly on efficacy of cooling systems so are hard to quantify in isolation, but for reference the NEC ampacity rating of 5mm² copper wiring is 40A, and 13.3mm² copper is 75A, suggesting the Turnigy may have up to twice the continuous current rating. (Smaller wires have proportionally more surface area for cooling, so current ratings do not increase linearly in practice.)

In order to keep eddy current losses low, both motors use 0.33mm thick stator laminations. This is particularly important for high pole-count motors which have correspondingly high electrical/magnetic frequencies compared with their rotation speed, since eddy current losses are proportional to electrical frequency. With LRK motors, mechanical speed is slower than electrical frequency by a factor of the pole pair count. As such at a given mechanical speed, the Turnigy with 14 pole pairs will have 40% higher eddy current losses than the Plettenberg with 10 pole pairs. This may be significant, especially at high RPM.

8.3 MAGNETIC LEAKAGE TESTING

8.3.1 Introduction

Outer-rotor PMSM motors are usually constructed with thin rotor magnets attached to the inside of a steel cylinder, referred to as the rotor can. For all such motors there is some magnetic flux from the permanent magnets which extends beyond the outer steel rotor can. In a good design the vast majority is contained by the can, but minimising leakage flux requires the use of thicker and/or better (higher magnetic permeability) rotor materials.

Magnetic flux leaking outside the rotor can interact with any nearby electrically-conductive materials, causing eddy current heating and braking effects. Also as observed in section 5.4, higher leakage flux usually also corresponds with a proportional decrease in magnetic flux density inside the motor, which detrimentally affects the motor's performance.

A corollary to having some leakage flux is the ability to detect rotor magnet position from outside the rotor can. A common latching Hall Effect sensor has a maximum switching threshold for magnetic flux density of 40 gauss (4×10^{-3} Tesla), so if we can verify that leakage flux is comfortably higher than this value for a motor, rotor position sensors can be added to the outside of the rotor, which is easier than attempting to modify the motor's internals.

8.3.2 Method and Materials

For this experiment, an Allegro A1301 linear Hall Effect sensor is used to measure magnetic field strength. The sensor is placed on the rotor can at regular 2mm intervals over the span of one pole pair, and the sensor output voltage is measured with a multimeter. The A1302 sensor has a sensitivity of 2.5mV per gauss (mV/G) and a total range of ± 1000 gauss (0.1T).

A diagram of the experimental setup is shown in figure 8.2.

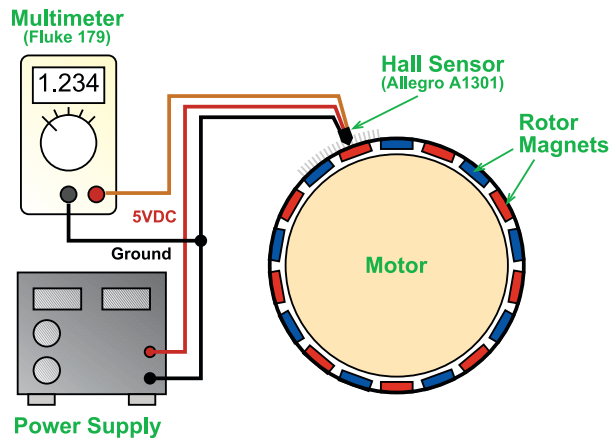


Figure 8.2: Diagram of setup for magnetic leakage test

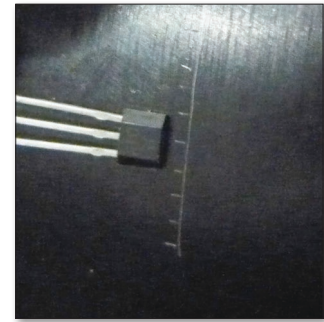


Figure 8.3: Hall sensor and position markings on motor can

8.3.3 Results

The following measurements were recorded for the three motors:

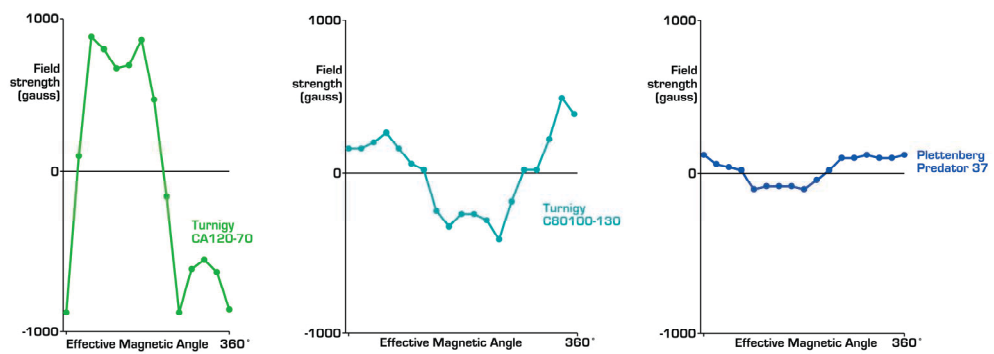


Figure 8.4: Individual graphs of motor magnetic field leakage

Combined into one graph including phase correction yields the following:

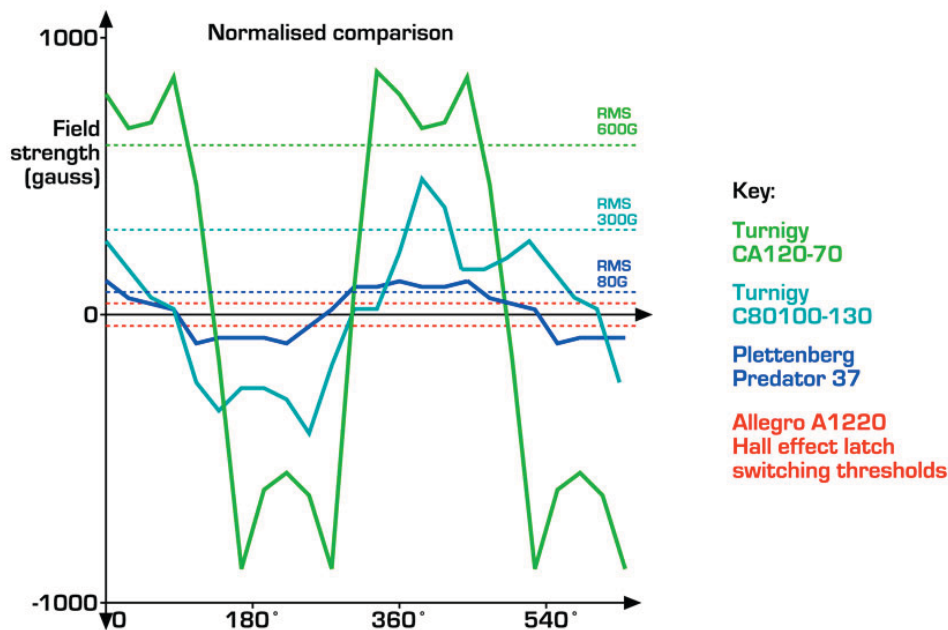


Figure 8.5: Combined and phase-corrected graph of motor leakage

8.3.4 Discussion

The salient points to note from these results include:

- The Turnigy CA120-70 has approximately 8 times higher leakage flux density than the Plettenberg Predator 37. Since rotor can thickness is comparable, the huge difference may be due to an inferior grade of steel used for the rotor can, or some other saturation effects from the motor design.
- Both motors have well above the required 40 gauss worst-case threshold for switching an Allegro A1220 Hall Effect latch, which will facilitate adding rotor position sensors to the outside of the rotor cans.
- Peak field strength of typical neodymium rare earth magnets is approximately 1.2 Tesla (12000 gauss), so the Turnigy appears to be leaking around 6% of its magnetic field – a significant percentage, and it would be best to avoid installation near electrical conductors which may see induced eddy currents, and cause increased drag on the rotor.

8.4 BACK-EMF TESTING

8.4.1 Introduction and Method

All PMSM motors have a certain constant which relates both the ratio of no-load voltage to speed, and current to torque. This is known as the motor velocity constant K_v , usually represented in the units of rpm per volt. K_t is sometimes used to represent the torque constant of a motor in amps per Newton-metre, and is the reciprocal of K_v (in SI units). These constants are useful to simply calculate the maximum speed and torque of a PMSM for a given maximum voltage and current from the motor controller. In analysing the results of this experiment we assume a 48V 300A controller such as a Kelly KBL48301, as used in later experiments.

K_v and K_t can be measured by sampling the back-EMF waveform of the motor between any pair of phases with an oscilloscope while rotating the motor at a steady speed. From the back-EMF waveform, we can also glean the optimum output waveform from a motor controller which would result in minimum torque ripple (Colton 2010).

Only the two larger motors were tested, namely the Plettenberg Predator 37 and the Turnigy CA120-70. Motors were excited at approximately 500rpm (K_v is independent of speed so actual speed does not affect result), and back-EMF waveform viewed on an Atten ADS1102CAL 100Mhz digital storage oscilloscope.

8.4.2 Results

Figure 8.6 and 8.7 show the back-EMF waveforms observed for the Turnigy CA120-70 and Plettenberg Predator 37 respectively.

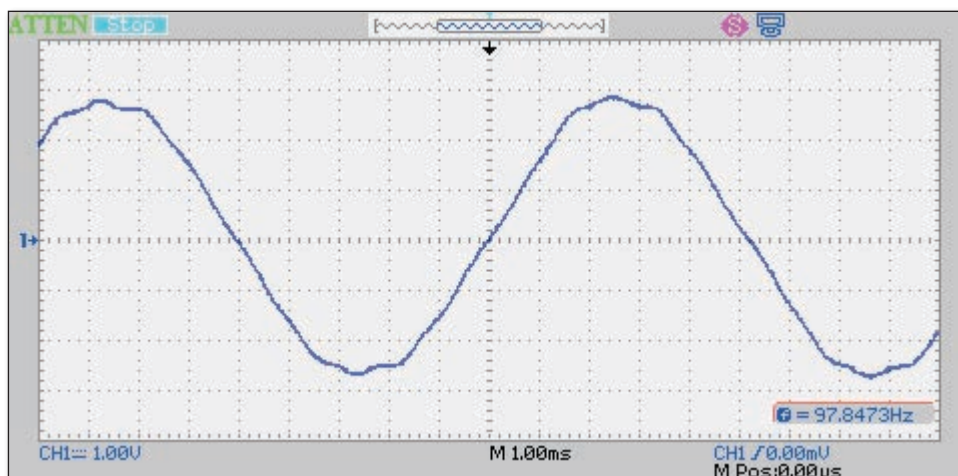


Figure 8.6: Back-EMF waveform for Turnigy CA120-70

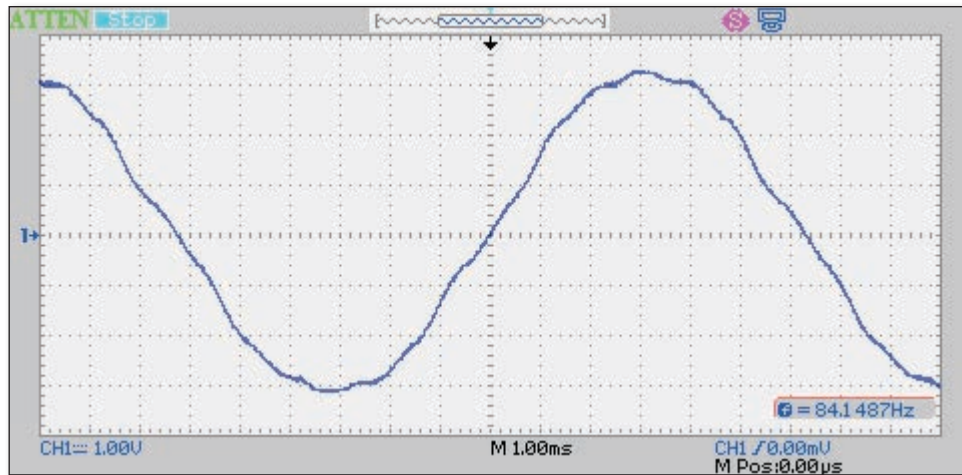


Figure 8.7: Back-EMF waveform for Plettenberg Predator 37

The value of KV may be calculated from the waveforms as follows:

Table 8.4: Calculations for Kv and Kt constants

Turnigy CA120-70	Plettenberg Predator 37
2.85V peak @ 97.8Hz electrical frequency	3.25V peak @ 84.1Hz electrical frequency
$F_{\text{mechanical}} = 97.8 \div 14$ (pole pairs) = 6.99 Hz	$F_{\text{mechanical}} = 84.1 \div 10$ (pole pairs) = 8.41Hz
Speed = $60 \cdot 6.99 = 419$ rpm	Speed = $60 \cdot 8.41 = 505$ rpm
$K_v = 419 \text{ rpm} / 2.85 \text{ V} = 147 \text{ rpm/V}$ <i>(in SI units, $K_v = 15.4 \text{ rad/s/V}$)</i>	$K_v = 505 \text{ rpm} / 3.25 \text{ V} = 155 \text{ rpm/V}$ <i>(in SI units, $K_v = 16.2 \text{ rad/s/V}$)</i>
$K_t = 1 / 15.4 = 0.065 \text{ Nm/A}$	$K_t = 1 / 16.2 = 0.062 \text{ Nm/A}$
Max speed @ 48V = $48 \cdot 147 = 7056$ rpm	Max speed @ 48V = $48 \cdot 155 = 7440$ rpm
Max torque @ 300A = $300 \cdot 0.065 = 19.5 \text{ Nm}$	Max torque @ 300A = $300 \cdot 0.062 = 18.5 \text{ Nm}$

8.4.3 Discussion

Both motors proved to have fairly similar K_v (and hence K_t) values. In both cases it would be reasonable to expect a maximum RPM slightly over 7000 and a maximum torque just under 20Nm when used in a 48V system with a Kelly KBL48301 300A motor controller (as per UWA's previous Formula SAE Electric vehicle).

Experimentally-determined motor speed and torque constants correlate reasonably well with the theoretical approximations calculated in section 7.2.3, with about 15% variation.

Table 8.5: Comparison of actual motor constants with theoretical approximation

	Theoretical		Experimental		% difference
	K_v	K_t	K_v	K_t	
<i>Plettenberg Predator 37</i>	132rpm/V	0.072Nm/A	155rpm/V	0.062Nm/A	17%
<i>Turnigy CA120-70</i>	130rpm/V	0.073Nm/A	147rpm/V	0.065Nm/A	13%

The K_v value for the Plettenberg motor is not published, but the claimed K_v of 150 rpm/V for the Turnigy motor is very close to the experimentally-determined value of 147 rpm/V.

The waveforms of both motors appear to be quite close to sinusoidal, suggesting that optimum motor behaviour would be achieved using a motor controller with sinusoidal 3-phase output.

8.5 ADDING HALL SENSORS

As mentioned in section 7.1, all three motors under consideration were originally intended for use in electric aircraft, where there is no requirement for high starting torque, so are built for sensorless (i.e. back-EMF sensing) control. For traction purposes where starting torque requirement is high, it is necessary to add rotor position sensors for sensed control.

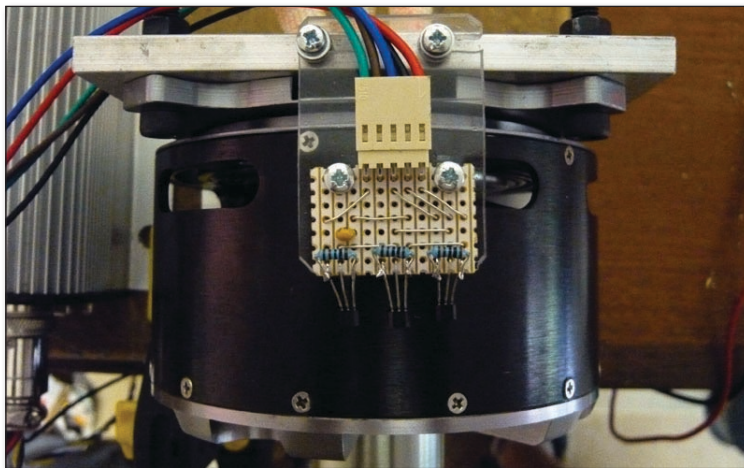
This type of modification has been undertaken by many hobbyists wishing to use inexpensive/commodity sensorless motors in traction applications (Endless Sphere: Electric Vehicle Technology Forums 2009).

Hall Effect sensors must be spaced 120° apart magnetically, i.e. three sensors spaced evenly over one pair of magnetic poles. Table 8.6 summarises sensor spacing calculation for the two 15kW motor candidates.

Table 8.6: Calculation of required Hall sensor spacing for each motor

	Plettenberg Predator 37	Turnigy CA120-70
Pole pairs	10 (20 magnets)	14 (28 magnets)
Rotor can diameter	103mm	118mm
Pole spacing	$103 \cdot \pi / 10 = 32.4\text{mm}$	$118 \cdot \pi / 14 = 26.6\text{mm}$
Hall spacing (120°)	$32.8 / 3 = 10.8\text{mm}$	$26.6 / 3 = 8.9\text{mm}$

For testing purposes, sensors were fastened to a small board and attached to the motor mounting frame. Figure 8.8 shows the result of the Hall sensor addition to the Turnigy motor.

*Figure 8.8: External Hall sensors added to Turnigy motor*

Optimal motor operating efficiency is depends on accurate spacing as well as timing (i.e angle with respect to stator windings). The sensor mounting brackets include slotted mounts so the timing can be adjusted $\pm 60^\circ$.

Correct behaviour of the Hall sensors is confirmed in section 7.6.

8.6 NO-LOAD TEST

8.6.1 Introduction

The safest place to start when testing any new motor is a no-load test. Smooth operation of the motor will confirm that the wiring is correct, and that the Hall sensor modification was successful.

The Hall sensor signalling and phase voltage waveforms can be observed using an oscilloscope to verify sensor timing and to check the compatibility of the motor controller with the motors.

8.6.2 Materials and Method

The two motors tested were the Plettenberg Predator 37 and Turnigy CA120-70. The power source used were two 12V deep cycle AGM batteries, for 24V total.

A Kelly KBL48301 motor controller was used, which is rated for 24-48V input voltage and had 300A maximum current. These controllers are designed to be compatible with any BLDC/PMSM motors that use 120°-spaced Hall sensors. Figure 8.9 shows a picture of the test setup.

Waveforms were monitored using an Atten ADS1102CAL 100Mhz digital storage oscilloscope.

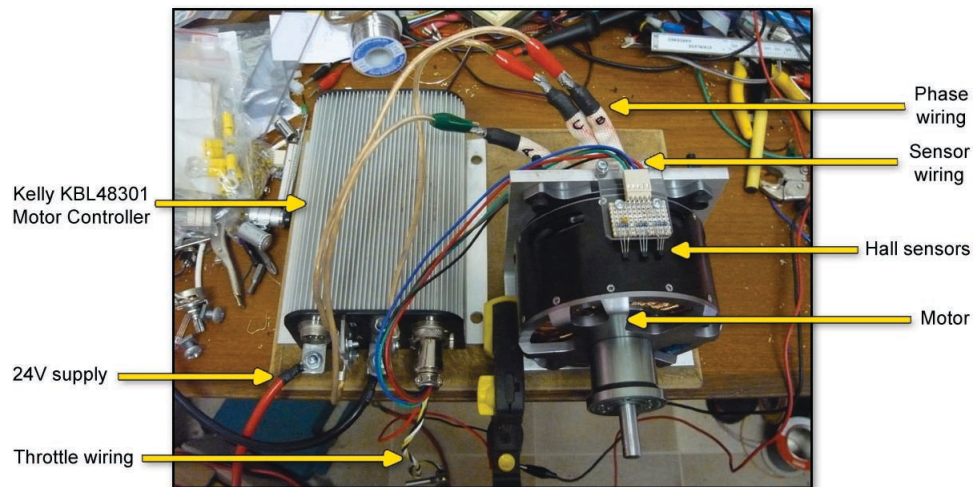


Figure 8.9: Test setup for no-load motor experiments

8.6.3 Results: Hall sensors

The following oscilloscope traces were observed when probes were attached to Hall sensors. Since the oscilloscope was only two channel, the three phases were observed as two pairs.

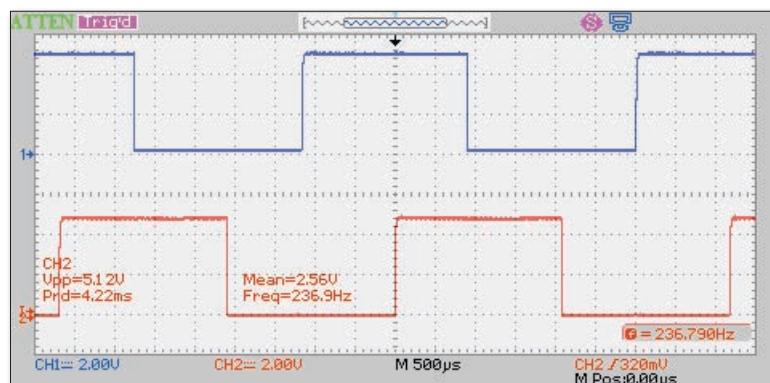


Figure 8.10: Oscilloscope capture of Hall sensors A (blue) and B (red)

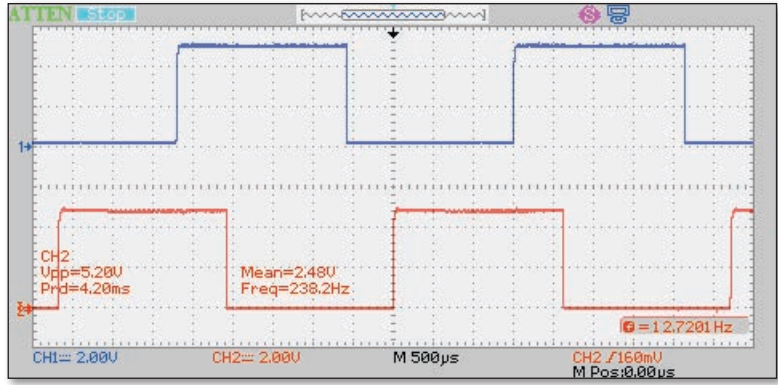


Figure 8.11: Oscilloscope capture of Hall sensors A (blue) and C (red)

8.6.4 Results: Phase Windings

The following oscilloscope traces were observed across one phase for the Plettenberg and Turnigy motors respectively:

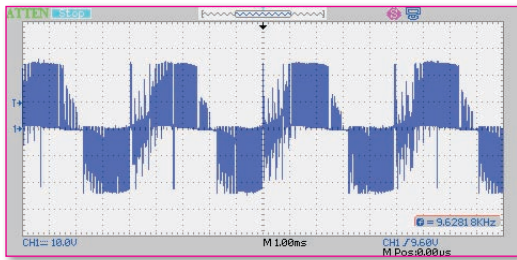


Figure 8.12: Plettenberg phase capture, 1ms/div

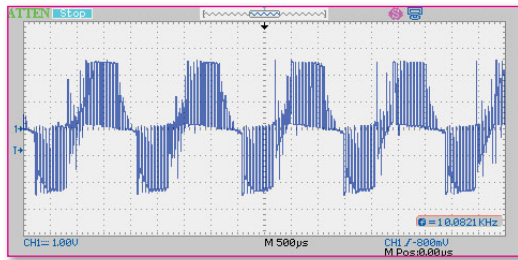


Figure 8.13: Turnigy phase capture, 500µs/div

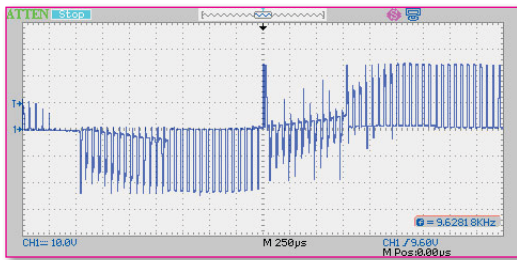


Figure 8.14: Plettenberg phase capture, 250µs/div

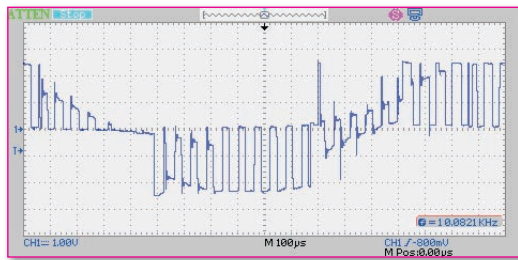


Figure 8.15: Turnigy phase capture, 100µs/div

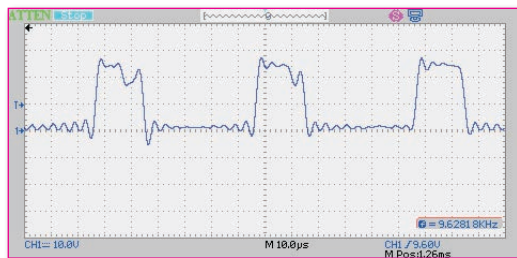


Figure 8.16: Plettenberg phase capture, 10us/div

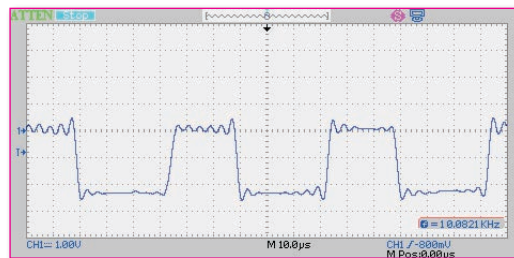


Figure 8.17: Turnigy phase capture, 10us/div

8.6.5 Discussion

Monitoring Hall sensor feedback while the motor was in operation confirmed clean switching (no false triggering) and correct timing of approximately 120° , confirming sensor spacing calculations.

It was observed that both the exact spacing and the overall position (timing) of the Hall sensors have a significant impact on smoothness of motor rotation – and hence presumably operating efficiency – which identified the need for further testing to quantify the effect of timing and find the optimum setting. The final design of sensor mounting used in a vehicle will need precise spacing and positioning.

The phase voltage captures show some interesting effects. Traces show a lot of unusual switching artefacts, most clearly visible in the middle figures. This may be attributed to some minor incompatibilities between motor and controller (such as low motor inductance causing problems for the controller's current limiting algorithm).

A significant amount of ripple is observed in the $10\mu\text{s}/\text{div}$ captures. This is often a side effect of a poorly designed motor controller, where internal inductances in the three-phase bridge cause 'ringing' (oscillations after each switch event).

The Kelly Controller appears to be doing trapezoidal switching (rather than sine-wave which was identified in section 7.4 as the most suitable for these motors) and probably no phase lag compensation (a shortcoming almost ubiquitous among the simpler trapezoidal BLDC controllers).

Although the motors both ran fairly well from the Kelly controller, the results from this experiment demonstrated that it would be beneficial to procure a motor controller which supported phase-lag-compensated sinusoidal 3-phase output.

8.7 FIXED LOAD TEST

8.7.1 Introduction

The motor velocity constant K_v calculated in section 7.4 can tell us a lot about the theoretical maximum speed and torque of the motor, but has little to offer in the way of predicting motor efficiency and continuous power ratings. For this, it is necessary to run the motor under load and measure its power use.

Basically in this experiment we wish to identify whether there are any significant efficiency differences which would preclude the use of the much cheaper Turnigy motor over the expensive Plettenberg.

In the absence of a full motor dynamometer, a large propeller was used as a fixed load. It is safe to assume that rotating a given propeller at a certain speed requires the same amount of energy regardless of the motor, so if one motor is using more energy to achieve the same speed, we can quantify a difference in operating efficiency.

8.7.2 Materials and Method

A similar setup was used to section 7.6, with a Kelly KBL48301 motor controller powered by two 12V lead acid batteries. Larger power cables were used throughout to handle the increased current expected. The load used was a 24x10" propeller attached to the motor output.

Power consumption by the motor was calculated via measured voltage and current from the batteries. Power losses in the motor controller were assumed to be negligible (Kelly claim typical 99% efficiency). Voltage was measured with a Fluke 179 multimeter, and current measured with Uni-T 400A DC clamp meter.

Speed sensing was done using the Atten ATS1102CAL oscilloscope, monitoring one Hall sensor's switching frequency as a multiple of the mechanical frequency (proportional to the number of pole pairs in the motor). Figure 8.18 presents a labelled diagram of the test rig.

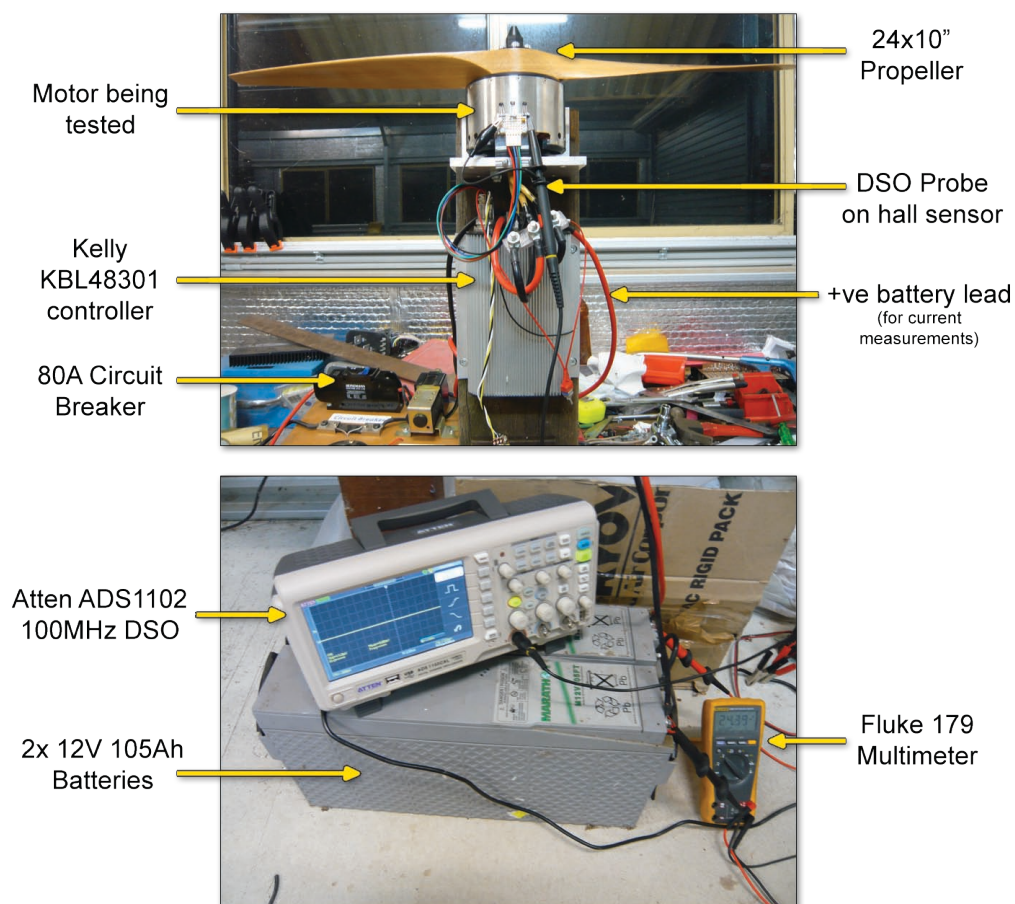


Figure 8.18: Overview of full power motor test rig

8.7.3 Results

The following table summarises the experimental data collected:

Table 8.7: Experimental data from comparative fixed-load motor test

Speed (rpm)	Plettenberg Predator 37			Turnigy CA120-70			Difference (%)
	Voltage (V)	Current (A)	Power (W)	Voltage (V)	Current (A)	Power (W)	
500	24.18	1.25	30.2	24.04	1.40	32.4	+7.3%
1000	24.07	2.98	71.7	23.92	3.18	76.1	+6.1%
1500	23.87	6.02	144	23.76	6.55	154	+6.9%
2000	23.72	10.3	244	23.6	11.25	265	+8.6%
2500	23.5	18.5	435	23.4	18.7	437	0.5%
3000	23.26	29.3	681.52	23.15	31.75	735	+7.9%

The Plettenberg proved to be more efficient with an average difference in efficiency of 6.2% was observed, although unfortunately experimental error appeared to be fairly significant. The data can be plotted graphically as follows:

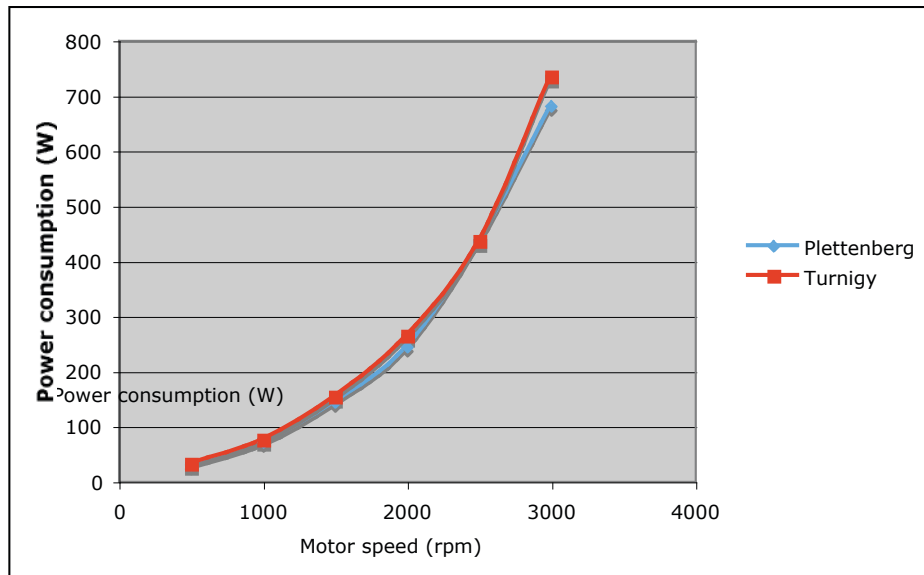


Figure 8.19: Power consumption vs speed for motors tested

8.7.4 Discussion

The Plettenberg motor was overall noticeably more efficient than the Turnigy, however during the test there was a troubling amount of experimental error and sensitivity of the apparatus. The motor controller's throttle sensitivity made it difficult to set the RPM within less than about 2% accuracy, and the importance of Hall sensor positioning and timing was reiterated. Sensor timing was adjusted to what seemed smoothest at a nominal ~1000rpm, but may have slightly affected results.

Overall it would be safe to conclude that the Plettenberg is a more efficient motor (though the actual percentage difference cannot be stated with confidence), but the difference in efficiency is hard to justify for the price.

8.8 EFFECTS OF HALL SENSOR TIMING

8.8.1 Introduction

As identified in section 7.6 and 7.7, the Hall sensor timing (relative angle of sensors to stator windings) can have a significant effect on motor behaviour and performance. Furthermore the inductance of motor windings tends to cause a phase lag between voltage and current in the motor varies proportionally with motor speed. In motor controllers which do not compensate for the phase lag automatically, the motor will run optimally at one speed and sub-optimally at all others. Therefore it is of value to quantify the range and sensitivity of a motor to changes in Hall sensor timing for various speeds.

In this experiment, we compare motor power usage at various speeds over a range of Hall sensor timings. Testing was performed on the Turnigy CA120-70 motor, but results could reasonably be extrapolated for any PMSM motors.

8.8.2 Materials and Method

The same test rig from section 7.7 was used. Only the Turnigy motor was tested, which has an 26.7mm magnetic pole pitch. Sensor timing measurements were taken at 1mm intervals, which therefore corresponds to 13.5° increments. Motor speed shown is mechanical RPM, though it was measured in electrical Hz by monitoring a Hall sensor signal with the oscilloscope.

8.8.3 Results

The following data was recorded:

Table 8.8: Experimental data from variable Hall Effect timing test

Timing (mm)	Motor current at speed (A)								
	500rpm 116Hz	750rpm 175Hz	1000rpm 233Hz	1250rpm 291Hz	1500rpm 350Hz	1750rpm 408Hz	2000rpm 467Hz	2250rpm 525Hz	2500rpm 583Hz
0	4.8	7.4	9.1	11.2	12.7	15.3	*	*	*
1	2.6	4.3	5.8	7.2	8.8	10.9	12.7	15.8	19.2
2	1.5	2.9	4.2	5.5	7.4	9.1	11.2	14.7	16.9
3	1.2	2.0	3.3	4.3	6.0	7.4	10.4	12.5	15.7
4	1.2	2.1	2.9	4.3	6.0	7.5	9.7	12.6	15.4
5	1.1	2.0	2.9	4.2	5.9	7.5	9.3	12.1	15.6
6	1.2	2.0	3.0	4.3	6.1	8.0	10.1	13.1	17.2
7	1.2	2.2	3.1	4.5	6.5	8.8	10.9	16.2	21.1
8	1.4	3.0	5.3	8.7	17.0	28.3	*	*	*

* Sample not taken to avoid possible damage to the motor – sensor timing was too extreme.

This can be represented graphically as follows:

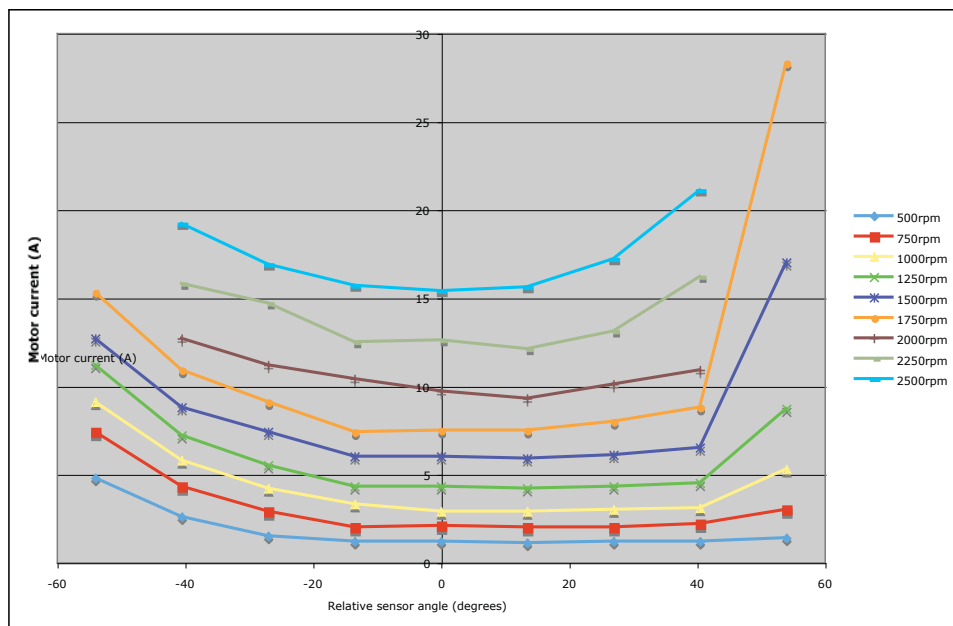


Figure 8.20: Effect of timing on current at various speeds

8.8.4 Discussion

The graph was centred around the data point at 5mm which had the lowest current draw at 2500rpm, representing the optimum sensor timing at this speed.

At low speeds, quite a wide band was observed for Hall sensor timing with little effect on motor speed; samples between -25° to $+40^{\circ}$ are almost identical. At higher speeds, timing appears to be increasingly important for efficiency (represented by increasing rate of curvature on the graph).

For higher speeds, $\pm 40^{\circ}$ sensor timing appeared to be the absolute maximum range where the motor would operate reliably. Particularly for cases of $>40^{\circ}$ retarded timing, motor performance was very poor.

Also discernible from the graph is the change in optimum timing at different RPMs. As one would expect, as speed increases the sensors need to switch earlier (known as advanced timing, in this case more negative positioning). Measurements are a little too coarse for a precise figure but a timing advance of approximately 10 degrees per 1000 rpm may be reasonable. As such, over the speed range of 0-7000rpm for this motor, the phase angle could change up to 70 degrees if fixed motor timing were used. This reiterates the importance of using a motor controller offering

automatic phase-lag compensation.

The high phase lag range for these motors can be attributed to the fact that they have very high pole count. At 7000rpm, the motors require an electrical frequency of 84kHz – much higher than most 3-phase motors.

8.9 CONCLUSION

Despite significant differences in motor geometry, our two motor candidates were found to have very similar speed and torque characteristics. Using a Kelly KBL48301 (48V 300A max) we could expect a maximum speed slightly over 7000rpm and a maximum torque just under 20Nm.

Adding Hall Effect sensors to the outside of the rotor can for rotor position sensing is feasible with both motors. Sensor spacing and position was found to be quite critical for optimum performance, so a final design would need rigid sensor mounting. Also the importance of accurate Hall sensor timing combined with a large phase lag variation (extrapolated) over the full RPM range of the motors means a motor controller with automatic phase-lag compensation would be highly recommended for best performance.

The continuous power rating of a motor is generally limited by the rate of heat build-up due to inefficiency vs rate of heat dissipation. Despite the much larger conductor size in the Turnigy, the Plettenberg was experimentally found to be more efficient – approximately 6% over the range of 0-3000rpm.

A surprising result considering the much larger conductor size in the Turnigy, and possibly attributable to the 40% higher electrical frequency required for a given RPM due to higher pole count, and the correspondingly higher eddy current losses.

Overall, the performance between the two motors was found to be sufficiently similar that use of the much cheaper Turnigy seems justified over the Plettenberg.

9 MECHANICAL DESIGN OF WHEEL HUB

9.1 INTRODUCTION

With a suitable motor identified, the next step was the mechanical design of the wheel hub.

The design has a variety of requirements which must be satisfied. Firstly it must adhere to all relevant Formula SAE rules and regulations. For example, all four wheels must have mechanical brakes which are capable of locking up the wheels. (Regenerative braking alone is not sufficient on any wheels.)

For neatness, the design must fit as completely as possible within the wheel hub itself. The wheels to be used were Keizer 4L 13x6" (see Appendix II). The design must be compatible with the suspension, which has already been designed and is discussed in more detail in section 9.2.

The drive system itself needs to be compact, efficient, reliable, and easy to construct and maintain. With a maximum motor speed of about 7000rpm, and a little over 1000rpm required at the wheels for 100km/h top speed, a reduction ratio of approximately 6:1 would be ideal. The reduction drive would need to cope with the ~20Nm maximum torque expected from the motor, at the motor controller's 300A maximum.

Based on these requirements, various options for reduction drive and component layout are considered. Finally a chosen design is verified and optimised using Finite Element Analysis.

9.2 SUSPENSION ATTACHMENTS

Suspension performance on a race car is very important, so its design was the thesis project of another student at UWA, Marcin Kiszko (2011). As is common with high performance vehicles, the design is based on an uneven-length double wishbone design with inboard suspension dampers actuated via pull-rods from the outer ends of the upper wishbone. Figure 9.1 shows a CAD rendering of the front left suspension.

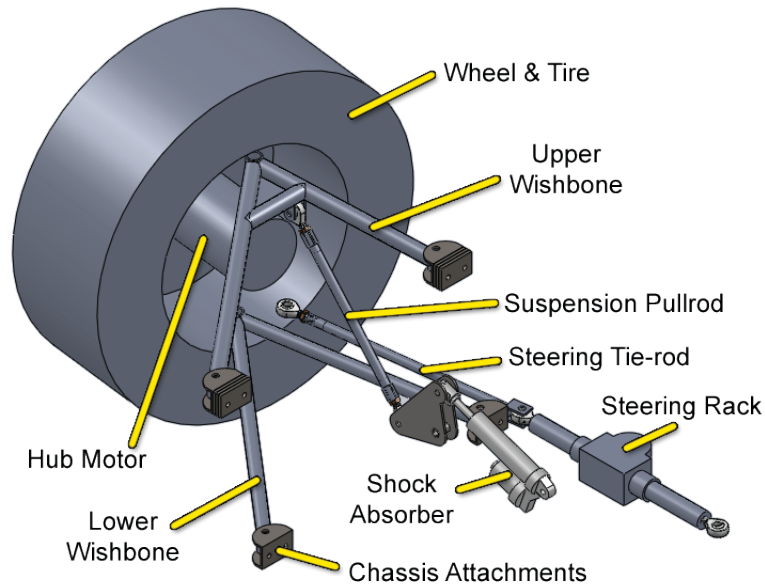


Figure 9.1: CAD rendering of front left suspension design, as designed by Marcin Kiszko (2011)

As can be seen on the diagram, the design of the upright must accommodate the location of three attachment points to the suspension – one each for the upper and lower wishbones, and in the case of the front wheels, one for the steering tie-rod. The rear suspension similarly uses three attachment points, but with the steering tie-rod replaced with a fixed brace to keep them pointing straight ahead. The locations of these points are summarised below:

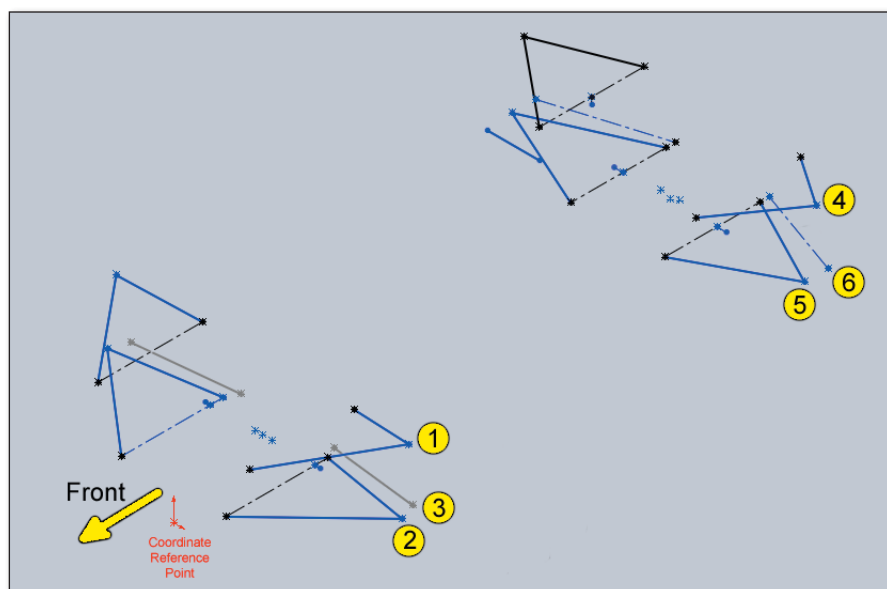


Figure 9.2: Suspension reference (Kiszko 2011)

The relevant suspension attachment points are summarised in Table 9.1.

Table 9.1: Suspension attachment coordinates

Reference		Coordinate (X Y Z mm)			Translated (X Y Z mm)		
(1)	Front upper	560	370	340	-70	+110	+15
(2)	Front lower	564	140	310	-74	-120	-15
(3)	Steering link	540	140	375	-90	-120	+50
	Middle of front wheel	630	260	325	0	0	0
(4)	Rear upper	560	380	1900	-40	120	0
(5)	Rear lower	560	150	1855	-40	-110	-45
(6)	Rear brace	560	150	1945	-40	-110	+45
	Middle of rear wheel	600	260	1900	0	0	0

Translated coordinates are referenced to the centre of the wheel, which is considered the middle of the wheel hub. Of particular note is the wider wheel track on the front wheels of 1260mm, which was required to avoid the wheel rims hitting the wishbones when turning (Kiszko 2011).

9.3 DRIVETRAIN COMPARISON

9.3.1 Introduction

The reduction drivetrain ideally needs a ratio of about 1:6, and must cope with 20Nm torque from the motor at up to 7000rpm. As identified by other researchers, the requirements for an in-wheel reduction drive are demanding (Gong et al 2008). A relatively large amount of power must be transmitted within a relatively small amount of space.

In this section several options are evaluated, namely belt drive, planetary gearbox, and pinion/spur gears.

9.3.2 Belt Drive

A belt drive reduction system was also investigated by Ivanescu (2009), and was based on a two-stage reduction system which ended up fairly complicated and bulky. A two-stage reduction has more moving parts, is harder to build, would have higher maintenance, and lower efficiency.

Alternatively we can consider if a single stage reduction is plausible. The first problem is that 5:1 is considered to be the practical limit of a single belt or chain drive (Patterson & Spée 1995), but it's not too far from the ideal 6:1 required here.

The inside diameter of the wheel rims is approximately 320mm, and motor diameter 120mm.

Allowing for a small amount of clearance, this leaves approximately 90mm between pulley centres, as shown in Figure 9.3.

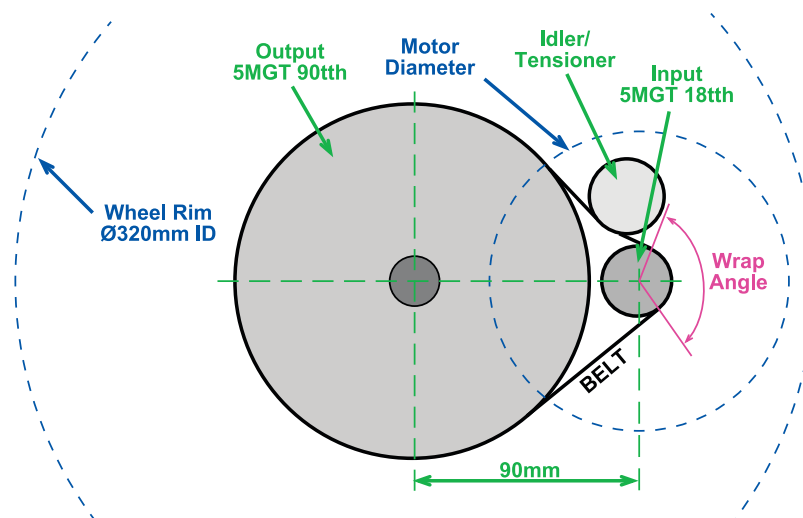


Figure 9.3: Space constraints make single-stage belt drive impractical due to inadequate wrap angle

Attaining the ideal ratio of 1:6 means drive pulley must be smaller than 13mm radius. As can be seen in Figure 9.3, a possible problem is the small wrap angle on the small drive pulley, which results in a very small contact area between pulley and belt which must cope with a large torque from the motor.

Communications with Phillip Aitken of Gates Transmissions Australia (2011) revealed the closest available product would be a toothed/timing belt 15mm wide in size “5MGT”. However due to the small wrap angle on the drive pulley, the belt could only handle 4.74Nm input torque which is far too low. And unfortunately drive pulleys of a sufficiently small diameter are not available to suit larger (stronger) belts. So in short, power density is the primary issue with belt drive systems, and a sufficiently strong drive will not fit within the wheel hub.

Further information/calculations on the belt drive system can be found in Appendix II.

9.3.3 Planetary Gearbox

Planetary gearboxes (also called epicyclic gearing) involve one or more outer gears known as *planet gears* rotating around a central *sun gear*.

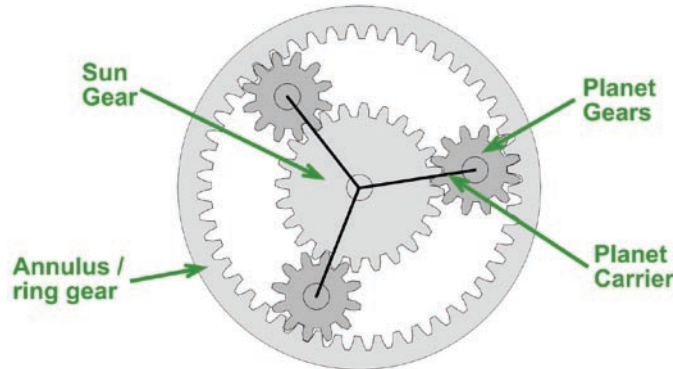


Figure 9.4: Diagram of a typical planetary gearbox

One of the primary advantages offered by planetary gearboxes is very high torque density, a consequence of having multiple gear meshes transmitting torque. For equivalent power rating, planetary gear sets are smaller, lighter and have lower inertia than spur gear pairs (Roos & Spiegelberg 2004). It is also possible to get fairly high reduction ratios in a single stage – certainly as high as 6:1 as required for this application.

The primary downside with planetary gearboxes is that their efficiency of around 97% is significantly lower than spur gears, once again a consequence of having multiple gear meshes. Cooling can be difficult due to their compact size and being enclosed by the annulus.

An in-wheel solution based on planetary gearbox was explored by Harris (2010), as discussed in section 5.4. In his research he identified a possible candidate for gearbox from manufacturer Matex, with a 5.5:1 reduction ratio (see Appendix II for full specifications). Officially this gearbox only has a 4000rpm rating which is significantly lower than required for this application, and would need a high flow rate of gear oil to keep gears lubricated and cool.

A significant issue with the use of a planetary gearbox for an in-wheel motor system is that the input and output are coaxial. This dictates the motor being on the opposite side of the wheel rim. Once wheel bearings and the planetary gearbox itself are included, the motor protrudes significantly outside the wheel rim.

Kiszko (2011) predicted the likelihood of suspension interference problems with this design, in particular the suspension pull rod.

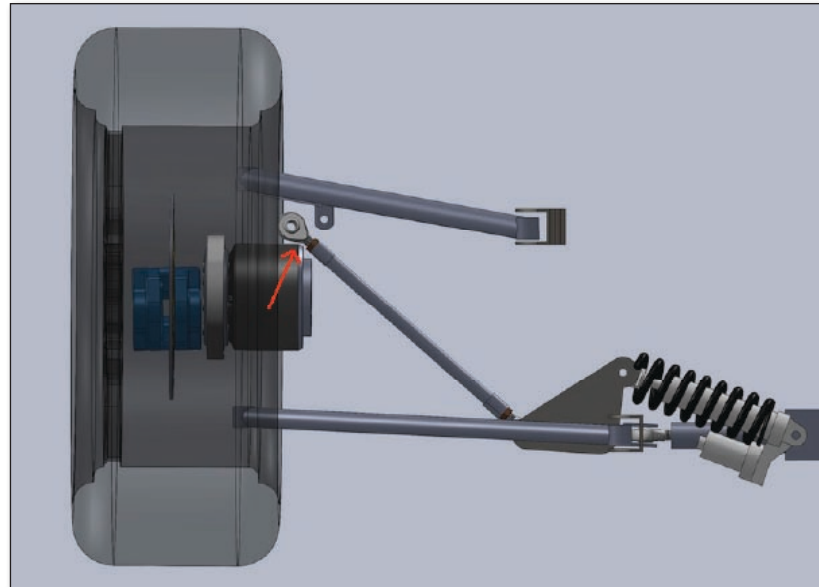


Figure 9.5: Possible suspension pull rod interference with planetary hub design (Kiszko 2011)

Kiszko's predictions were made prior to final component selection. Figure 9.6 shows scale drawings based on the actual motor and gearbox, demonstrating that the tolerances are indeed very tight. (Parts shown to scale are Keizer 4L 13x6 wheels, Turnigy CA12070 motor, Brembo 32G caliper, 7204 wheel bearings, Matex 120-5MNH, generic brake disc.)

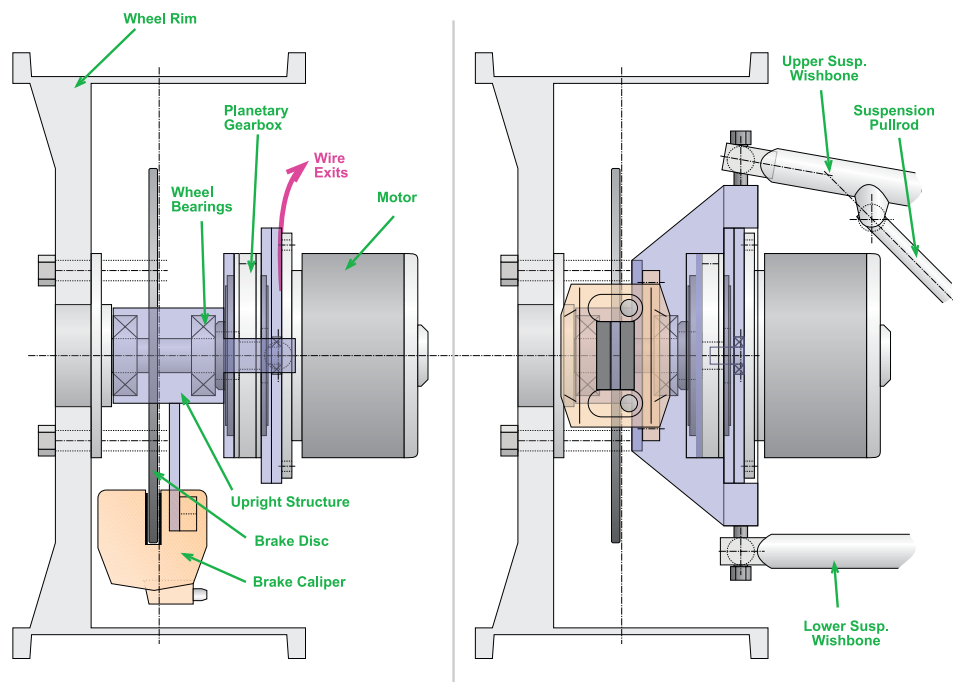


Figure 9.6: Top view (left) and front view (right) for hub layout based on planetary gearbox

Also the design presented by Kiszko is already compromising suspension performance slightly to accommodate the motor because the pull rod force vector intersects the upper wishbone some distance in from the end attachment, which causes a bending moment on the wishbone.

In conclusion, planetary gearboxes seem a feasible option but in this case we see clearance and heating issues, so it is good to seek a better solution.

9.3.4 Pinion and Spur Gears

Similar in principle to the gears used in manual gearboxes in most road-going vehicles, a pinion and spur gear reduction drive is generally considered the most efficient system for reduction drive. A further advantage in this case is that, unlike the planetary system where input is necessarily coaxial with output, the pinion/spur combination enables the motor to be positioned offset from the suspension such that interference with the suspension pull rod is no longer an issue.

Suitable gears were identified from supplier TEA Transmissions, pictured in Figure 9.7 next to the planetary gearbox.

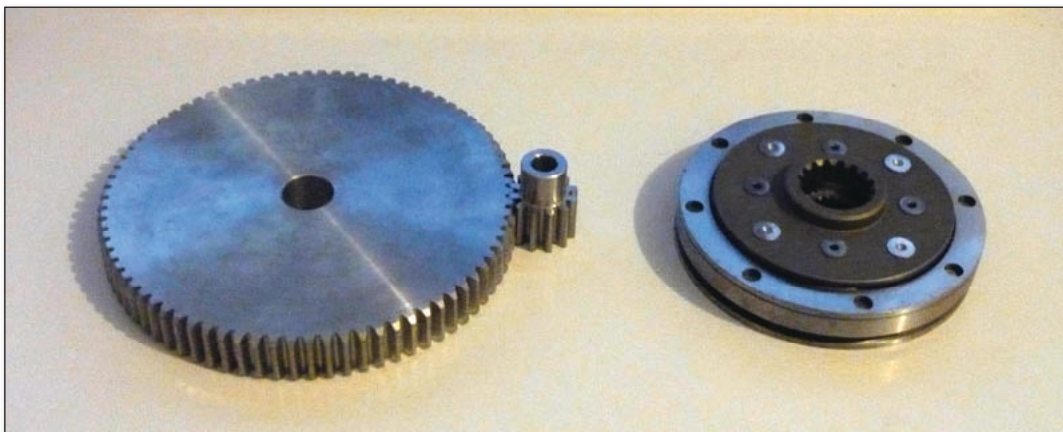


Figure 9.7: Picture of pinion/spur (TEA2080NH, TEA2012) and planetary gear set (Matex120-5MNH)

Table 9.2 compares specifications of the TEA pinion/spur combination compared with the Matex planetary gearbox.

Table 9.2: Pinion/spur vs Planetary gear set statistics

	Pinion/Spur	Planetary
Part Number(s)	TEA 2012, 2080NH	Matex 120-5MNH
Reduction Ratio	6.7:1	5:1
Performance estimate	100km/h max, 0.75G accel.	134km/h max, 0.55G accel.
Rated Torque	5Nm, up to 75Nm hardened	200Nm
Rated Input Speed*	16000rpm*	4000rpm
Estimated Efficiency	99%	97%
Weight	3.13kg	1.35kg

* based on 20m/s max gear mesh speed (TEA 2011) and typical lubrication/cooling

Performance predictions are based on the expected motor performance calculated in chapter 8, being 20Nm maximum torque and 7000rpm maximum speed. The higher reduction ratio offers more torque to the wheels but a lower maximum wheel speed. The expected maximum speed at Formula SAE events is around 100km/h, so speeds above this are unlikely to be utilised during the competition and it is preferable to have a the higher reduction ratio to maximise torque, and hence acceleration.

Due to having a single gear mesh instead of 8 for the planetary, the pinion/spur combination has much better efficiency. Most sources indicate a typical efficiency of 97% for planetary gear sets, vs 99% for straight-cut spur gears. A 2% difference in efficiency is not too significant from the perspective of vehicle performance, but it represents a factor of 3 more heat build-up in the transmission system which can be problematic.

In this application each transmission must cope with up to 15kW of power. A 97% efficient planetary system would therefore generate as much as 450W of heat, compared with 150W for a pinion/spur set. Compounded with the fact that planetary gear sets are also harder to cool due to their compact, enclosed design, the lower efficiency represents a significant disadvantage of planetary gear sets for hub motors.

Based on the gears selected, some possible hub layouts were explored as shown in Figure 9.10.

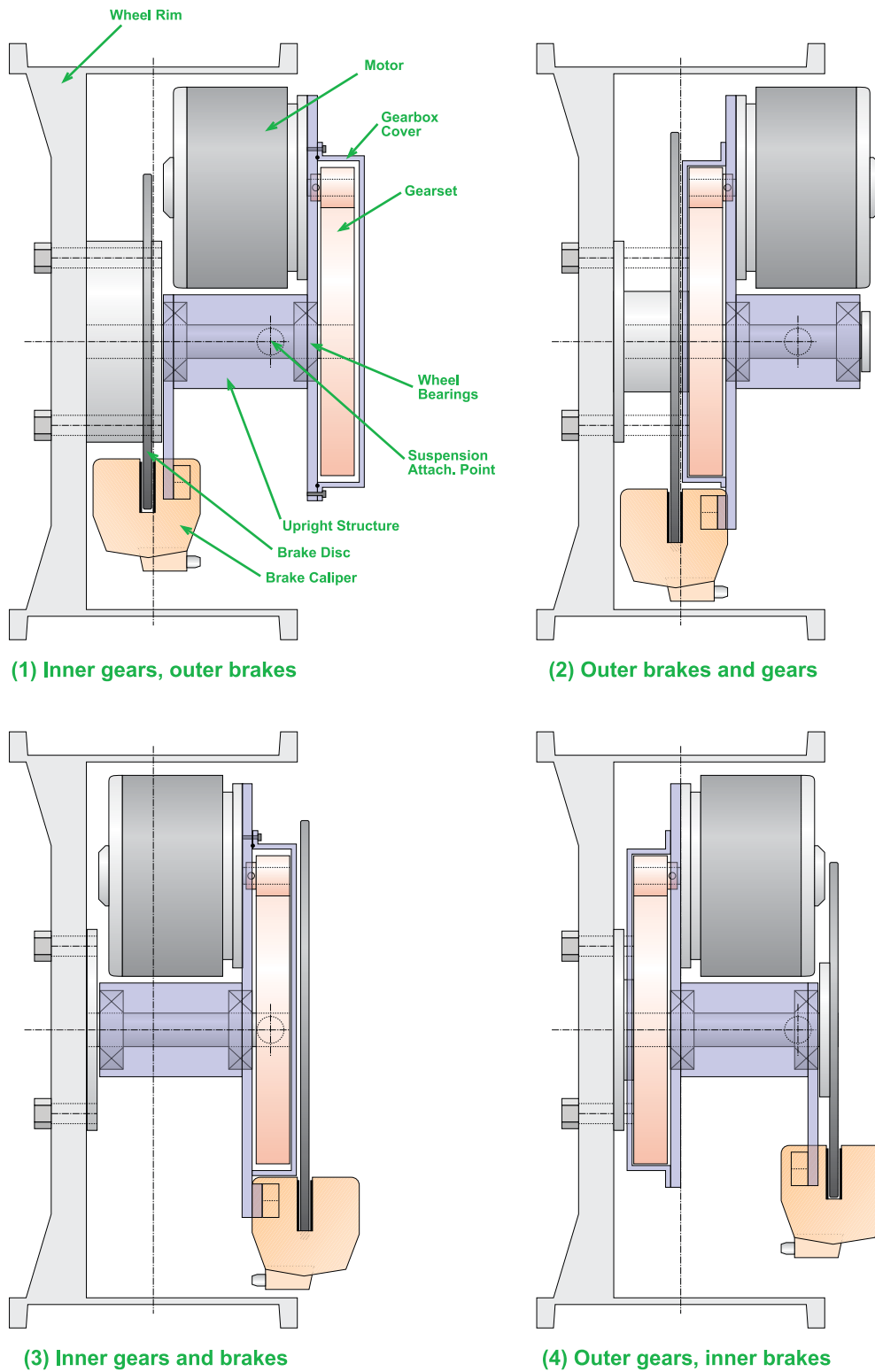


Figure 9.8: Four possible layouts (top-view) based on pinion/spur reduction gears

Parts shown (to scale) are Keizer 4L 13x6 wheels, Turnigy CA12070 motor, Brembo 32G caliper, 7204 wheel bearings, TEA 2080NH and 2012 gears, generic brake disc.

None of the designs proved to fit completely within the wheel hub, but all were close. A problem identified was the need to keep gears lubricated, with a strict avoidance of any lubrication escaping to the brake discs and compromising safety.

Some consideration was given to the possibility of running dry lubrication, in order to avoid a sealed gearbox. The two most common examples are Teflon (PTFE) or Molybdenum Disulfide (MoS₂) coatings. The latter can handle higher pressures and is sometimes suitable for dry lubrication of gears.

A maximum working pressure of 110kPa was identified for MoS₂ coatings (Holinski & Gansheimer 1970). Maximum pressure on pinion teeth, based on a contact area approximately 20x5mm conducting 20Nm of torque at 12mm radius, equates to 20MPa – more than two orders of magnitude too high. So the idea of dry lubrication was abandoned, and further investigation about necessary lubrication of high speed gears confirms that the only viable solution is an enclosed gearbox with circulating gear oil (Stachowiak & Batchelor 1993). This was a deciding factor in ruling out designs (2) and (3), due to the difficulty in guaranteeing no gear oil could escape to the adjacent brake disc.

Of the remaining choices, (1) was deemed a better option for two reasons. Firstly having the brake disc mounted directly next to the wheel rim would be safer; in the event of a shaft failure it would be better to lose drive than brakes. Secondly, having the spur gear on the outer side would mean only a single shaft oil seal, rather than requiring sealing on both sides.

9.4 PRELIMINARY CAD MODEL

After deciding on an overall layout for the in-wheel drive system, a preliminary design was completed in SolidWorks.



Figure 9.9: Preliminary hub design in SolidWorks

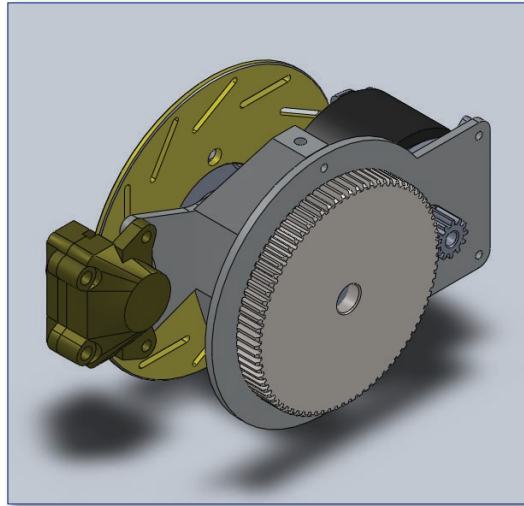


Figure 9.10: Close-up of design without wheel

9.5 DESIGN VERIFICATION AND OPTIMISATION

9.5.1 Introduction

Once a preliminary design has been developed, it is necessary to verify the strength of components under worst-case scenarios. It is also useful to explore opportunities to lighten any components which prove to be unnecessarily strong, in order to reduce unsprung mass.

Forces and loads on components can be calculated based on vehicle dimensions and dynamics, then compared to their ratings or, in the case of custom parts, Finite Element Analysis can be performed on each component in isolation based on the calculated forces. FEA analysis can calculate Von Mises stress concentrations in a part to discover any critical areas where the material may yield.

The process of optimising components for vehicles is not an exact science because the wide range of conditions they may experience cannot be fully predicted, but we can consider some “worst case scenarios” to gain a reasonable estimation on design integrity.

9.5.2 Verification of Wheel Bearing Load Rating

The SKF 7204BECBP tapered-race ball bearings chosen for the wheel bearings have a dynamic radial load rating of 14.3kN (SKF 2011). The maximum load experienced by wheel bearings is in the outer bearing of the outer wheel during cornering, and is a combination of vehicle weight plus opposing forces balancing the moment from the wheel contact radius, as shown in Figure 9.11. The maximum cornering acceleration is taken as 1.5G, resulting in an outer wheel load of 125kg due to load transfer (see Appendix II).

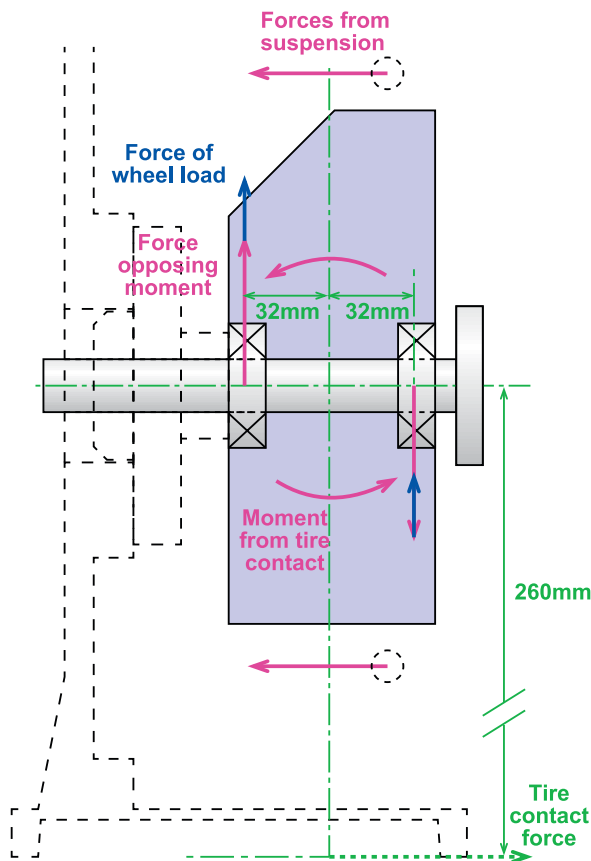


Figure 9.11: Diagram of forces on wheel bearings

Force calculations:

Force due to weight loading:

$$F_w = 125 \cdot 9.81 \div 2 = 613 \text{ N}$$

Force at tire contact point:

$$F_t = 125 \cdot 9.81 \cdot 1.5 = 1840 \text{ N}$$

Moment about bearings due to tire force:

$$\omega = F_t \cdot 0.26 = 478 \text{ Nm}$$

Force on bearings opposing moment from tire contact point:

$$F_m = 478 \div 0.032 \div 2 = 7468 \text{ N}$$

Total force on outer wheel bearing:

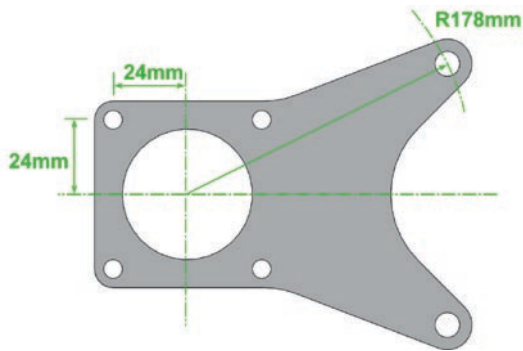
$$F_{\text{total}} = F_w + F_m = 8081 \text{ N}$$

Maximum load on wheel bearings is calculated to be 8081N, representing a safety factor of 1.73 compared with their rated load.

9.5.3 Brake Caliper Mount Strength Verification

The mounting bracket for the brake caliper needs to be strong enough to resist all braking forces between the brake rotor and caliper. The worse case scenario for the brake caliper mount is seen at the front wheels under maximum braking. Each tire of 0.26m radius sees a load of 125kg at 1.5G

deceleration (see Appendix II for load transfer calculations), hence:



Force at tire contact patch:

$$F = ma = 125 \cdot 9.81 \cdot 1.5 = 1840 \text{ N}$$

Torque at wheel hub:

$$T = 1840 \cdot 0.26 = 478 \text{ Nm}$$

Force on caliper mounts:

$$F = 478 / 0.178 / 2 = 1343 \text{ N}$$

Figure 9.12: Drawing of caliper mounting bracket

Using the four 6mm upright mounting holes as fixtures and applying a force of 1343N to each of the two caliper mounting holes yields the following Von Mises stress simulation:

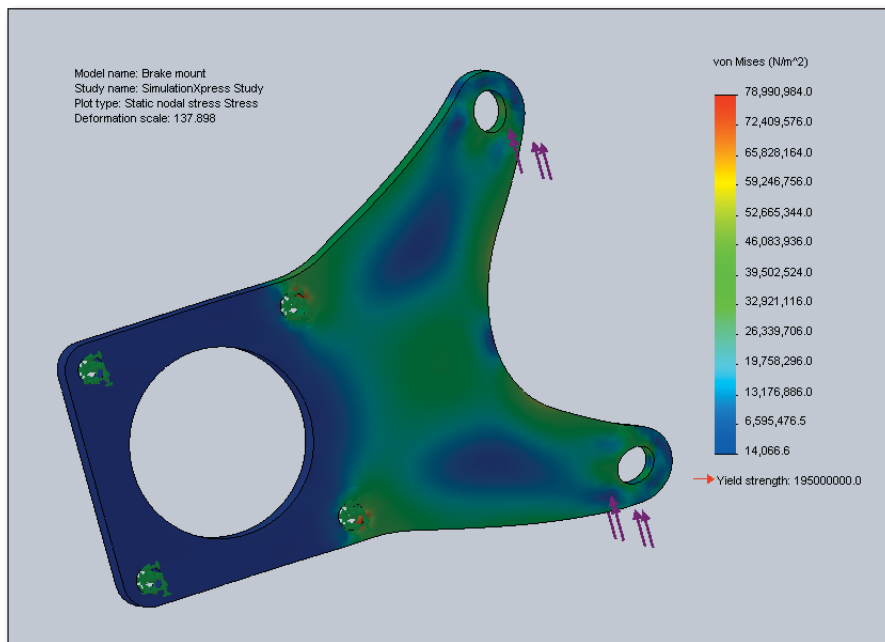


Figure 9.13: Von Mises analysis of brake caliper mounting bracket

A safety factor of approximately 5:1 is observed. Lightening the part without compromising function may be possible, but the part itself is relatively low weight so it is deemed unnecessary.

9.5.4 Upright Body Lightening and Verification

The primary option for weight reduction in the upright body itself is the excess material between wheel bearing housing and the suspension mounts at the extremities. The easiest option is to hollow the section out as shown in Figure 9.14. The resulting hollow triangular shape should resist longitudinal deflection.

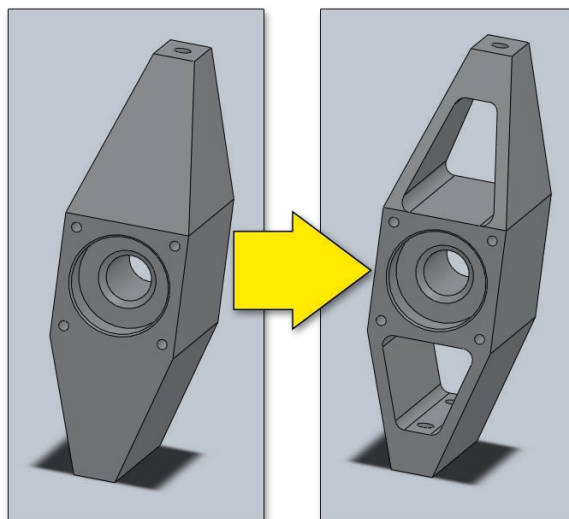
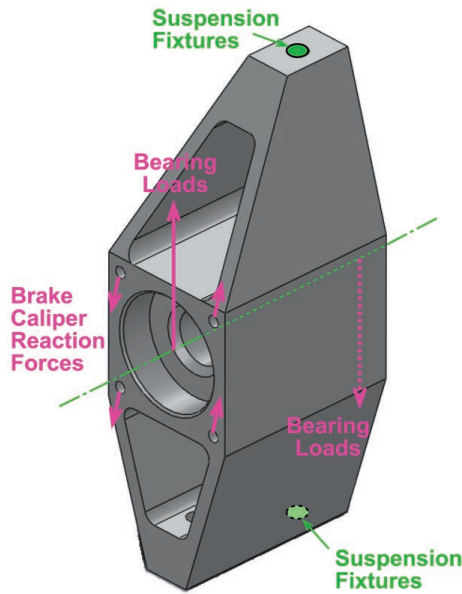


Figure 9.14: Lightening of the upright body

The worst case scenario for stresses on the upright are during maximum cornering and braking, where the front outer wheel may be taking entire vehicle weight (e.g dynamic load transfer may cause this temporarily). If the suspension attachment points are considered rigid fixtures, the forces on the upright come from bearing loads (as calculated in section 8.5.2) and brake caliper forces. Based on FEA simulation of caliper mount, the majority of stress is seen at the mounting bolts closest to the caliper, with virtually none transmitted to the farther mounting bolts. Figure 9.15 shows the position of these forces.



Outer bearing reaction force:

$$F_{ob} = 7468 + 613 = 8081\text{N (up)}$$

Inner bearing reaction force:

$$F_{ib} = 7468 - 613 = 6855\text{N (down)}$$

Force at tire contact patch:

$$F = ma = 300 \cdot 9.81 \cdot 1.5 = 4414\text{ N}$$

Torque at wheel hub:

$$T = 4414 \cdot 0.26 = 1147\text{ Nm}$$

Force on caliper bracket mounts:

$$F = 1147 / 0.034 / 2 = 16860\text{N}$$

Figure 9.15: Forces experienced by upright body

Simulation based on these load calculations yielded the following results:

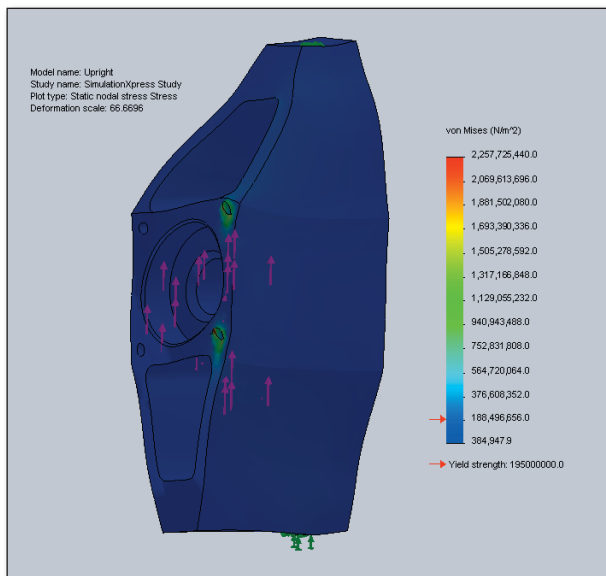


Figure 9.16: Von Mises stresses on upright

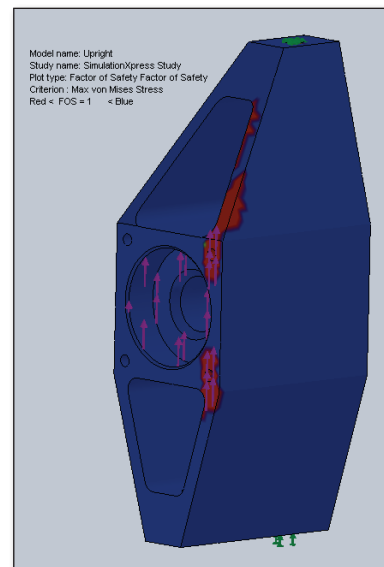


Figure 9.17: Highlighted areas where safety factor < 1 (material failure)

Basically stresses on all parts of the upright are negligible with stark exception to the mounting bolts nearest the caliper, which would yield severely. As such it will be necessary to reinforce the brake caliper mount – most likely by welding its edges to the upright body, to spread out the stresses from brake caliper reaction forces.

The low stress concentrations throughout the rest of the component suggest that more material could be removed if further weight saving is desired.

9.5.5 Optimisation of Spur Gear

The steel spur gear has a mass of approximately 3kgs, which is a considerable addition to the total hub mass. It is possible to reduce the weight of the gear by removing “inactive” material, such as between the axle mounting and the teeth. Stress concentrations in gears tend to be highest at the teeth, and secondly at the attachment to the shaft such as through a spline or keyway.

The TEA2080 gear was modelled in SolidWorks as shown in Figure 9.18, with the only modification being the six mounting bolt holes.

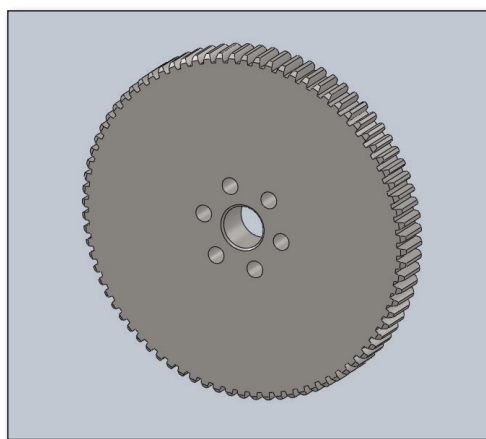


Figure 9.18: SolidWorks model of unmodified gear

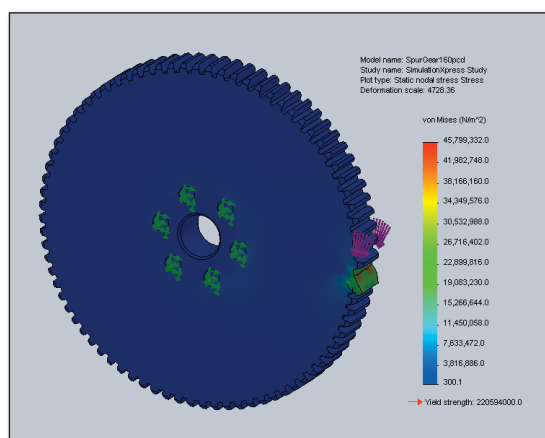


Figure 9.19: Von Mises analysis of unmodified gear

Figure 9.19 graphically shows the Von Mises stress concentrations on the material under worst case scenario of 20Nm torque being transmitted to a single tooth on the spur gear from the 24mm PCD gear, resulting in a 1666N force on the tooth. A maximum stress around 46MN/m² is observed, representing a safety factor of around 5, against the yield strength of 220MN/m² for plain carbon steel.

However it is clear from the analysis that the vast majority of the steel is virtually unstressed, indicating that a lot can be removed without compromising the component’s integrity. A proposed design for a lightened spur gear is shown in Figure 9.20.

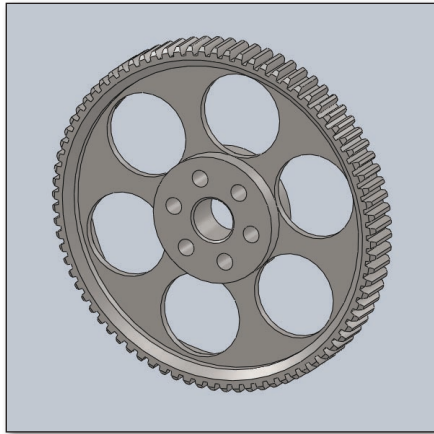


Figure 9.20: Design of lightened gear

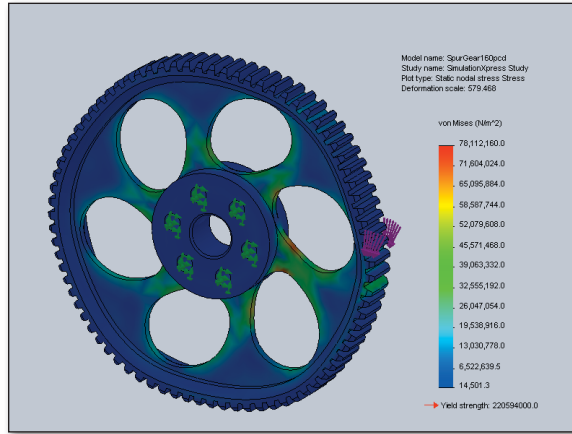


Figure 9.21: Von Mises analysis of lightened gear

Figure 9.21 shows the Von Mises stress concentrations for the new design, again under worst case scenario with maximum motor torque of 20Nm from the motor. The highest stress concentration in this design is now found at the thinnest point of the “spokes”, with a value of 78MN/m², with a safety factor of 2.8. The mass of the lightened spur gear was calculated by SolidWorks to be 1.12kg, down from 3.03kg for the unmodified gear, a saving of almost 2kg.

9.5.6 Final Design

Figure 9.22 shows an exploded view of the wheel hub assembly.

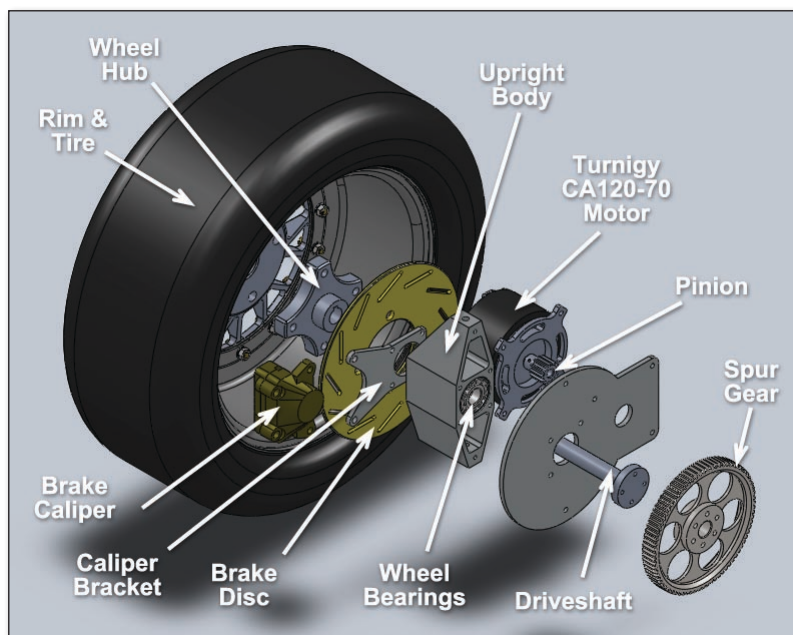


Figure 9.22: Exploded view of wheel hub assembly

Table 9.3: Summary of components in hub design

Part	Description	Mass (kg)
Motor	Turnigy CA120-70	2.61
Pinion	TEA 2012	0.08
Spur Gear	TEA 2080NH	1.12
Motor mount	6mm Aluminium, laser cut	0.57
Drive system subtotal:		4.38
Upright Body	Aluminium, CNC machined	0.96
Wheel bearings x2	SKF 7204	0.10
Driveshaft	4140 steel, CNC machined	0.55
Caliper bracket	6mm Aluminium, laser cut	0.09
Brake caliper	Brembo 32G	0.54
Brake rotor	Ø220x5mm steel	1.15
Wheel hub	Aluminium, CNC machined	0.45
TOTAL:		9.03 *

** excluding wheel rim and tire*

9.6 SUMMARY

This chapter has described the design of an in-wheel drive system based on high-speed PMSM motor. The design is compatible with the suspension geometry designed by Kiszko (2011), and to the best of the author's knowledge, complies with all Formula SAE rules. It was also designed to accommodate a Brembo 32G brake caliper with Ø220x5mm brake disc, and fit inside a Keizer 4L 13x7 wheel (see Appendix II for more details of these components).

Various options for reduction drive were reviewed, namely belt drive, planetary gearbox, or pinion/spur gear. The latter was chosen due to high efficiency, fairly compact size, and convenient layout in the hub.

With a 6.6:1 reduction drive to the wheel, a peak torque of 132Nm and maximum speed of 1060rpm (100km/h) is expected from the design, which satisfied the application requirements for a Formula SAE race car identified in chapter 3, being 108Nm peak torque and 1060rpm.

Components were evaluated using Finite Element Analysis to verify strength and lighten where possible. The total weight excluding wheel and tire is approximately 9kg, with 4.4kg for the drivetrain.

10 CONCLUSION

This thesis has explored the design of in-wheel motor systems for Formula SAE Electric vehicles. Electric vehicles are rapidly increasing in popularity and many automobile manufacturers have already released electric vehicles. There is also growing interest from universities around the world in the building electric vehicles for the Formula SAE competition. A review of these indicates that conventional drivetrains are the norm to date, which highlights the potential for researching in-wheel drive systems for both of these vehicle types.

The performance requirements for in-wheel drive systems for both vehicle types were calculated. In brief, maximum wheel speed in both cases is about 1000rpm. Roadgoing vehicles require a maximum torque of 332Nm, for steep hill-climbing. Formula SAE electric vehicles require much less torque, being much lighter vehicles and also only operating on a flat race track, with a peak torque of 108Nm required. Some qualitative requirements were also discussed, such as the need for fully enclosed, water cooled motors to operate in the dirty environment of a wheel hub – for road-going vehicles are least, where distances are high, maintenance intervals long, and conditions unpredictable.

After reviewing fundamental motor and controller theory, a review of academic literature and commercial products relating to in-wheel motor systems was presented. Permanent Magnet Synchronous Motors (PMSMs) were almost ubiquitously considered the most promising candidate due to their very high power density and efficiency. Two main topologies were encountered, namely axial flux PMSM and outer-rotor radial flux. However it became clear that achieving sufficient torque was one of the most challenging requirements for in-wheel motor systems. This led to the selection of two paths for further research. Firstly the design of a direct drive wheel motor based on axial-flux PMSM, with dual rotor and airgap winding, and secondly a system based on a commercial high-speed PMSM motor with reduction drive to the wheel.

The direct drive case was explored first. Initially some magnetostatic Finite Element Analysis experiments were undertaken in Ansys Maxwell SV in order to optimise machine dimensions. It was found that nominal dimensions for an axial flux airgap-stator include a backplate thickness approximately equal to magnet thickness (to minimise leakage flux), an airgap thickness of 1-2x magnet thickness for reasonable airgap flux density, and a pole span to airgap width of at least 3 to keep inter-pole leakage low. Also the efficacy of Halbach Arrays in increasing airgap flux density was demonstrated.

Combined with the constraints of the application discussed in the requirements analysis, this led to

the design of a 24-pole motor, Ø300mm x 44mm in size. Unfortunately torque estimates of 12Nm continuous and 36Nm maximum were significantly lower than required for this application.

Since a direct drive system appeared inadequate, a reduction drive system was explored. Some motor candidates had been identified, all based on outer-rotor PMSM vernier drive (LRK) topologies and originally intended for electric aircraft use, where power density is equally paramount. The motors were submitted to a variety of tests to evaluate their suitability.

Once a motor was chosen, the mechanical design of the wheel hub was undertaken. A reduction drive of 6.6:1 based on pinion/spur gears was chosen, yielding a predicted maximum torque at the wheel of 132Nm and top speed of 1060rpm (100km/h) which satisfies the application requirements, and packaged into a design including disc brakes which fits within a common 13x6" wheel.

Comparing the two systems, the direct drive is certainly preferable from the perspective of simplicity and reliability, and would be suitable for applications requiring (much) less torque. It also avoids any transmission losses. However unfortunately it proved difficult to design for sufficient torque, which precludes its use in this case. Furthermore it ended up substantially heavier at 10.4kg than the reduction drive solution at 4.4kg for the drivetrain components, which adds unwelcome unsprung mass.

Two possible ideas have since emerged for future research. Firstly, the motor could be designed for a much lower K_v (and higher K_t) by using thinner conductors, such as using four "windings" of Ø3mm conductors instead of one Ø6mm conductor per pole. This raises torque per amp by four, though decreases conductor size by the same factor. Most importantly however, resistive losses are proportional to the square of the current, so resistive heating should be reduced in a higher-voltage design.

Another idea for further research would be along the lines of Carrichi (1996) and Pullen & Mansir (1999) who used a multi-stage axial flux to increase torque. The design could be extended with more layers of rotor & stator, which should increase torque proportionally. A combination of these two improvements may yield a motor with sufficient torque.

It is envisaged that other Formula SAE teams will consider the use of in-wheel drive systems in the future. Based on findings in this research, a high speed motor with reduction drive is recommended as the easier solution.

11 REFERENCES

- Adams, W 1884, *Electric Motor*; US Patent 300827
- Ando, N & Fujimoto, H 2010, 'Yaw-rate Control for Electric Vehicle with Active Front/Rear Steering and Driving/Braking Force Distribution of Rear Wheels', *11th IEEE International Workshop on Advanced Motion Control*. 21-24 March 2010, Nagaoka, Japan.
- Astroflight Brushless 150 Motor. Available from <www.astroflight.com>
- Batzel, T & Lee, K 2005, 'Electric Propulsion with the Sensorless Permanent Magnet Synchronous Motor', *IEEE Transactions on Energy Conversion*, Vol. 20, No. 4, pp 575-583 (*Implementation and Performance*) & 818-825 (*Model and Approach*)
- Brand, S, Ertugrul, N & Soong, W 2004, 'Investigation of an Electric Assisted Bicycle and Determination of Performance Characteristics', *Australasian Universities Power Engineering Conference (AUPEC04)*, Christchurch.
- Brisset, S, Tudorache, T, Tran, T, Brochet, P & Fireteanu, V 2007, 'Finite Element Analysis of a Brushless DC Wheel Motor with Concentrated Winding', *International Aegean Conference on Electrical Machines and Power Electronics, ACEMP'07*, pp. 337-342
- Brooke, L 2010, 'Protean Electric courts partners for wheel motor applications', *Automotive Engineering International Online*. <<http://www.sae.org/mags/aei/8458>>
- Cairns, E, 'A new mandate for energy conversion: zero emission (electric) vehicles', *IEEE 35th International Power Sources Symposium*, pp 310-313
- Cakir, K 2004, *In-Wheel Motor Design for Electric Vehicles*. Masters Thesis, Sabanci University, Istanbul.
- Cakir, K & Sabanovic, A 2006, 'In-wheel motor design for electric vehicles', 9th IEEE International Workshop on Advanced Motion Control
- Caricchi, F, Crescimbeni, F, Mezzetti, F & Santini, E 1996, 'Multistage Axial-Flux PM Machine for Wheel Direct Drive', *IEEE Transactions on Industry Applications*, Vol. 32, No. 4, pp 882-888
- Chan, C & Wong, Y 2004, 'The state of the art of electric vehicle technology', *4th International Power Electronics and Motion Control Conference, IPEMC2004*, Vol. 1, pp 46-57
- Chang, L 2004, 'Comparison of AC drives for electric vehicles – A report on experts' opinion survey', *IEEE Aerospace and Electronic Systems Magazine*, Vol. 9, issue 8, pp 7-11.
- Chen, C & Cheng, M 2006, 'A New Sensorless Commutation Drive for Brushless DC Motors

and Alternators', *IEEE International Symposium on Industrial Electronics 2006*, vol. 3, 2116-2121

- Cheng, Y, Duan, F & Cui, S 2005, 'The Design Principle of Electric Motors and Drive Systems for Electric Vehicles', *Proceedings of the 8th International Conference on Electrical Machines and Systems, ICEMS2005*. Vol. 1, pp. 802-805
- Chung, M 2008, 'Development of In-Wheel Motor System using Brushless DC Motor of Hall sensor Type', *International Conference on Control, Automation and Systems, Seoul, Korea*
- Clarke, R 2008a, 'Magnetic properties of materials'. Available from <<http://info.ee.surrey.ac.uk/Workshop/advice/coils/mu>>
- Clarke, R 2008b, 'Power losses in wound components'. Available from <http://info.ee.surrey.ac.uk/Workshop/advice/coils/power_loss.html>
- Colton, S 2010, *Design and Prototyping Methods for Brushless Motors and Motor Control*, Masters Thesis, Massachusetts Institute of Technology.
- Dixon, L.D 2003, *Eddy Current Losses in Transformer Windings and Circuit Wiring*. Texas Instruments.
- e-Traction Direct Drive Technology: *TheWheel*. Available from <<http://www.e-traction.com/TheWheel.htm>> [17 April 2011]
- Ehsani, M, Rahman, K & Toliyat, H 1997, 'Propulsion system design of electric and hybrid vehicles', *IEEE Transactions on Industrial Electronics*, Vol. 44, Issue 1, pp. 19-27
- Endless Sphere: Electric Vehicle Technology Forums 2009. *Mounting Hall sensors to R/C brushless motors*. Available from: <<http://endless-sphere.com/forums/viewtopic.php?f=28&t=9061>>. [17 August 2009].
- Espanet, C, Kauffmann, J & Bernard, R 2006, 'Comparison of Two In-Wheel Permanent Magnet Motors for Military Applications', Vehicle Power and Propulsion Conference, IEEE.
- *Formula Student Electric Rules 2011*, Formula Student, Germany.
- Gong, H, Chai, F, Pei, Y & Cheng, S 2008, 'Research on Torque Performance for Permanent Magnet In-Wheel Motor', *IEEE Vehicle Power and Propulsion Conference VPPC2008*, Harbin, China
- Greaves, M, Simpson, A, Guymer, B, Walker, G & Finn, A 2003, 'Ironless wheel motor for a direct drive vehicle application'. *Proceedings of the Australasian Universities Power Engineering Conference*. Christchurch, New Zealand, pp 1-6.

- Greaves, M, Walker, G & Walsh, B 2001, 'Design optimisation of Ironless Motors based on Magnet selection', *Proceedings of the Australasian University Power Engineering Conference*. Perth, Australia, pp 216-220.
- Green Team: Rennwagen. Available from < <http://www.greenteam-stuttgart.de/Rennwagen.html> >
- Güemes, J, Iraolagoitia, A, Donsión, M & Hoyo, J 2008, 'Analysis of Torque in Permanent Magnet Synchronous Motors with Fractional Slot Windings', *Proceedings of the 2008 International Conference on Electrical Machines*
- Hacker Brushless Motors. Available from <<http://www.hacker-motor.com>>
- Halkosaari, T 2006, 'Optimal U/F control of high speed permanent magnet motors', *Proceedings of the IEEE International Symposium on Industrial Electronics*, Montreal, Vol. 3, pp 2302-2308
- Harris, D 2010, *REV SAE Front Drive*. Undergraduate thesis, University of Western Australia.
- Hredzak, B, Gair, S & Eastham, J 1996, 'Elimination of Torque Pulsations in a Direct Drive EV Wheel Motor', *IEEE Transactions on Magnetics*, Vol. 32, No. 5, pp 5010-5012
- Holinski, R & Gansheimer, J 1970, *A study of the lubricating mechanism of molybdenum disulphide*. Dow Corning, Munich, Germany.
- Hui, T, Basu, K & Subbiah, V 2003, 'Permanent magnet brushless motor control techniques', *Proceedings of Power Engineering Conference, PECon 2003*
- Ishizaki, A et al 1995, 'Theory and Optimum Design of PM Vernier Motor', *Seventh International Conference on Electrical Machines and Drives (Conf. Publ. No. 412)*
- Ivanescu, M 2009, *Design of the Drive System and Battery Cage for the 2009 REV FSAE vehicle*. Undergraduate thesis, University of Western Australia.
- Jian, Z, Xuhui, W & Lili, Z 2009, 'Optimal system efficiency operation of dual PMSM motor drive for fuel cell vehicles propulsion', *IEEE 6th International Power Electronics and Motion Control Conference*, pp. 1889-1892
- Kim, J & Kim, H 2007, 'Electric Vehicle Yaw Rate Control using Independent In-Wheel Motor'. *Power Conversion Conference, PCC '07, Nagoya*. pp 705-710
- Kim, YK, Cho, YH, Park, NC & Mok, HS 2009, 'In-Wheel motor drive system using 2-phase PMSM', *Power Electronics and Motion Control Conference '09*, pp. 1875-1879

- Kiszko, M 2011, *REV 2011 Formula SAE Electric – Suspension Design*. Undergraduate thesis, University of Western Australia.
- Laine, L & Fredriksson, J 2007, ‘Coordination of Vehicle Motion and Energy Management Control Systems for Wheel Motor Driven Vehicles’, *Proceedings of the 2007 IEEE Intelligent Vehicles Symposium*, Istanbul, Turkey, pp 773-780
- Laskaris, K & Kladas, A 2008, ‘High Torque Internal Permanent Magnet Wheel Motor for Electric Traction Applications’, *18th International Conference on Electrical Machines*, pp 1-4
- Laskaris, K & Kladas, A 2010, ‘Internal Permanent Magnet Motor Design for Electric Vehicle Drive’, *IEEE Transactions on Industrial Electronics*, Vol. 57, Issue 1, pp 138-145.
- Lee, C.H 1963, ‘Vernier Motor and Its Design’, *IEEE Transactions on Power Apparatus and Systems*, vol. 82, pp. 343-349.
- Lee, K, Son, H & Joni, J 2005, ‘Concept Development and Design of a Spherical Wheel Motor (SWM)’, *Proceedings of the 2005 IEEE International Conference on Robotics and Automation*, Barcelona, pp 3652-3657
- Li-qiang, J, Chuan-xue, S & Qing-nian, W 2010, ‘Influence of In-Wheel Motor Structure about the Contact and Comfort for Electric Vehicle’. *2nd International Workshop on Intelligent Systems and Applications (ISA)*, pp 1-5
- Lovatt, H.C, Ramsden, V.S & Mecrow, B.C 1997, ‘Design of an in-wheel motor for a solar-powered electric vehicle’, *8th International Conference on Electrical Machines and Drives*. Cambridge, UK, pp 234-238
- Lyra, R.O.C & Lipo, T.A 2001, ‘Torque density improvement in a six-phase induction motor with third harmonic current injection’, *36th Industry Applications Conference*, Vol 3, pp. 1779-1786
- Meier, F 2008, ‘Design of a 10-pole 12-slot Permanent Magnet Synchronous Motor for Traction Applications’, *KTH Royal Institute of Technology, Sweden*
- Melfi, M, Evon, S & McElveen, R 2008, ‘Permanent Magnet Motors for Power Density and Energy Savings in Industrial Applications’, *54th Annual Pulp and Paper Industry Technical Conference PPIC2008*, pp. 218-225
- Merritt, B, Post, R, Dreufuerst, G & Bender, D 1994, *Halbach Array Motor/Generators - A Novel Generalized Electric Machine*. Halbach Festschrift Symposium, Berkeley CA
- Mevey, J 2006, *Sensorless Field Oriented Control of Brushless Permanent Magnet Synchronous*

Motors. Masters thesis, Kansas State University.

- *Michelin Active Wheel Press Kit*, 2008 Paris Motor Show
- Murray, A, Kettle, P & Moynihan, F 1997, 'Advances in Brushless Motor Control', *American Control Conference '97*, vol. 6, pp 3985-3989
- Nanda, G & Kar, N 2006, 'A Survey and Comparison of Characteristics of Motor Drives Used in Electric Vehicles', *Canadian Conference on Electrical and Computer Engineering CCECE'06*, pp. 811-814
- Oh, S & Emadi, A 2004, 'Test and Simulation of Axial Flux Motor Characteristics for Hybrid Electric Vehicles', *IEEE Transactions on Vehicular Technology*, vol. 53, no. 3, pp. 912-919
- Parcelle, A 1890, *Electromotor Traction Wheel*. US Patent 433180
- Patterson, D & Spée, R 1995, 'The Design and Development of an Axial Flux Permanent Magnet Brushless DC Motor for Wheel Drive in a Solar Powered Vehicle', *IEEE Transactions on Industry Applications*, Vol. 31, No. 5, pp. 1054-1061
- PML Flightlink, *Protean Electric In-Wheel Motors*. Available from <<http://www.pmlflightlink.com>>
- Rahman, K, Patel, N, Ward, T, Nagashima, J, Caricchi, F & Crescimbin, F 2006, 'Application of Direct-Drive Wheel Motor for Fuel Cell Electric and Hybrid Electric Vehicle Propulsion System', *IEEE Transactions on Industry Applications*, Vol. 42, No. 5, pp. 1185-1192
- Rajagopal, K & Sathaiah, C 2006, 'Computer Aided Design and FE Analysis of a PM BLDC Hub Motor', *International Conference on Power Electronics, Drives and Energy Systems, PEDES'06*, pp. 1-6
- Ravaud, R, Lemarquand, G & Lemarquand, V 2009, 'Ironless Permanent Magnet Motors: Three-Dimensional Analytical Calculation', *IEEE International Electric Machines and Drives Conference IEMDC'09*, pp. 947-952
- Rhodes, DJ 1977, 'Assessment of vernier motor design using generalised machine concepts', *IEEE Transactions on Power Apparatus and Systems*, vol. PAS-96, no. 4, pp. 1346-1352
- Roos, F & Spiegelberg, C 2004, 'Relations between size and gear ratio in spur and planetary gear trains', *Department of Machine Design, Royal Institute of Technology, Stockholm*
- Sawyer, C 2006, 'Around the eCORNER', *Automotive Design and production*, 10 March
- Schalkwyk, D & Kamper, M 2006, 'Effect of Hub Motor Mass on Stability and Comfort of Electric Vehicles', *IEEE Vehicle Power and Propulsion Conference, VPPC '06*

- Stachowiak, G & Batchelor, A 1993, *Engineering Tribology*, Elsevier Science Publishers, Amsterdam
- Sullivan, C 2001, 'Cost-Constrained Selection of Strand Diameter and Number in a Litz-Wire Transformer Winding', *IEEE Transactions on Power Electronics*, vol.16, No.2, pp. 281-288
- Svechkarenko, D, Soulard, J & Sadarangani, C 2008, *A Novel Transverse Flux Generator in Direct-Driven Wind Turbines*. Royal Institute of Technology, Stockholm, Sweden.
- Terashima, M, Ashikagi, T, Mizuno, T, Natori, K, Fujiwara, N & Yada, M 1997, 'Novel motors and controllers for high-performance electric vehicle with four in-wheel motors', *IEEE Transactions on Industrial Electronics*, Vol. 44, pp. 28-38
- Theryc, C 1896, *Wheel with Electrical Motor Hub for Vehicles*. US Patent 572036
- Toba, A & Lipo, T 1999, 'Novel dual-excitation permanent magnet Vernier machine', *International Conference for Electric Machines and Drives 1999*, pp.522-524
- Tseng, K & Chen, G 1997, 'Computer-Aided Design and Analysis of Direct-Driven Wheel Motor Drive', *IEEE Transactions on Power Electronics*, Vol. 12, Issue 3, pp. 517-527
- Versèle, C, De Grève, Z, Vallée, F, Hanuise, R, Deblecker, O, Delhaye, M & Lobry, J 2009, 'Analytical Design of an Axial Flux Permanent Magnet In-Wheel Synchronous Motor for Electric Vehicle', *13th European Conference on Power Electronics and Applications*
- Volk, J 2008, *Permanent Magnet Work at Fermilab, 1995 to present*. Fermilab, United States.
- Wadnerkar, V, Das, G & Rajkumar, A 2005, 'Performance Analysis of Switched Reluctance Motor; Design, Modelling and Simulation of 8/6 Switched Reluctance Motor', *Journal of Theoretical and Applied Information Technology*, Vol. 4, No. 11, pp. 1118-1124
- Walker, J 2005, 'The Physics Of Braking Systems', StopTech LLC.
- Wang, S et al 2005, 'Implementation of a 50-kW Four-Phase Switched Reluctance Motor Drive System for Hybrid Electric Vehicle', *IEEE Transactions on Magnetics*, vol. 41, no. 1, pp. 501-504
- Wildi, T 2002, *Electrical Machines, Drives and Power Systems, 5th Edition*, Prentice Hall
- Woolmer, T & McCulloch, D 2007, 'Analysis of the Yokeless and Segmented Armature Machine', *Electric Machines and Drives Conference IEMDC'07*, vol 1, pp 704-708
- Wikipedia: *Brushless DC electric motor*. Available from: <http://en.wikipedia.org/wiki/Brushless_DC_electric_motor>.

- Wikipedia: *Halbach array*. Available from <http://en.wikipedia.org/wiki/Halbach_array>
- Wikipedia: *Mitsubishi i-MiEV*. Available from <http://en.wikipedia.org/wiki/Mitsubishi_i-MiEV>
- Wikipedia: *Induction motor*. Available from <http://en.wikipedia.org/wiki/Induction_motor>
- Wikipedia: *Nissan Leaf*. Available from <http://en.wikipedia.org/wiki/Nissan_Leaf>
- Wikipedia: *Tesla Roadster*. Available from <http://en.wikipedia.org/wiki/Tesla_Roadster>
- Wikipedia: *Wheel Hub Motor*. Available from <http://en.wikipedia.org/wiki/Wheel_hub_motor>
- Wu, S, Song, L & Cui, S 2007, 'Study on Improving the Performance of Permanent Magnet Wheel Motor for the Electric Vehicle Application', *IEEE Transactions on Magnetics*, Vol. 43, No. 1, pp. 438-442
- Xiaoyuan, W, Fang, Z, Jingjuan, D & Renyuan, T 2005, 'The Magnetic Field Simulation of Multi-disc Coreless Permanent Magnet Synchronous Motor Based on Halbach Array', *Proceedings of the 8th International Conference on Electrical Machines and Systems, ICEMS2005*, Vol. 3, pp. 2083-2086
- Yang, Y & Chuang, D 2007, 'Optimal Design and Control of a Wheel Motor for Electric Passenger Cars', *IEEE Transactions on Magnetics*, Vol. 43, No. 1, pp. 51-61
- Yang, Y, Liang, J, Xing, X 2009, 'Design and Application of Axial-Flux Permanent Magnet Wheel Motors for an Electric Vehicle', *IEEE AFRICON '09*, 23-25 Sept 2009
- Yang, Y, Luh, Y & Cheung, C 2004, 'Design and Control of Axial-Flux Brushless DC Wheel Motors for Electric Vehicles', *IEEE Transactions on Magnetics*, Vol. 40, No. 4, Pp 1873 - 1891
- *YASA Motors: YASA-750*. Available from: <<http://www.yasamotors.com/technology/products/yasa-750>>. [25 May 2011]
- Zhang, L, Wen, X & Wang, Y 2010, 'Research of Permanent Magnets Failure for High Power-Density Interior PM Synchronous Motor Used in Electric Vehicles', *2010 International Conference on Electrical Machines and Systems*, pp. 1098-1102
- Zielinski, P & Schoepp, K 1991, *Three-Phase Low-Speed Permanent Magnet Synchronous Machines*. Technical University of Wroclaw, Poland

APPENDICES

APPENDIX I: VEHICLE DYNAMICS FORMULAE

I.A ENERGY AND POWER REQUIREMENTS

For a vehicle in motion, the power required to maintain a steady state velocity has two components, aerodynamic drag and rolling resistance, given by the following formulae:

$P_{\text{drag}} = 0.5 \rho C_d A V^3$	P_{drag}	Aerodynamic drag power, in watts
	ρ	Density of air, typ. 1.2kg/m ³
	C_d	Coefficient of drag (no units)
	A	Frontal area, in m ²
	V	Velocity, in m/s
$P_{\text{rr}} = V C_{\text{rr}} g m$	P_{rr}	Rolling resistance power, in watts
	V	Velocity, in m/s
	C_{rr}	Coefficient of rolling resistance
	g	Gravitational constant (9.81m/s ²)
	m	Mass, in kg

The energy and power involved with vehicle acceleration may be calculated using the following:

$E_k = \frac{1}{2} m V^2$	E_k	Kinetic Energy, in joules
	P	Power, in watts
	m	Mass, in kg
$P = \frac{m V^2}{2t}$	V	Velocity, in m/s
	t	Time (delta), in seconds

A third use of vehicle power is in hill climbing, the formulae for which are:

$E = m g h$	E	Potential Energy, in joules
	P	Power, in watts
$P = m g h / t$	m	Mass, in kg
	g	Gravitational constant (9.81m/s ²)
	h	Height (delta), in metres
	t	Time period, in seconds
	V	Velocity, in m/s
$P = m g V \sin\theta$	θ	Angle of inclination

Total power for any vehicle is simply the sum of these components:

$$P_{\text{total}} = P_{\text{drag}} + P_{\text{rr}} + P_{\text{accel}} + P_{\text{climb}}$$

I.B MAXIMUM LOAD TRANSFER

Load transfer (sometimes called weight transfer) is the change in load experienced by vehicle wheels due to lateral or transverse acceleration (including cornering and braking). The formula for weight transfer is given by:

$$\Delta F = \frac{m H a}{L}$$

ΔF	Change in load force	
m	Vehicle mass	
H	Height of centre of gravity	<i>(FItechnical.net: Suspension)</i>
L	Wheel base / track	

Relevant vehicle dimensions for the 2011 UWA Formula SAE Electric vehicle are shown in Figure 11.1 and 11.2:

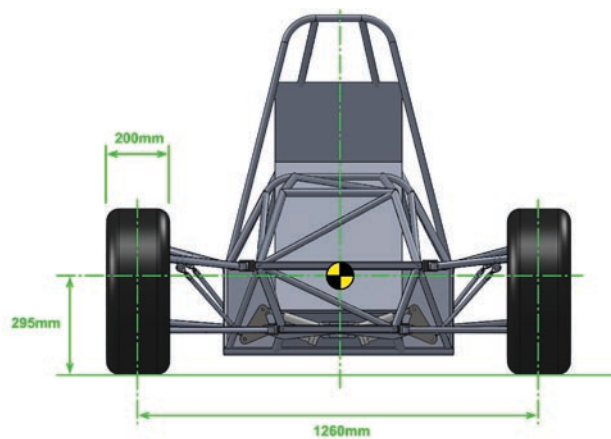


Figure 11.1: FSAE vehicle Centre of Gravity location (front view)

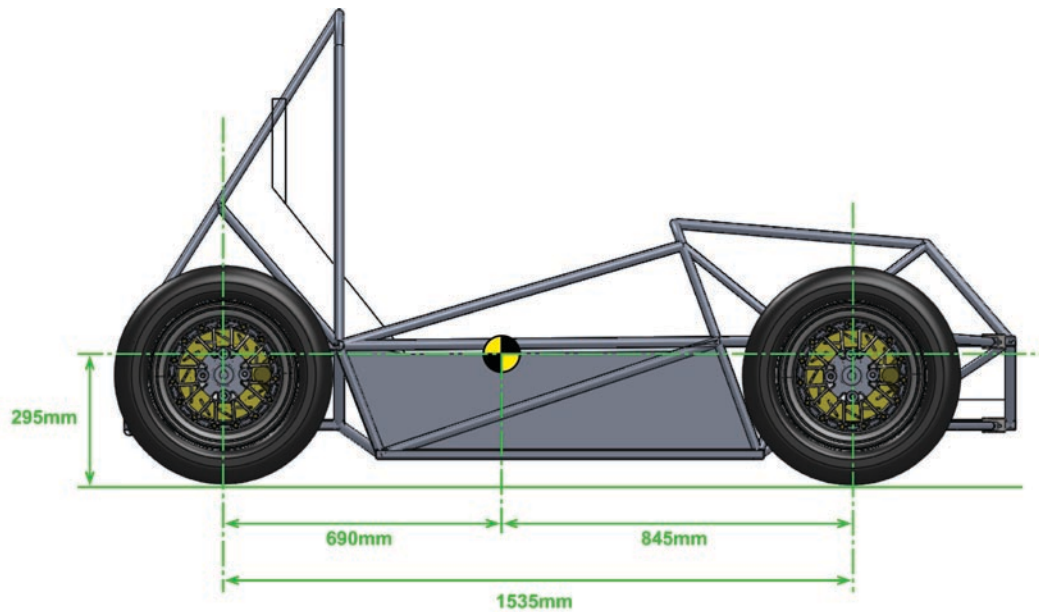


Figure 11.2: FSAE vehicle Centre of Gravity location (side view)

Assuming a vehicle weight including driver of 290kg and a maximum cornering or braking acceleration of 1.5G for high-performance tires, maximum load transfer for the vehicle is calculated as follows:

Cornering: $\Delta F = 300 \cdot 0.295 \cdot (9.81 \cdot 1.5) / 1.26 = 1033 \text{ N}$

$$\Delta \text{Load} = 1033 / 9.81 = 105 \text{ kg}$$

$$\therefore \text{Load on outside wheels} = 290 / 2 + 105 = 250 \text{ kg (2540N)}$$

$$\text{Load on inside wheels} = 290 / 2 - 105 = 40 \text{ kg (380N)}$$

Braking: $\Delta F = 300 \cdot 0.295 \cdot (9.81 \cdot 1.5) / 1.535 = 848 \text{ N}$

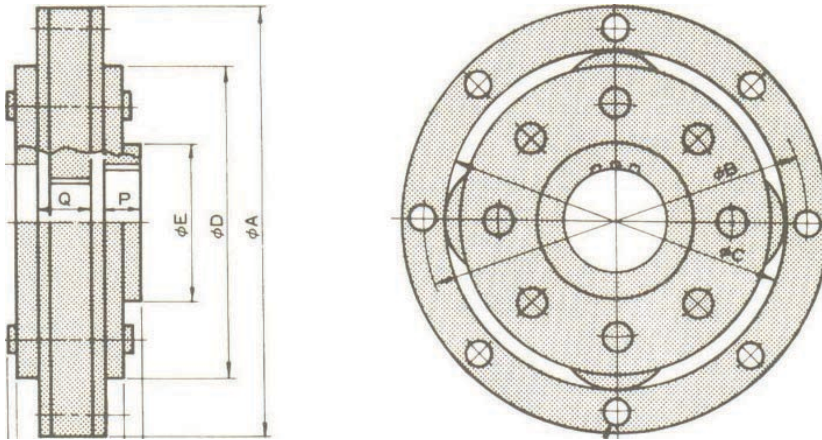
$$\Delta \text{Load} = 848 / 9.81 = 86 \text{ kg}$$

$$\therefore \text{Load on front wheels} = 290 / 2 + 86 = 231 \text{ kg (2260N)}$$

$$\text{Load on rear wheels} = 290 / 2 - 86 = 59 \text{ kg (580N)}$$

APPENDIX II: COMPONENT SPECIFICATIONS/DATASHEETS

II.A MATEX PLANETARY GEARBOX



Specifications	
Maximum Torque	2000 kg-cm
Maximum Torque	1739 lb-in.
Nominal Reduction Ratio	5:1
Actual Reduction Ratio	5:1
Dimension - A	120.00 mm
Dimension - B	109.00 mm
Dimension - C	99.00 mm
Dimension - D	94.00 mm
Dimension - E	40.00 mm
Dimension - F	32.00 mm
Dimension - J	8 x 6.5 mm
Dimension - L1	29.80 mm
Dimension - L2	16.00 mm
Dimension - L3	26.30 mm
Dimension - M	10.30 mm
Dimension - N	3.50 mm
Dimension - O	3.20 mm
Dimension - P	10.00 mm
Dimension - R	1.00 mm
Weight	1330 grams
Moment of Inertia	51.79 kg-cm ²
Female Spline - Size (Input)	17.00 mm
Female Spline - Teeth Number (Input)	15
Female Spline - Module (Input)	1.00 mm
Female Spline - Size (Output)	30.00 mm
Female Spline - Teeth Number (Output)	16
Female Spline - Module (Output)	1.67 mm
Dimension - Q	13.00 mm

II.B BELT DRIVE DATA (GATES TRANSMISSIONS 2011)



Industrial Belt Design - Drive Detail Report Design Flex® Pro by the Gates Corporation

Designed For:		Provided By: Phillip Aitken Gates Corporation 1-15 Hydrive Close Dandenong South, Victoria 3175 Australia paitken@gates.com +61 3 9797 9643 Phone +61 3 9797 9600 Fax	
Application: Design #1			
INPUT			
Drive Information		DriveR	DriveN
Known Belt: PowerGrip GT3 - 490-5MGT3 - 25.00 mm		Known Size: 18 Grooves	90 Grooves
Speed Ratio: 5.00 Down		RPM: 6000.0	1200.0
Input Load: 20 N-m		Maximum Rim Speed: 33 m/s	33 m/s
Service Factor: 1.6		Bushings Checked: TL	
Design Power: 32 N-m		Belts Checked: PowerGrip GT3	
Center Distance: 91.36 mm		Electric Motor	
SELECTED DRIVE			
Belt Type: PowerGrip GT3 - 5M		Belt	DriveR
		Part No: 490-5MGT3-25	18-5MR-25
		Product No: 9400-45253	90 Grooves
Speed Ratio: 5.00 Down		Top Width: --	Non-Stock Item
dN RPM: 1200.0		Weight: 50 g	--
Rated Load: 4.74 N-m		Rim/Belt Speed: 9.0 m/s	8.6 m/s
Belt Pull: 1650 N		RPM: 1102.0	8.9 m/s
Center Distance: 91.36 mm		Bushing Part No: --	1200.0
Install/Take-Up Range: 76.88 mm to 92.12 mm		Bore: --	--
		Pitch Diameter: --	28.65 mm
			143.2 mm
TENSION			
	New Belt	Used Belt	
Rib/Strand Deflection Distance:	1.42 mm	1.42 mm	When planning to re-install used belts, measure and record the tension before removing and re-install at the recorded tension.
Rib/Strand Deflection Force:	7.3 to 8.0 kg	5.2 to 5.9 kg	
Sonic Tension Meter			
Belt Frequency: 642 to 674 Hz		537 to 575 Hz	
505C/507C Model STM Settings: Weight: 4.1 g/m, Width: 25 mm/#R, Span: 71 mm			
NOTES			
<ul style="list-style-type: none"> - Centre Distance is Close. Pulleys may interfere during installation. - The input load exceeds the rated drive load capacity and may result in poor performance. - The belt length was user specified. - The belt width was user specified. - The installation allowance falls out of the specified centre distance range. - The DriveR pulley must be bored to the required size. Allow proper lead times. - The DriveR bore & shaft should meet a H8 clearance fit. The shaft must penetrate 100%. - The DriveN pulley is a special order item. Bore and bush are not known. 			
<ul style="list-style-type: none"> - Design Flex Drive Solutions assume Gates products and are not applicable to non-Gates products. - products are not intended for use in any application where the failure of the product to perform could cause injury or death. This includes use on aircraft propeller or rotor drive systems or other in-flight systems necessary for safe flight. 			

